

**Best
Available
Copy**

AD-A286 158



SOC-R875-003-1094

**NON-DESTRUCTIVE INSPECTION
BY INFRARED
IMAGING SPECTROSCOPY**

PHASE I FINAL REPORT

Prepared for:
**DEPARTMENT OF THE ARMY
U.S. ARMY ARDEC**
Picatinny Arsenal, New Jersey 07806-5000

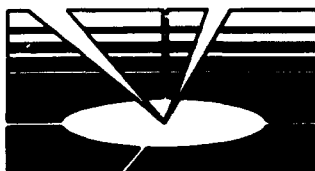
Prepared under:
CONTRACT NUMBER DAAA21-94-C-0013

Reporting period:
14 FEBRUARY 1994 THROUGH 14 OCTOBER 1994

This document has been approved
for public release and sale; its
distribution is unlimited.

Point of contact:
MARK S. DOMBROWSKI

**SURFACE OPTICS
CORPORATION**



**P.O. Box 261602
San Diego, CA 92196
TEL: (619) 578-8910
FAX: (619) 578-0484**

94-34781



1409

14 OCTOBER 1994

94

7

REPORT DOCUMENTATION PAGE

Form Approved
OMB No. 0704-0188

Public reporting burden for this collection of information is estimated to average 1 hour per response, including the time for reviewing instructions, searching existing data sources, gathering and maintaining the data needed, and completing and reviewing the collection of information. Send comments regarding this burden estimate or any other aspect of this collection of information, including suggestions for reducing this burden, to Washington Headquarters Services, Directorate for Information Operations and Reports, 1215 Jefferson Davis Highway, Suite 1204, Arlington, VA 22202-4302, and to the Office of Management and Budget, Paperwork Reduction Project (0704-0188), Washington, DC 20503.

1. AGENCY USE ONLY (Leave blank)	2. REPORT DATE 14 OCT 94	3. REPORT TYPE AND DATES COVERED Final Report, 14 FEB 94 - 14 OCT 94	
4. TITLE AND SUBTITLE Non Destructive Inspection by Infrared Imaging Spectroscopy - Phase I Final Report		5. FUNDING NUMBERS C	
6. AUTHOR(S) Mark Dombrowski Virgil Moore (Editor, Compiler)			
7. PERFORMING ORGANIZATION NAME(S) AND ADDRESS(ES) Surface Optics Corporation 9929 Hibert Street, Suite C San Diego, CA 92131		8. PERFORMING ORGANIZATION REPORT NUMBER SOC-R875-003-1094	
9. SPONSORING/MONITORING AGENCY NAME(S) AND ADDRESS(ES) Department of the Army U.S. Army ARDEC Picatinny Arsenal, NJ 07806-5000		10 SPONSORING/MONITORING AGENCY REPORT NUMBER	
11. SUPPLEMENTARY NOTES			
12a. DISTRIBUTION/AVAILABILITY STATEMENT Public availability		12b. DISTRIBUTION CODE	
13. ABSTRACT Maximum: 150 words The objective of the Phase I effort was to investigate the applicability of infrared imaging spectroscopy to multiple Non-Destructive Inspection (NDI) applications. The program demonstrated object discrimination using an algorithm which post-processes an infrared spectral image of two apparently identical objects by filtering across the spectral radiance distribution of the scene. The project also addressed three major design issues concerning the transition of Surface Optics's existing visible spectral radiometer to an infrared version.			
14. SUBJECT TERMS Non-destructive, Spectral, Imaging, Radiometer, Discrimination, Identification, Test, Infrared		15. NUMBER OF PAGES	
		16. PRICE CODE	
17. SECURITY CLASSIFICATION OF REPORT UNCLASSIFIED	18. SECURITY CLASSIFICATION OF THIS PAGE UNCLASSIFIED	19. SECURITY CLASSIFICATION OF ABSTRACT UNCLASSIFIED	20. LIMITATION OF ABSTRACT UL

SOC-R875-003-1094

**NON-DESTRUCTIVE INSPECTION
BY INFRARED
IMAGING SPECTROSCOPY**

PHASE I FINAL REPORT

Prepared for:

**DEPARTMENT OF THE ARMY
U.S. ARMY ARDEC
Picatinny Arsenal, New Jersey 07806-5000**

Reporting period:

14 FEBRUARY 1994 THROUGH 14 OCTOBER 1994

Prepared under:
CONTRACT NUMBER DAAA21-94-C-0013

14 OCTOBER 1994

Action For	
NTIS	CRA&I
DTIC	TAB
Unannounced	
Justification	
By	
Distribution /	
Availability Codes	
Dist	Avail and/or Special
A-1	

UNCLASSIFIED

TABLE OF CONTENTS

SECTION		PAGE
1.0	RESULTS OF PHASE I WORK	1
1.1	Summary	1
1.2	Research on NDI Applications of Infrared Imaging Spectroscopy	2
1.3	Radiometer Design Study Summary	8
1.4	Imaging Spectrometer Detailed Description	10
1.4.1	Objective Lens	12
1.4.2	Circular Variable Filter	12
1.4.3	Imaging Array	13
1.4.4	Internal Calibration Sources	14
1.4.5	Spectral Operating Modes	15
1.4.5.1	Integration Time Limits For Spectral Scanning	15
1.4.5.2	Number of Spectral Exposures per Frame ..	17
1.4.6	Spectrometer Energy Throughput	19
1.4.7	Spectral Imager Noise Levels	21
1.5	Processing Electronics	26
1.5.1	Data Collection and Storage	30
1.5.2	Calibration	31
1.5.3	Processing	32
1.5.4	Control and Data Interfaces	33
2.0	POTENTIAL FOLLOW-ON APPLICATIONS	34
2.1	Introduction	34
2.2	Potential Commercial or Private Sector Applications	35
2.2.1	The Optical Sensor Consortium	37
2.2.2	Example Application #1: Ranging and Detection	38
2.2.3	Example #2: Automobile Exhaust Testing	40
2.3	Potential Uses by the Federal Government	42

UNCLASSIFIED

TABLE OF APPENDICES

<u>APPENDIX</u>		<u>PAGE</u>
A	Non-Destructive Inspection by Infrared Imaging Spectroscopy - Progress Report #1	A-1
B	Non-Destructive Inspection by Infrared Imaging Spectroscopy - Progress Report #2	B-1

LIST OF FIGURES

<u>FIGURE</u>		<u>PAGE</u>
1-1	Comparison of a Clean (FS6855) and a Silica Contaminated Graphite Composite Sample (FS6854)	3
1-2	8 μ m to 12.0 μ m Broad-Band Image of COI Samples	3
1-3	Filtered Image using FS6854 as Filter Spectral Radiance	4
1-4	Filtered Image using FS6855 as Filter Spectral Radiance	4
1-5	Fit to Spectral Emissivity Data for Graphite Composite at Recovered Temperature 293.1°K	5
1-6	Comparison of the Simulated Spectral Radiance Data for Graphite Composite at 295°K, and the Radiance using the Emissivity Fit and Recovered Temperature	5

UNCLASSIFIED

LIST OF FIGURES (Continued)

<u>FIGURE</u>		<u>PAGE</u>
1-7	Spectral Directional Reflectance of Rusted Iron (FS6829), Red Painted Iron (FS6830), and Red Painted Iron Contaminated with a Thin Film of Machine Oil (FS6831)	6
1-8	8.0 μm to 12.0 μm Broad Band Image of Rust (Left), Red Paint (Center), and Oil-Coated Red Paint (Right)	7
1-9	Filtered Image using Oil-Coated Paint as Filter Spectral Radiance	7
1-10	Filtered Image using Paint as Filter Spectral Radiance	8
1-11	Multi-Band VIS-LWIR Imaging Spectroradiometer	9
1-12	Schematic Overview of Imaging MWIR Spectroradiometer	9
1-13	CVF-Based High Speed Spectral Imager, Refractive Version	11
1-14	CVF-Based High Speed Spectral Imager, All Waveband Version	11
1-15	Filter Bandwidth vs. Cone Angle of Illumination	12
1-16	Effect of Integration Time on Filter Bandwidth	16
1-17	Number of Spectral Images vs. Frame Rate	18
1-18	Total Spectral Dispersion Across Array vs. Frame Rate	19
1-19	Definition of Terms for Energy Collection Analysis	20
1-20	NESR and Target Radiance for Spectral Imager	24
1-21	NESR and Target Radiance for Reduced Readout Noise Imager	24
1-22	SNR vs. Target Temperature for 250 μs Integration Time	25
1-23	Frame-to-Frame SNR vs. Frame Rate, 1.5-5.5 Sensor Emulation	25
1-24	MIDIS Processing Electronics Block Diagram	30
1-25	Detail of Matched Filtering Channel	32

UNCLASSIFIED

LIST OF FIGURES
(Continued)

<u>FIGURE</u>		<u>PAGE</u>
2-1	Methodology for Application Survey	34
2-2	Spectral Imager Applications	36
2-3	Intensity Ratio Versus Distance	39
2-4	Spectral Plot of Nitric Oxide	40
2-5	Application of Outrigger Bands	41

LIST OF TABLES

<u>TABLE</u>		<u>PAGE</u>
2-1	Potential Commercial Applications	37
2-2	List of Government Organizations Briefed on the Proposed Technology	42
2-3	List of Government Agencies Briefed at Symposiums on the Proposed Technology	43
2-4	Application Areas Identified by Government Personnel	43

UNCLASSIFIED

1.0 RESULTS OF PHASE I WORK

1.1 Summary

The primary objective of the Phase I SBIR effort was to demonstrate the feasibility of Non-Destructive Inspection (NDI) using imaging spectroscopy. Using Surface Optics Corporation's (SOC) existing visible band Real Time Imaging Radiometer (RTISR) as a baseline, the program focused on tailoring this instrument to the requirements of NDI. Surface Optics Corporation and NASA's Jet Propulsion Laboratory (JPL) were teamed to define the design and operating characteristics of this instrument during Phase I. Upon successful completion of Phase I, the team would then develop and demonstrate a prototype during Phase II, and bring the instrument to commercial viability during Phase III. Specifically, the objectives for Phase I were as follows:

- 1) to demonstrate the applicability of spectral matched filtering techniques to nondestructive monitoring.
- 2) to study the various methods of extending the wavelength coverage of the existing spectral imaging radiometer from 400nm-900nm to 400nm-12 μ m, as well as downselect to the best technical approach.
- 3) to study any changes, if necessary, to the powerful processing electronics within the radiometer to accommodate spectral matched filtering techniques, as well as to evaluate emerging electronic packaging technology which would allow for further miniaturizing of them below their already compact 240 in³. The goal is to better facilitate man portability.

To satisfy the objectives as stated above, SOC, in conjunction with JPL, conducted four distinct research activities. First, to satisfy the broad objective of defining NDI applications of imaging spectroscopy, specific areas in surface characterization of materials, circuit board inspection and composite materials inspection were investigated. To satisfy the first specific objective, SOC used a spectral resolution system to better identify and classify materials. Various spectral matching algorithms were applied to the data to demonstrate the ability to identify materials throughout an image based on their spectral radiances. To satisfy the second objective, SOC and JPL analytically investigated the specific components within the radiometer to evaluate alternate technologies such as acousto-optic tunable filters, liquid crystal filters and fourier transform interferometers. Finally, to satisfy the third objective SOC conducted a design trade study to evaluate the data collection and storage, calibration and processing modules of the electronics. The following sections describe this research in more detail.

UNCLASSIFIED

1.2

Research on NDI Applications of Infrared Imaging Spectroscopy

The first Phase I progress report documented the results of a literature review of the use of broad band thermal imagery to NDI applications and where addition of real-time, calibrated spectral image data would significantly enhance the diagnostic capabilities of the system. Our goal was to investigate real applications and demonstrate the capabilities of using spectral versus broad band imagery. We initially identified three NDI application areas for exploiting infrared imaging spectroscopy: material characterization, electronic circuit board inspection, and identification and mapping of contamination on graphite composite materials.

Our approach was to produce or procure material samples and perform laboratory reflectance measurements to identify spectral features that could be exploited using the spectral imaging camera. Computer simulations were performed to predict the performance of the imaging system and to develop and evaluate spectral processing algorithms. Two types of algorithms were evaluated: spectral matched filtering for spatially enhancing pixels with a desired reflectance spectrum in the image, and temperature and spectral emissivity determination from the pixel spectral radiance data in the image. Finally, a laboratory demonstration of infrared imaging spectroscopy was performed using a broad band, 3-12 micron, thermal imager and a series of discrete filters. Because of time and funding limitations, only the material characterization and the graphite composite contamination application were pursued. A complete description of the computer simulations, laboratory experiments, and results are provided in the second Phase I progress report, and a summary of these results are provided below.

The graphite composite contamination application was identified through discussions with a local firm, Composite Optics, Inc. (COI), that produces light weight, parabolic reflectors for space applications. The manufacture of these reflectors requires surface preparation with chemical etching treatments. The residue left from the chemical etching process affects the adhesion and quality of the subsequent metal deposition on the reflector surface. An imaging spectroradiometer that could identify regions on the reflector surface that are contaminated with the chemical etch residue would be very valuable to their quality control.

COI provided a number of samples of their graphite composite materials, some of which were known to be clean, and others known to be contaminated with a silica residue. Figure 1-1 shows a comparison of the 1.5 to 26 micron reflectance measurements of contaminated (FS6854) and clean (FS6855) samples of the graphite composite material, which shows significant variations in the 8 to 12 micron region. A broad band, 8 to 12 micron, image of these samples is shown in Figure 1-2, and shows very little discernable contrast difference between the samples. Using a spectral matched filtering algorithm, based on five experimental spectral points (4.4, 8, 9, 10.5, and 11.7 microns), demonstrated the capability for spatially enhancing features in the image with specific spectral properties. Figure 1-3 shows the filtered image using the five point filter derived from pixels on the contaminated sample (FS6854), which dramatically highlights the contaminated sample in the image. Similarly, Figure 1-4 shows an image of the clean sample (FS6855) highlighted after spectral matched filtering using a five point filter derived from pixels on the clean sample.

Theoretical analysis of algorithms for simultaneous determination of the sample temperature and spectral emissivity also show promise. Figure 1-5 shows the recovered temperature of 293°K and spectral emissivity using a simulated 19 point radiance spectrum in the 7 to 14 micron band, based on the laboratory measurement of the sample hemispherical emissivity. The resulting comparison with the simulated radiance for a surface at 295°K is shown in Figure 1-6. While more work remains to be done on the temperature and emissivity recovery algorithms, the Phase I results are encouraging.

UNCLASSIFIED

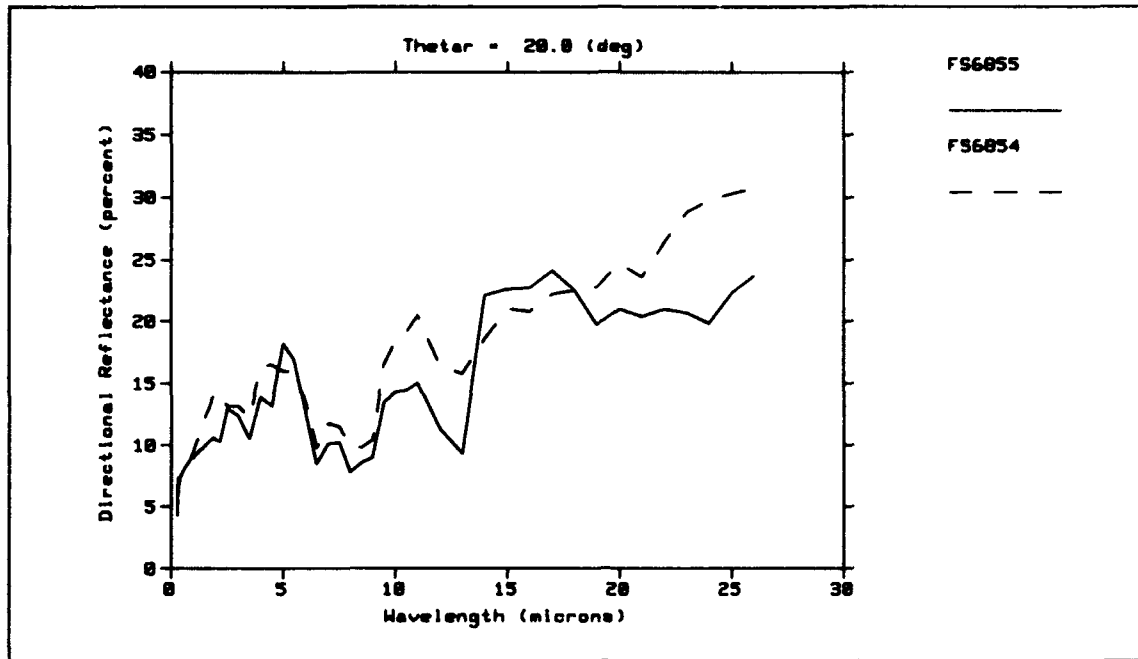


Figure 1-1. Comparison of a Clean (FS6855) and a Silica Contaminated Graphite Composite Sample (FS6854).

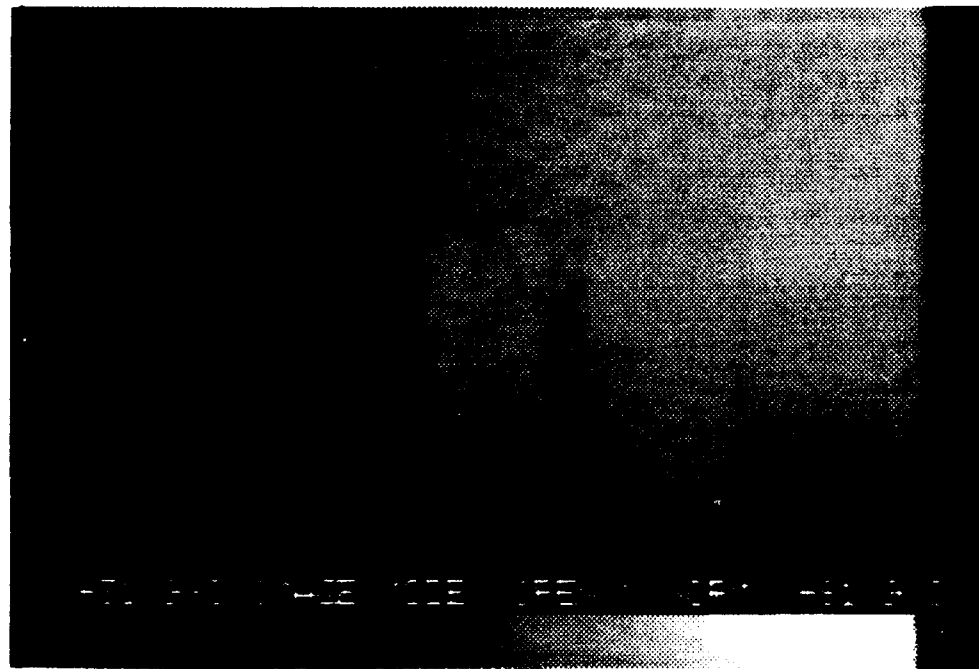


Figure 1-2. 8 μ m to 12.0 μ m Broad-Band Image of COI Samples.

UNCLASSIFIED

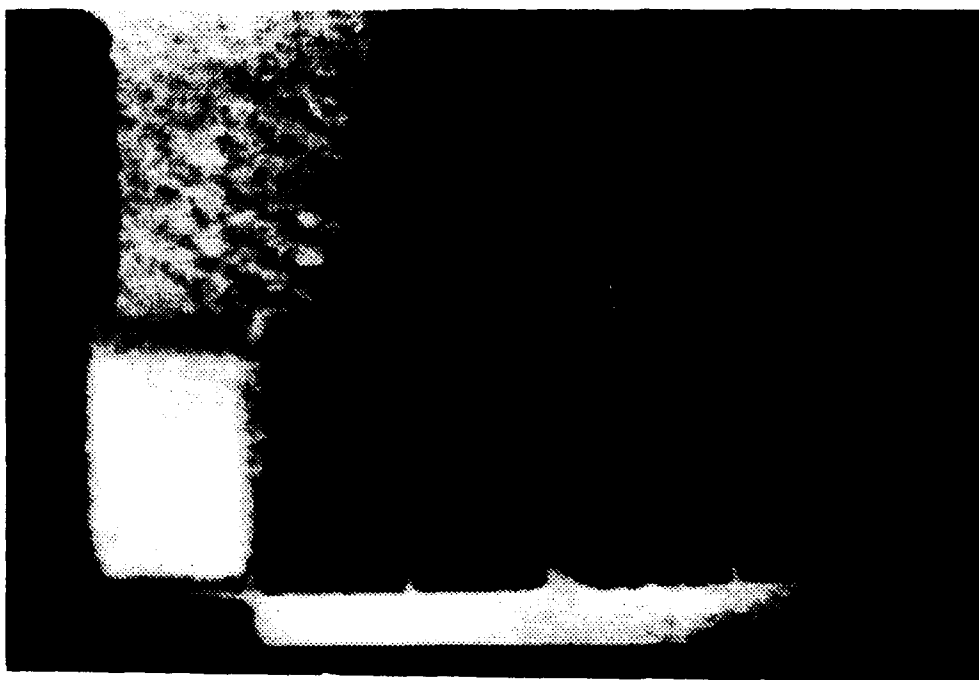


Figure 1-3. Filtered Image using FS6854 as Filter Spectral Radiance.

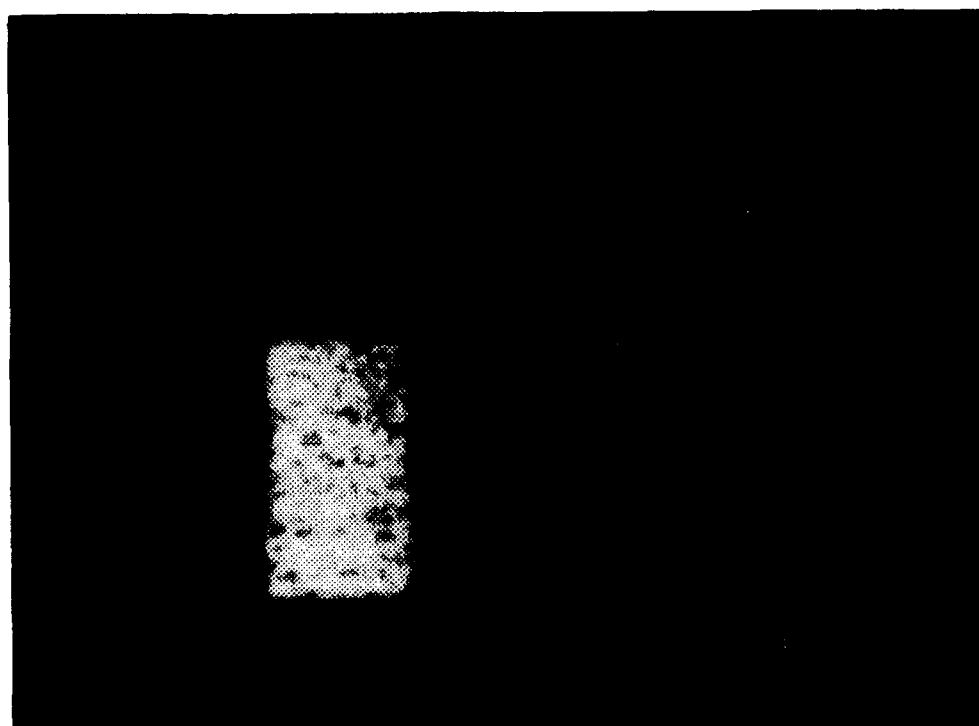


Figure 1-4. Filtered Image using FS6855 as Filter Spectral Radiance.

UNCLASSIFIED

UNCLASSIFIED

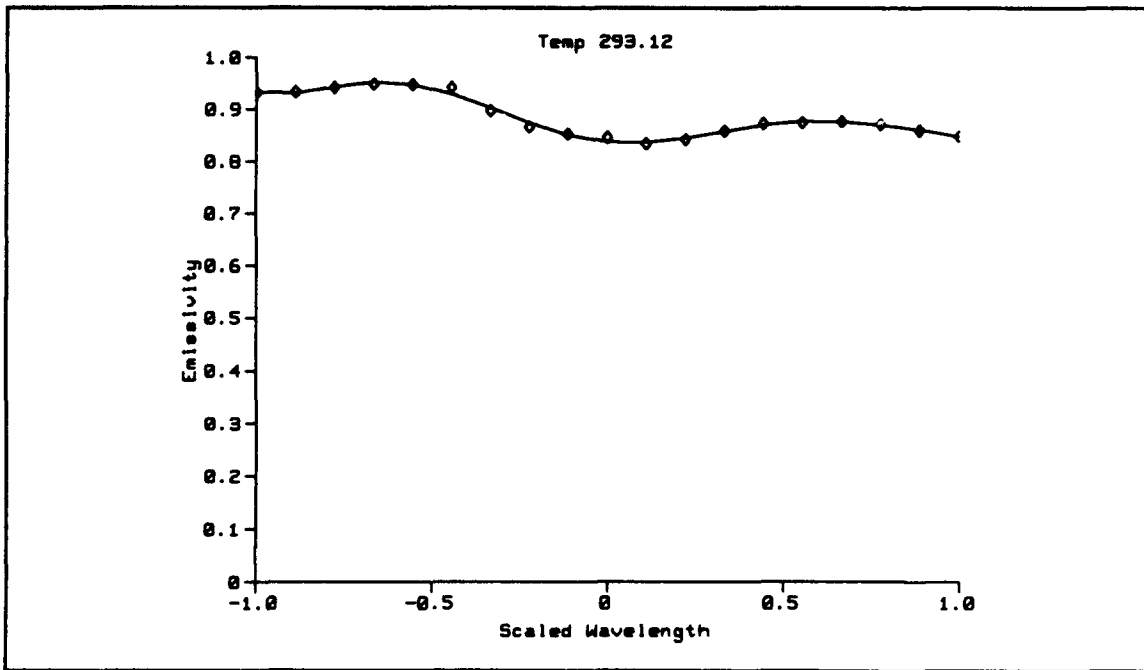


Figure 1-5. Fit to Spectral Emissivity Data for Graphite Composite at Recovered Temperature 293.1°K.

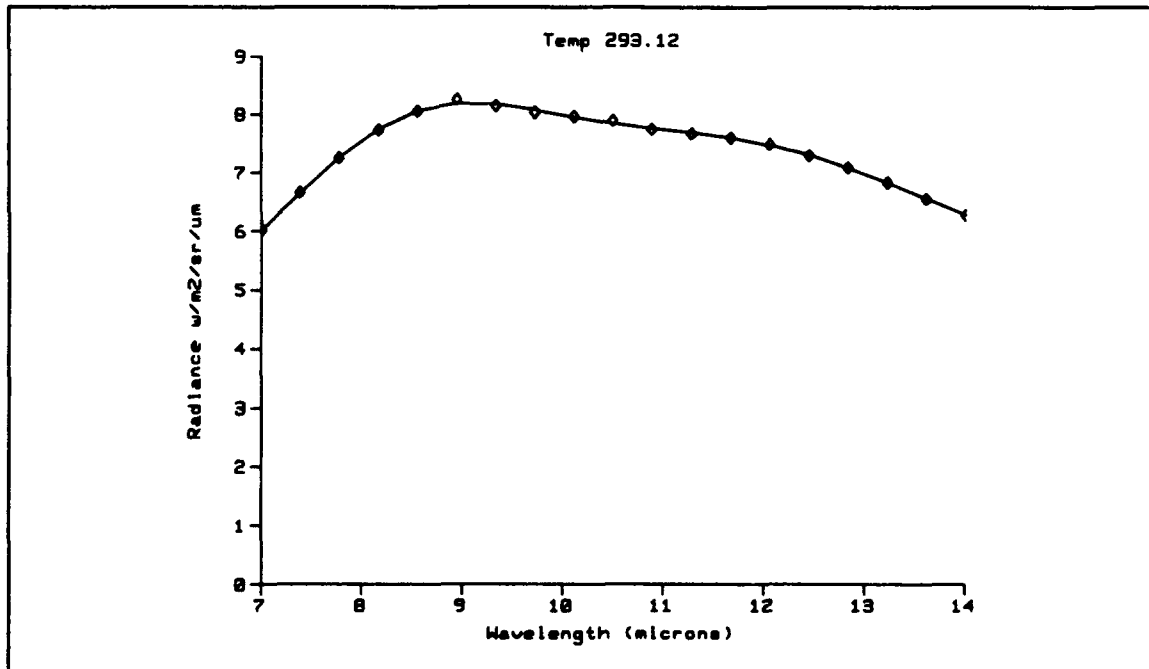


Figure 1-6. Comparison of the Simulated Spectral Radiance Data for Graphite Composite at 295°K, and the Radiance using the Emissivity Fit and Recovered Temperature.

UNCLASSIFIED

The second NDI application studied was developed based on discussions with ARDEC personnel. Experience with visual inspection of shell casings shows that it is sometimes difficult to differentiate between rusted and painted casings. Infrared spectral data can be used to characterize material surface treatments. We investigated this application by cutting a sample of rusted iron into three pieces. The rust was removed from two of the pieces, which were coated with a rust colored red paint. One of the samples was then coated with a thin film of machine oil. These three samples represent three types of surface conditions which are visually similar, but have distinctly different mid-infrared reflectances as shown in Figure 1-7.

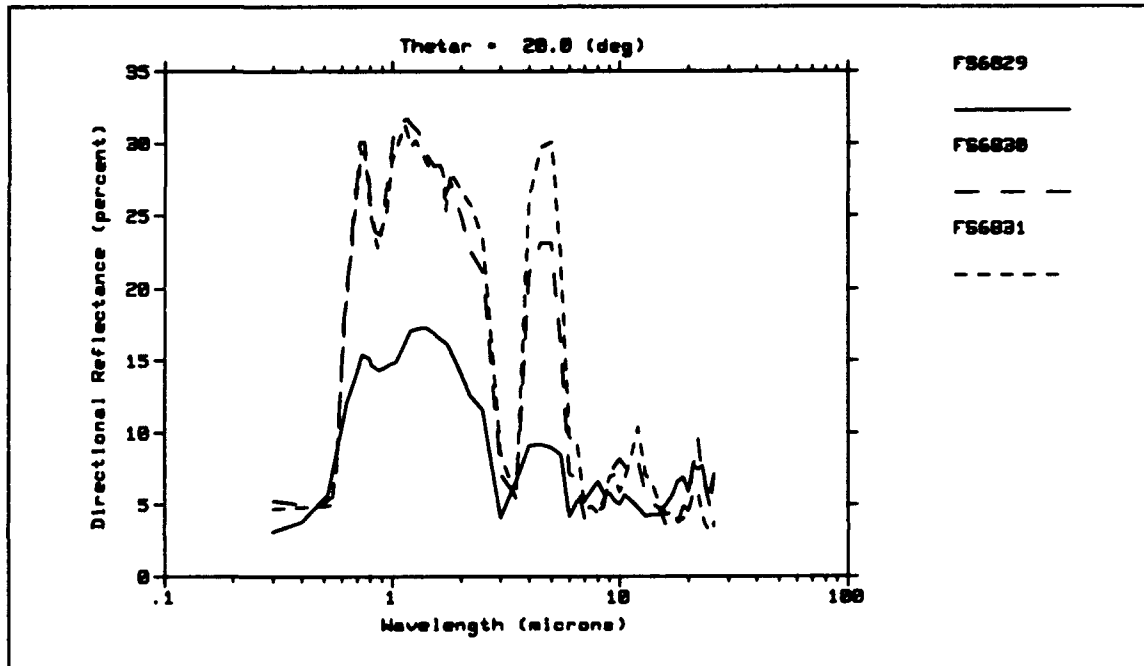


Figure 1-7. Spectral Directional Reflectance of Rusted Iron (FS6829), Red Painted Iron (FS6830), and Red Painted Iron Contaminated with a Thin Film of Machine Oil (FS6831).

As before, the laboratory measurement of infrared spectral imagery was limited to five points between 4.4 and 11.7 microns, which would not necessarily optimally exploit the spectral features of the different surface treatments. The broad band, 8 to 12 micron, image of the three samples is shown in Figure 1-8, which again shows little contrast variation. Figure 1-9 shows the result of spectral matched filtering the image using the spectral radiance from pixels on the oil coated sample as the filter. This clearly highlights the oil coated sample in the image, all other areas appearing dark. Similarly, Figure 1-10 shows the result of using the pixel spectral radiances of the painted sample as the filter. The painted sample and, to a lesser extent, the oil coated painted sample are bright, while the rusted sample is dark.

UNCLASSIFIED

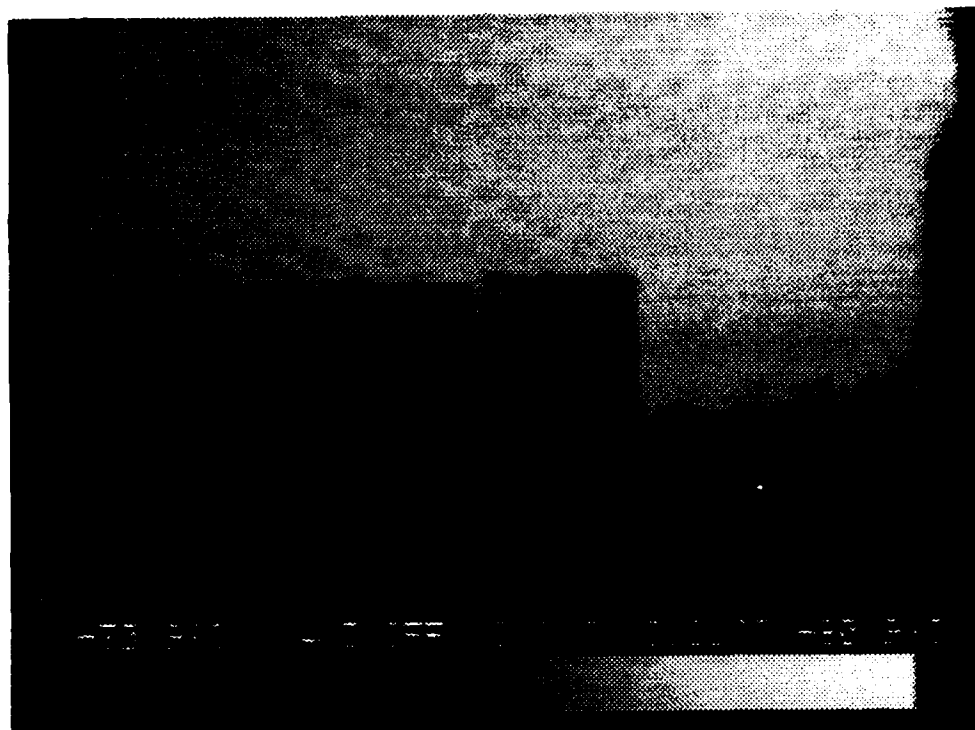


Figure 1-8. 8 μm to 12 μm Broad Band Image of Rust (Left), Red Paint (Center), and Oil-Coated Red Paint (Right).

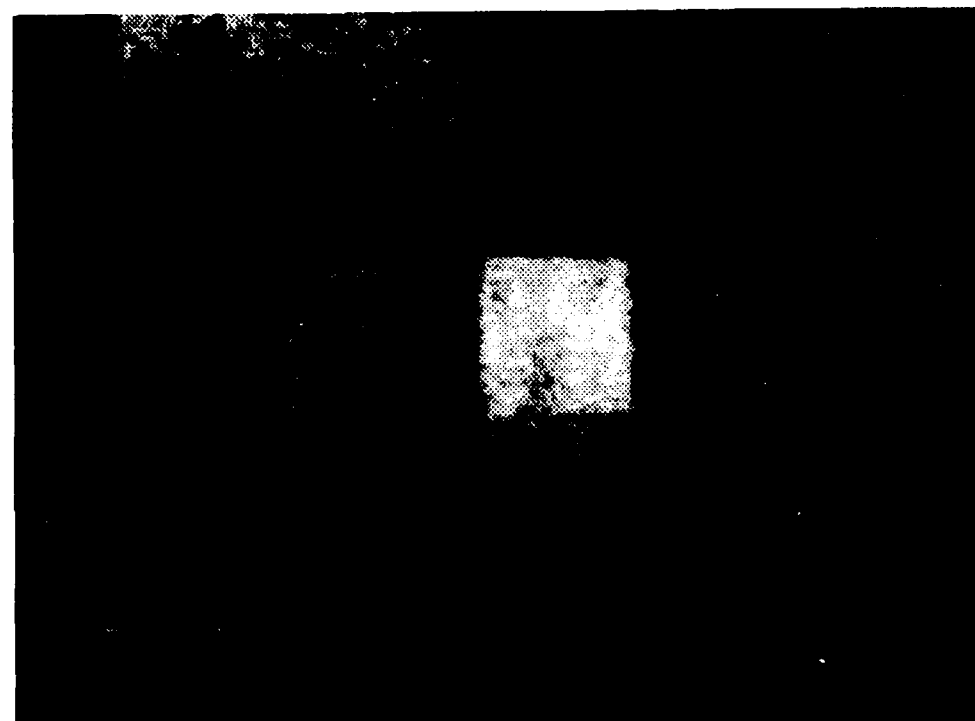


Figure 1-9. Filtered Image using Oil-Coated Paint as Filter Spectral Radiance.

UNCLASSIFIED

UNCLASSIFIED



Figure 1-10. Filtered Image using Paint as Filter Spectral Radiance.

The laboratory demonstration of the use of infrared imaging spectroscopy for NDI applications that was performed during this Phase I program shows promising results. The spectrally filtered images, using one detector, five spectral points, and taking many hours to acquire and post process, clearly identified the regions in the image which matched the spectral filter. These results demonstrated only a small fraction of the capability of the proposed instrument with 256x256 detectors, 30 to 60 spectral points, and real time processing and display.

1.3 Radiometer Design Study Summary

To satisfy the second and third objectives of the Phase I effort, a preliminary design of an infrared radiometer was conducted. A detailed technical description of the instrument is presented below. Figure 1-11 presents a conceptual drawing of the ultimate 400 nm - 30 μ m instrument, with three heads attached to a single processor. As illustrated schematically in Figure 1-12, basic design of a Multiband Identification and Discrimination Imaging Spectroradiometer (MIDIS) is straight forward, allowing construction of a compact, rugged, easily producible instrument. The instrument comprises four main sections. First, raw spectral images are gleaned by a continuously variable narrowband IR filter-based imaging

UNCLASSIFIED

UNCLASSIFIED

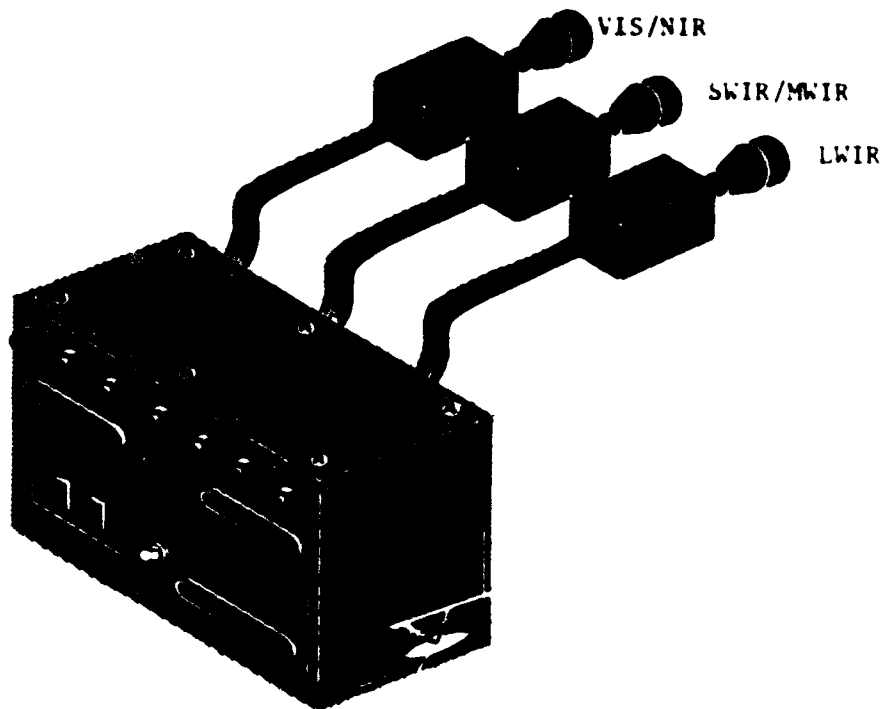


Figure 1-11. Multi-Band VIS-LWIR Imaging Spectroradiometer.

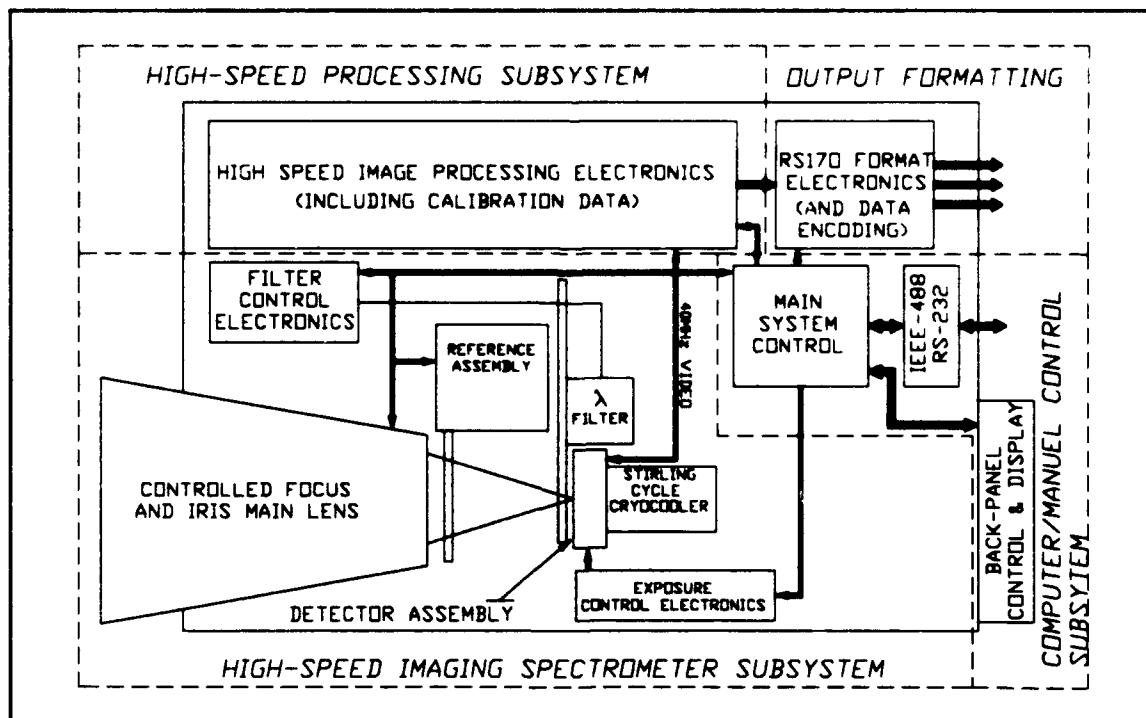


Figure 1-12. Schematic Overview of Imaging MWIR Spectroradiometer.

UNCLASSIFIED

spectrometer at up to a 600Hz rate. Second, raw image data is collected, spectro-radiometrically calibrated, and processed by a high-speed processing section. Third, data is formatted as standard RS-170 analog video data or as high speed 12-bit digital data by an output processing section. Fourth, overall system operation is monitored and controlled by a system controller which also communicates to an external computer over standard serial or parallel busses.

All functions of the instrument, e.g. CVF speed, integration time, iris, will have both an automatic and manual mode. In the automatic mode, the system controller determines the optimum settings for the instrument based on scene spectral radiances and dependent on other conditions already set by the operator, such as minimum allowable frame rate. In the manual mode, the operator sets the desired parameter to a given value through one of the interface busses, or through the back panel interface. These two modes allow for complete flexibility in instrument control, from fully autonomous operation, to completely manual control.

In either case, output from the instrument is fully spectro-radiometrically calibrated, unlike current spectro-radiometers which generally rely on an external computer for calibration and processing. Realizing that spectral images in-and-of themselves are only partially useful, SOC's instrument will include two very powerful processing modes. First, any desired spectral response function can be loaded into the instrument. Internal electronics will then integrate the product of the response curve and the measured spectral radiances to allow emulation of any type of SWIR/MWIR sensor system (or ultimately any VIS-LWIR sensor). Three such integrals can be performed and output simultaneously. Second, and extremely important to non-destructive inspection, is spectral matched filtering. In this mode, a desired relative spectral radiance to search for is either entered into, or measured by, the instrument. Several internal matched filtering algorithms can then be employed to filter scene spectral radiances against the desired radiance; any objects in the scene possessing the desired relative spectral radiance will appear bright, while other objects will appear dim.

These two processing modes, in addition to monochromatic imaging and spectral scanning, will produce an instrument with unsurpassed speed and flexibility, just as they have already in SOC's visible instrument. To allow for immediate and direct data monitoring, standard RGB RS-170 channels will be used for output. 12 bit digital data will also be output from the instrument.

1.4 Imaging Spectrometer Detailed Description

The first step in generating and processing spectro-radiometric imagery is capturing raw spectral images. SOC proposes to develop a circular variable filter-based (CVF) spectral imager operating from about 1.5 μ m to about 5.5 μ m, analogous to our already developed visible instrument. Figure 1-13 shows a representation of the spectral imager head using a refractive objective lens, while Figure 1-14 shows the same head, but with a Swarthchild reflective objective lens.

UNCLASSIFIED

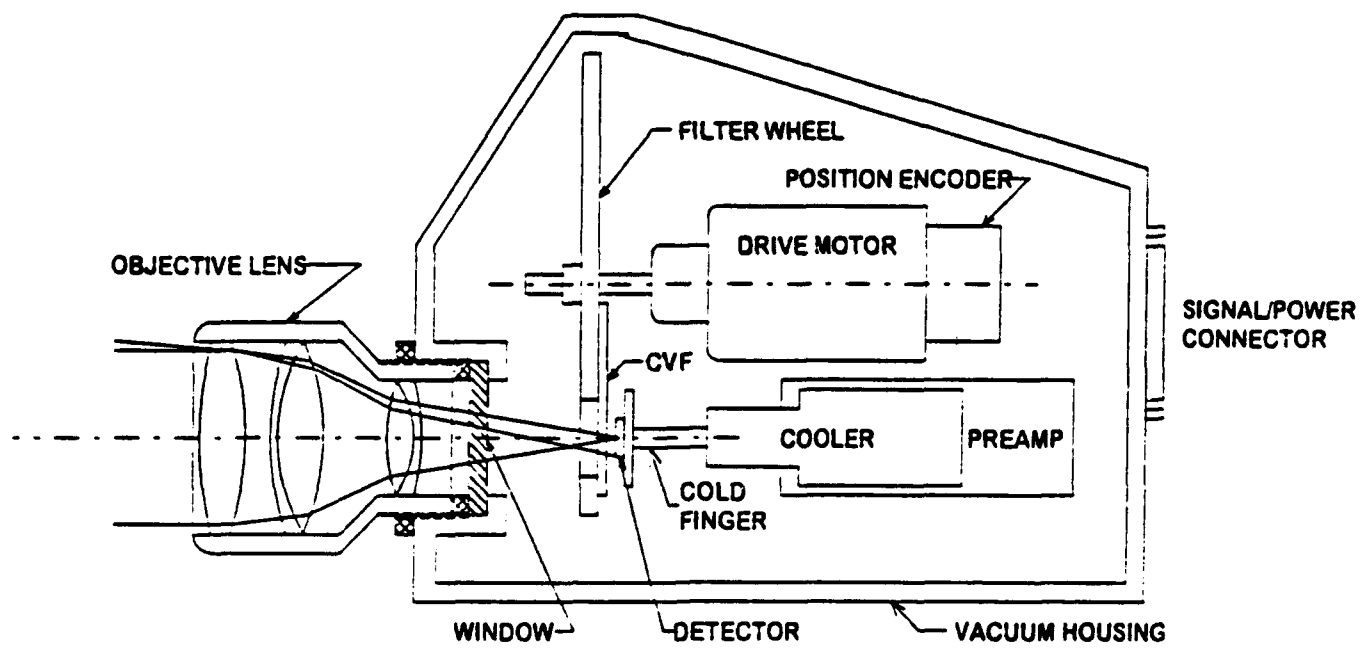


Figure 1-13. CVF-Based High Speed Spectral Imager, Refractive Version.

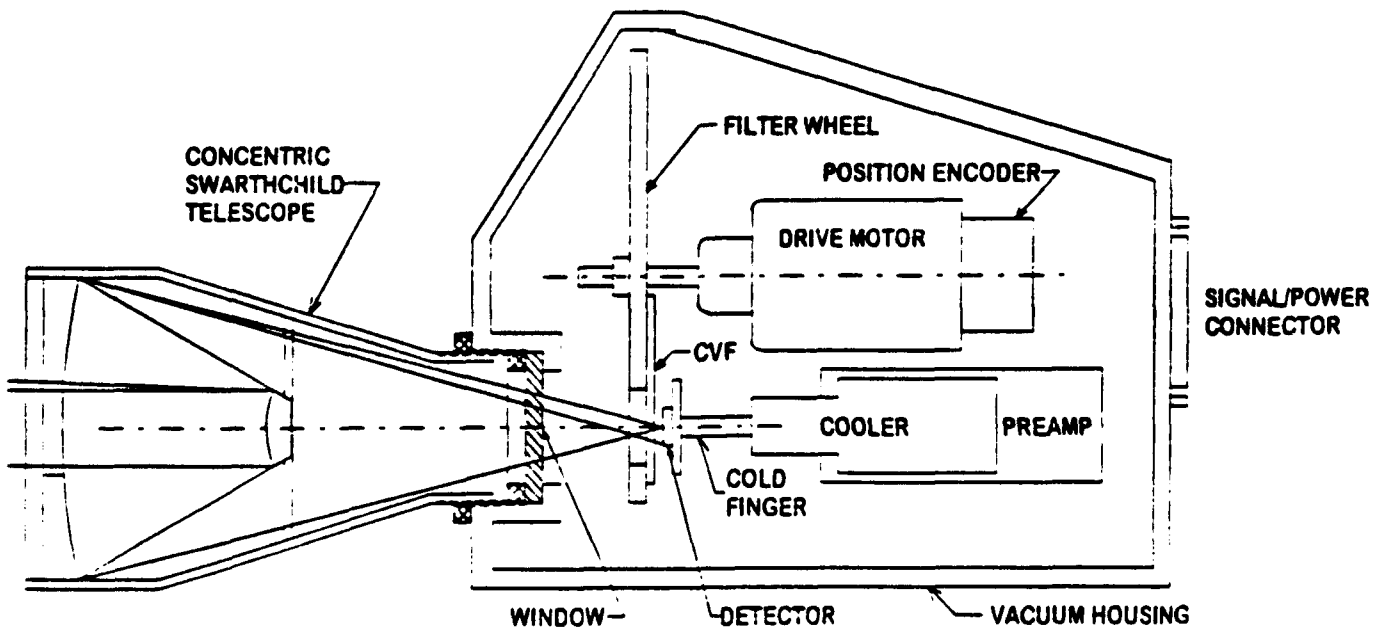


Figure 1-14. CVF-Based High Speed Spectral Imager, All Waveband Version.

UNCLASSIFIED

1.4.1 Objective Lens

An F/1.8 input objective with at least a 10° field of view will image the scene on to a narrow-band CVF. When viewing high spectral radiance objects, a precision iris controlled by the instrument (or operator) will stop down the lens as necessary. Focus will also be controllable through the instrument. If a commercially available lens is not found which will meet instrument requirements, then Surface Optics will custom design the optics using its in-house design capability and previous experience in designing custom optical assemblies.

1.4.2 Circular Variable Filter

Spectral information from the objective's image is then gleaned by a narrow-band SWIR/MWIR circular variable filter. Comprising two segments, this filter will vary its center wavelength from approximately $1.5\mu\text{m}$ to $5.5\mu\text{m}$ as it rotates 360°, and will have a passband of approximately 1.5% FWHM of the center wavelength. Such filters are available as standard technology from OCLI. Position of the filter will be encoded to 4,095 points per revolution, ensuring accurate determination of exact wavelength being viewed. As shown in Figure 1-15, a narrow-band dielectric filter's bandwidth varies with cone angle of incident light. This graph was generated with data from OCLI¹ based on a filter's center wavelength shift versus angle of incidence of collimated light.



Figure 1-15. Filter Bandwidth vs. Cone Angle of Illumination.

¹ Martin L. Baker and Victor L. Ten, "Effects of the Variation of Angle of Incidence and Temperature on Infrared Filter Characteristics", Applied Optics, Vol. 6, No. 8, pp. 1343-1351 (August 1967).

UNCLASSIFIED

As this figure shows, a 1.5% filter will see a negligible increase in its bandwidth when used in a fast F/1.8 system (cone angle = $\pm 15.5^\circ$). Hence, the imaging spectrometer portion of this instrument will have tremendous light gathering capability. The CVF is also temperature stable, exhibiting a center wavelength change of only about 70ppm/ $^\circ\text{C}$, or only $\pm 0.6\%$ over the temperature range of -55°C to 125°C . This is less than half a bandwidth change, or only 15 nm at 2500 nm for extremely harsh environmental conditions (note that SOC is not currently proposing to develop the instrument capable of operating over the full military temperature range. The range is given by way of example only).

Any method of spectral scene generation, be it CVF, grating, LCD, AOTF, or fourier transform, has its own set of advantages and disadvantages. For a high-speed spectral scanning system such as this instrument will employ, a grating based spectrometer would be very difficult to implement. LCD filters and AOTFs offer the attractive benefit of random access, no moving parts, and good resolution, but suffer from requiring very small cone angles to maintain bandwidth. Since the AOTF merely creates an index grating within its birefringent crystal, using a large cone angle has the same effect as illuminating the grating at a range of incident angles simultaneously, thereby increasing its bandwidth. Both LCD and AOTF also polarize the incident light, the AOTF through its birefringence, the LCD through an entrance polarizer necessary for proper operation. Hence, these devices provide a fixed polarization view of the scene, an artifact which can give an erroneous answer for the true spectral radiance of a scene. Fourier transform's biggest drawback is the tremendous processing demand placed on the processor just to generate the spectrum even before calibrating and analyzing it. An FTIR based system will also introduce some polarization into the image from its beam splitter. The CVF based system, although not able to provide the spectral resolution of, say, an AOTF at small cone angle, has several distinct advantages, including: very good spectral resolution, even with very fast optics; polarization insensitivity; high-speed scanning; compactness, stability, and durability. One of the major goals of the Phase I effort was to re-evaluate these various methods of spectral imaging and to decide on the one most appropriate for this effort. Details of the study are presented in the first progress report. Based on this study, CVF technology still appears to be the best choice for this instrument. Hence, a CVF-based spectrometer will be used in the proposed instrument.

1.4.3 Imaging Array

Output from the CVF will be imaged onto an area detector array, providing the spatial imaging of the system. Several different types and configurations of arrays were considered during analysis of the proposed instrument conducted under the Phase I effort, including Platinum-Silicide (PtSi), Mercury-Cadmium-Telluride (HgCdTe), and Indium-Antimonide (InSb). Based on quantum efficiency, readout noise, imaging format, exposure control, speed, and availability, an InSb appears to be the best choice for this system, although Rockwell's SWIR/MWIR HgCdTe is also a strong contender. InSb arrays from both Amber and Litton Electron Devices were considered. Presented here is the faster array made by Litton. This array, a 16-port 256 x 256, variable exposure array with a maximum exposure rate of 1,200 exposures per second appears to be the best choice for the instrument; the array will be used at half speed of 600Hz in order to directly use existing electronics. Note that generating 600 exposures per second, each containing 65,536 pixels, requires a data rate of over 39MHz. Digitizing such a stream to 12 bits and then processing is easily within SOC's capability; our

UNCLASSIFIED

visible instrument, for instance, runs a 256 x 192 array at a 725Hz burst rate, requiring 12 bit digitization at a 40MHz rate.

To compensate for band-to-band variances in spectral radiance and to effectively freeze the CVF's rotation (as detailed in Section 1.4.5), controllable integration time is necessary. Several different approaches can be used to effect variable integration time. In the visible band, this is simple task accomplished merely by gating, on and off, an image intensifier. In the infrared, such a technique can not be used since no photocathode material is available with a work function as low as a thermally-generated photon's energy. Mechanical shuttering could be used, but a shutter with the required aperture and response time (sub millisecond) would be extremely difficult to develop and likely unreliable; hence, this is not a viable option. Fortunately, electronic techniques can be used to effect variable integration time. The proposed array is a random access photodiode array. Each photodiode integrates charge on an associated capacitor. Analog field-effect transistor switches then allow readout of each pixel. The proposed array offers the ability to reset any sixteen pixels and read any other sixteen pixels in a 200ns clock cycle. Resetting pixels an appropriate number of clock cycles before reading them allows variable integration time. This can be visualized as a window moving through the array, with pixels at the leading edge of the window held in reset, pixels within the window integrating, and pixels at the trailing edge of the window being read out. Integration times are then variable from 1/4096th of the frame time up to the full frame time. At minimum frame time of 1.6 milliseconds, integration times are variable from 400ns to 1.6 ms in 400ns increments.

Pixels on the array measure 38 μ m square with an effective optical fill factor of 90%, so that overall array size is 9.73mm square. To yield a total FOV of $\pm 5^\circ$, the input objective lens must have a 55mm focal length. Pixel IFOV is then .7 mrad. Trade-off exists between FOV and IFOV. If IFOV is dropped to, say, .5mrad, than FOV decreases to $\pm 3.7^\circ$ as focal length increases to 76mm. As previously mentioned, part of the detailed design to be carried out during the initial part of the Phase II effort will be to define (and design, if necessary) the input lens. If possible, a lens with zoom capability will be incorporated into the instrument.

Needless to say, the array must be cryogenically cooled for proper operation. Cooling will be provided by a compact, closed-cycle stirling cryogenic cooler, thermostating the array at 77°K. If possible, a microcooler such as is available from Inframetrics or Ricor will be used. These coolers provide good cooling capacity in a cooler which can fit in the palm of a hand, and have a demonstrated life of over 2000 hours. Longer life and lower cost, however, can be achieved by using a somewhat larger cooler such as are available from Hughes. The exact cooler to be used will be specified early in the detailed design phase.

By placing the detector immediately behind the CVF, dramatic decrease in background noise will be realized. Since the CVF achieves its blocking characteristics through reflection rather than absorption, emissivity of the filter is extremely low. Hence, background from the filter reaching the detector will be minimal, since close proximity to the detector ensures that the detector sees its own reflection at only 77°K.

1.4.4 Internal Calibration Sources

To allow the instrument to maintain calibration with a minimal amount of laboratory calibration, MIDIS will contain an internal reference. SOC is very familiar with the

UNCLASSIFIED

manufacture and use of blackbody sources, as much of our instrumentation employs these sources. For this instrument, a thermo-electrically controlled reference will be employed. The reference will consist of two blades connected to either side of the cooler; one cooler, then, will produce both a hot and a cold reference, both of whose temperatures will be monitored to allow correct gain and offset compensation. During the Phase I effort, inclusion of a shutter designed to exploit narcissus, thereby allowing the cooled detector to view itself for offset correction, was studied. Although implementation of such a shutter is feasible, use of the two-temperature reference should allow better gain and offset compensations. Absolute spectro-radiometric calibration data will be generated at time of assembly by having the radiometer view a source of known spectral radiance (blackbody). Immediately after this, the internal reference will be viewed. By viewing the internal source later, calibration data can be appropriately scaled to compensate for any gain variations.

In reality, inclusion of the internal high temperature reference is not absolutely necessary provided adequate attention is paid to ensure thermal stability of readout electronics. In SOC's visible instrument, for example, no internal reference is used. Periodic recalibration is necessary as components (mainly the intensifier) age. By using an internal reference in MIDIS, interval between recalibration can be extended.

1.4.5 Spectral Operating Modes

The proposed MIDIS instrument does much more than just capture spectral images. MIDIS uses internal electronics to process the raw data, turning it into calibrated spectro-radiometric data. Realizing that generating a spatial and spectral cube of calibrated radiances is only a small part of the battle, SOC's instrument will include custom electronics to calibrate and then analyze the data. Simple spectral image scanning or staring is also possible. When sensor emulation or spectral matched filtering is implemented, many individual spectral images will be processed to yield the resulting output image. Hence, a distinction must be made between individual images and the conglomerate of processed images. To this end, individual spectral images will be, and already have been, referred to as exposures; processed output images will be referred to as frames, consistent with normal video cameras.

Dependent on the processing desired, the spectrometer can collect spectral images in two distinct modes. First, if a single wavelength is to be viewed repeatedly at rates of 30Hz to 600Hz, the CVF is held stationary at the desired wavelength. For exposure rates above RS-170 standard video rates of 30Hz frame rates, all images are output over the high-speed digital interface, while a subset of these will be output as RS-170 video, e.g., at exposure rates of 600Hz, every 20th exposure will be output as video data. Second, if spectral images are to be processed, or if sequential spectral image scanning is desired, the CVF will rotate at a rate slaved to the overall frame rate.

1.4.5.1 Integration Time Limits For Spectral Scanning

When the CVF is rotating, integration time on the array must be controlled to effectively freeze the rotation of the filter. If integration time were not properly controlled,

UNCLASSIFIED

then bandwidth spreading would occur as the CVF changed its center wavelength while a pixel was integrating. Assume that a pixel views a wavelength of λ_1 at the start of the integration time. If the CVF rotates at a rate of N revolutions per second, then at the end of an integration period Δt , the same pixel will now view a wavelength of $\lambda_2 = \lambda_1 + (\lambda_{\max} - \lambda_{\min}) \cdot N \cdot \Delta t$, where λ_{\min} and λ_{\max} are respectively the CVF's minimum and maximum wavelengths. The new filter response curve, $F(\lambda, \lambda_c')$, for this pixel will then be the integral of the nominal filter response, $F(\lambda, \lambda_c)$, over the range of center wavelengths from λ_1 to λ_2 :

$$F(\lambda, \lambda_c') = \int_{\lambda_1}^{\lambda_2} F(\lambda, \lambda_c) d\lambda_c$$

Effect of this change in filter response function is shown graphically in Figure 1-16, which plots the increase in filter bandwidth for varying effective slit width normalized to filter bandwidth, i.e., $s = (\lambda_{\max} - \lambda_{\min}) \cdot N \cdot \Delta t / \Delta \lambda$. This plot also shows the change in effective center wavelength which is simply $(\lambda_1 + \lambda_2) / 2$.

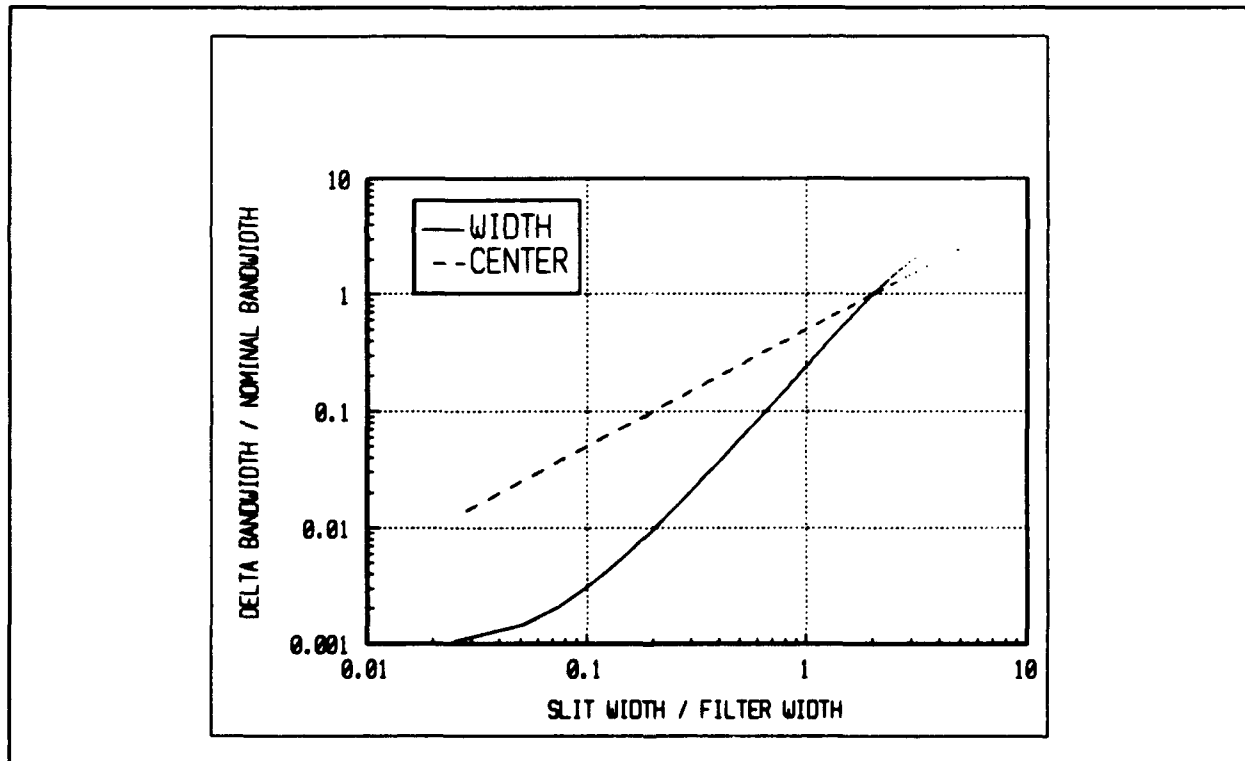


Figure 1-16. Effect of Integration Time on Filter Bandwidth.

Arbitrarily choosing the maximum allowable increase in filter bandwidth to be 20% defines the maximum allowable integration time for any filter rotation rate. From the above

UNCLASSIFIED

graph, an increase of 20% will occur when the filter has changed by 82% of its bandwidth, or using the previous nomenclature, when $\lambda_2 - \lambda_1 = 0.04 \mu\text{m}$ at $3.5\mu\text{m}$. This bounds the maximum integration time for a given filter rotation rate as $\Delta t_{\max}(N) = 0.04/(\lambda_{\max} - \lambda_{\min}) \cdot N$. For the proposed filter with a spectral coverage of $4 \mu\text{m}$, and at filter rotation rate of 30 Hz, this equates to a maximum integration time of about $350\mu\text{s}$. Note that using a CVF allows a trade-off between sensitivity and bandwidth: when viewing low radiance (cold) objects, longer integration times are required. If no decrease in spectral resolution is required, then CVF speed must be decreased in proportion to the increase in exposure time. If, however, speed is required, then longer integration times will merely result in an effective increase in bandwidth of the spectral imager.

1.4.5.2 Number of Spectral Exposures per Frame

As detailed next, spectral scanning mode of the instrument can be further broken down into two sub modes. These two modes are distinguished by their differing spectral dispersion across the height of the array.

When the instrument collects a set of spectral images for sensor emulation or spectral matched filtering, the total number of images that it can collect in a given frame is dependent on frame rate, the array readout time, and any dead time between readouts. To maximize the number of spectral images which can be collected and then processed by the instrument, the array must be read out continuously. That is, as soon as the 256th row is read out of the array, read out must begin again immediately at the first row. Under this condition, the imager can acquire M spectral images for a given filter rotation rate N as defined by

$$M = \frac{1}{N \tau_{\text{exp}}}$$

where τ_{exp} is the image readout time for a given spectral exposure. For the proposed array with a minimum full image readout time of 1.6 ms, and at a 30Hz frame rate, each frame can contain 20 spectral images. Maximum number of spectral exposures per frame will increase inversely with overall frame rate, up to a maximum of at least 50 as dictated by spectral range and bandwidth requirements. Number of spectral exposures collected versus frame rate in maximum collection mode is shown in Figure 1-17.

UNCLASSIFIED

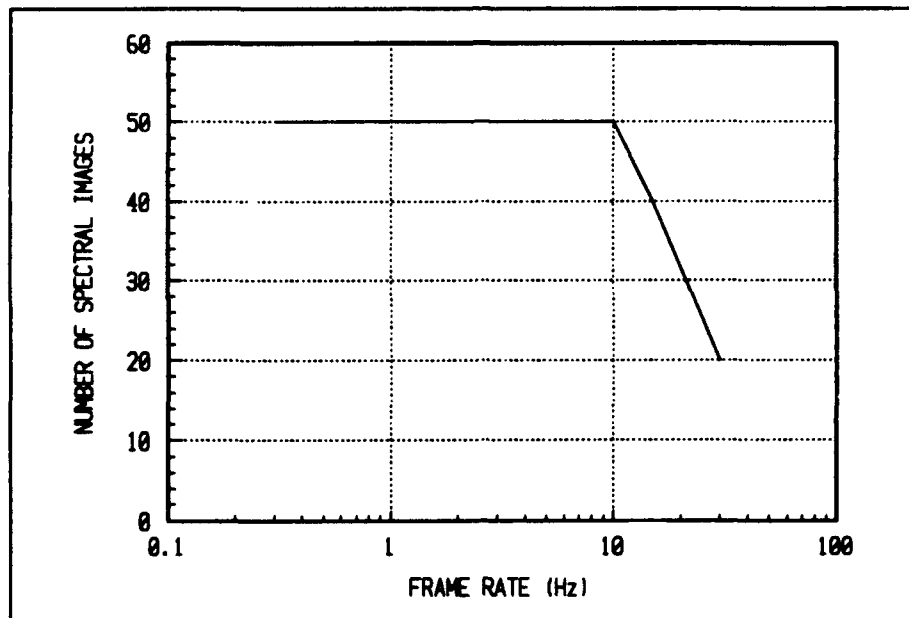


Figure 1-17. Number of Spectral Images vs. Frame Rate.

Note that the caveat was made above that this curve is for the maximum number of exposures per frame, i.e., each exposure follows its predecessor immediately. At a nominal radius of 1.75", the filter exhibits a lineal spectral dispersion of $4\mu\text{m}/(2\pi \cdot 1.75")$, or $.36\mu\text{m}$ per inch, or $.014\mu\text{m}$ per millimeter. The array covers an area of $9.7\text{mm} \times 9.7\text{mm}$. If the array is situated such that its projection onto the CVF places the center row on a radial vector, then $\pm .068\mu\text{m}$ exist across the array. This means that each pixel views the scene at the resolution of the filter (1.5%), but at a slightly different wavelength. At $4\mu\text{m}$ at the center of the array, for instance, pixels in the first row view a wavelength of $4.07\mu\text{m}$, while pixels in the last row view a wavelength of $3.93\mu\text{m}$. This dispersion exists with the CVF stationary. If the CVF is rotating during exposure and readout of the array, then the wavelength illuminating any given row will change during the readout. As explained previously, the variable integration time of the array can be viewed as a window of exposure and readout scanned across the rows of the array. The rate at which this window scans across the array and the rotation of the CVF will operate together to vary the effective dispersion across the array. If the exposure window scans in the same direction as the filter is rotating, then the rates of both can be synchronized so that each row is exposed to the same wavelength as any other row. For a given full-array readout time τ_{exp} , this rotation rate is given explicitly by the following equation:

$$N_{\text{monochromes}} = \frac{\Delta\lambda_{\text{array}}}{\tau_{\text{exp}} (\lambda_{\text{max}} - \lambda_{\text{min}})}$$

where $\Delta\lambda_{\text{array}}$ is the total spectral dispersion across the array with the CVF stationary, or $.136\mu\text{m}$. Using the minimum readout time of 1.6 ms means that the monochrome frame rate

UNCLASSIFIED

is 21.2Hz. In order to maintain the frame rate at an integer submultiple of the standard 30Hz video rate, a 15Hz rate would be used with 30 spectral images per frame. The relationship between spectral dispersion across the rows of the array versus frame rate and maximum number of exposures per frame is shown in Figure 1-18. Note that this figure plots the total array dispersion, not the plus or minus value.

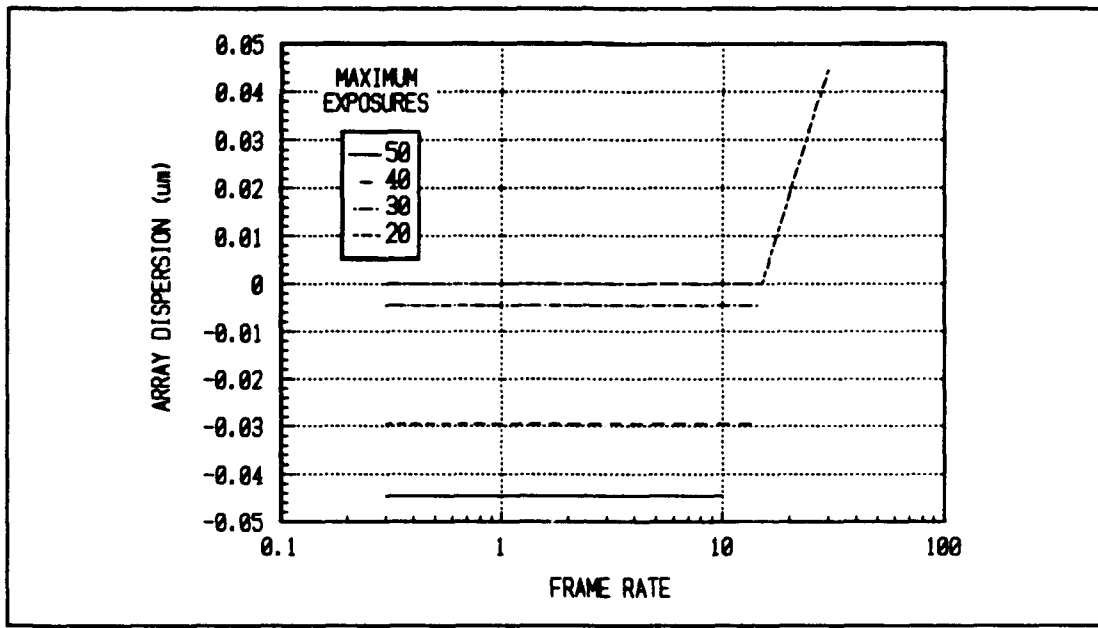


Figure 1-18. Total Spectral Dispersion Across Array vs. Frame Rate.

Note that for any number of exposures per frame at any frame rate, total dispersion across the array is less than $\pm .022\mu\text{m}$, or \pm one-half bandwidth at $3\mu\text{m}$. At any frame rate and number of spectral exposures per frame, dispersion across the array will be constant. Processing electronics will automatically account for this dispersion in applying the correct spectro-radiometric calibration factors and when performing spectral response curve integration and matched filtering.

In summary, when the system is scanning spectrally, it can operate in two different modes: First, it can maximize the number of spectral images per frame based on frame rate. Second, it can minimize spectral dispersion across the array based on desired number of spectral images.

1.4.6 Spectrometer Energy Throughput

In order to determine the expected performance of SOC's and JPL's proposed MIDIS, detailed analysis of the light gathering capability of the system was performed during the Phase I effort. Since such analysis is key to the expected performance of the instrument, a brief review of the throughput analysis will be conducted here. A short digression into

UNCLASSIFIED

radiometry will help to clarify how the instrument works. Assume that a detector of area A_p , linear dimension l_p , sits behind a lens of arbitrary focal length F and collecting area A_l , and is viewing a scene a distance D from the lens. Assume also that the scene possesses a spectral radiance $L(\lambda)$ in units of $\text{W}/(\text{cm}^2 \cdot \text{sr} \cdot \mu\text{m})$. The lens will project the detector to an area A_{pp} on the scene. At a distance D from the scene, the lens subtends a solid angle Ω_l . Therefore, total power collected by the system and deposited, neglecting transmission or scattering losses, on the detector is $L(\lambda)A_{pp}\Omega_l$. Here, Ω_l was assumed small. If the angular distribution of radiance were to change significantly over the angle subtended by the lens, then explicit integration of spectral radiance over the lens's subtended angle would have to be performed. The preceding notation, however, is not easy to use since both A_{pp} and Ω_l depend on the distance D to the object. Introduce a new parameter, Ω_p , the solid angle subtended by the detector (pixel) at the focal distance from the lens. All these quantities are shown in Figure 1-19.

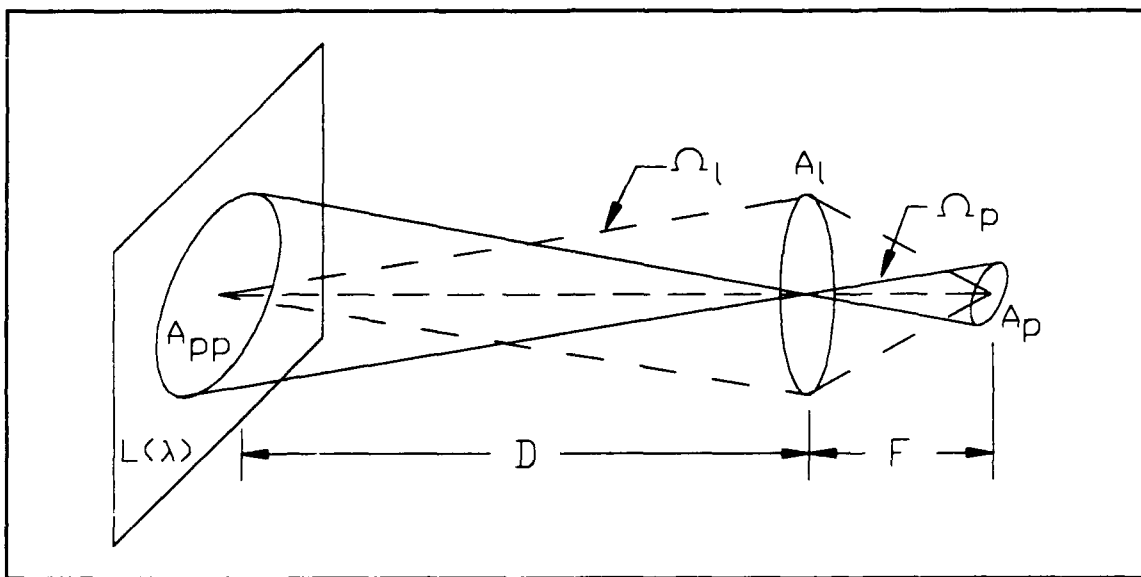


Figure 1-19. Definition of Terms for Energy Collection Analysis.

A simple derivation will show that given the condition of $D \gg F$ (i.e., image plane and focal plane of lens nearly coincident), and $l_p \ll F$, then the product $A_{pp}\Omega_l \approx A_l\Omega_p$, with the degree of approximation being dependent on the relative magnitudes of F , D , and l_p . For example, an F/1.8 lens with $F = 55\text{mm}$ viewing a scene 1 meter away and illuminating a pixel $38\mu\text{m}$ on a side, will have a $A_l\Omega_p$ product which is only .022% greater than the actual collection product of $A_{pp}\Omega_l$.

With the above description in mind, neglecting path radiance contributions for now, the spectral power incident on a given pixel in the imaging array, through an optical train of transmission $T_o(\lambda)$, through atmosphere of transmission $T_a(\lambda)$, but without any spectral filtering is

UNCLASSIFIED

$$P(\lambda) = L(\lambda) \Omega_p A_i T_o(\lambda) T_e(\lambda) \quad \left[\frac{W}{\mu m} \right]$$

If now a spectral filter with response function at λ_c of $F(\lambda, \lambda_c)$ is introduced into the optical train, the total power striking a pixel is

$$P(\lambda_c) = \int L(\lambda) \Omega_p A_i T_o(\lambda) T_e(\lambda) F(\lambda, \lambda_c) d\lambda \quad [W]$$

If the detector has a quantum efficiency $\eta(\lambda)$, and the pixel is exposed to the above power level for an integration time of Δt , then the total number of electrons collected by a pixel is

$$N_e(\lambda_c) = \int \frac{L(\lambda) \Omega_p A_i T_o(\lambda) T_e(\lambda) F(\lambda, \lambda_c) \eta(\lambda) \Delta t}{h \frac{c}{\lambda}} d\lambda \quad [\text{number}]$$

Here, the division by hc/λ converts a spectral radiance to a spectral photon radiance. This is the desired throughput equation for a generalized spectro-radiometer. Also note that given a focal length F much greater than pixel dimension l_p , the product $A_i \Omega_p$ for a lens of f-number F/no can be rewritten as

$$A_i \Omega_p \approx \left[\frac{\pi l_p}{4 F/\text{no}} \right]^2 \quad [m^2 \cdot sr]$$

1.4.7 Spectral Imager Noise Levels

To correctly quantify system performance, an expression for the radiometer's noise level must also be generated. Four main sources will be considered, namely signal shot noise, background shot noise, detector noise, and readout noise.

Shot noise is an intrinsic part of any photon flux because of the discrete nature of photons. Generation of photons from a time independent photon generation source, i.e., a coherent source, is governed by Poisson statistics.² For a non coherent chaotic source, i.e., a greybody, Bose-Einstein statistics govern the emission events. Hence the RMS fluctuation in photon flux from an incoherent source is given by:

² Eustace L. Dereniak and Devon G. Crowe, Optical Radiation Detectors, Wiley-Interscience, pp. 14-19 (1984).

UNCLASSIFIED

$$\sigma_s = \sqrt{\bar{n} \frac{e^{h\nu kT}}{e^{h\nu kT} - 1}}$$

where the subscript "s" indicates the noise is inherent in the signal and \bar{n} is the mean number of photons during the observation period. Note that the variance for a Bose-Einstein distribution is merely the variance of a Poisson distribution multiplied by the Boson factor. At 1500°C and at 5 μm , for example, this factor has the value of 1.25, indicating an increase in the RMS noise over a Poisson distribution of only 11%. Hence, for the proposed spectro-radiometer's operating range, a Poisson distribution adequately describes the statistical fluctuations in the photon flux.

Since the detector cannot be cold-stopped perfectly to prevent all unwanted background radiation from reaching the detector, some charge will accumulate in a pixel from background radiation. Representing an offset, this background level is subtracted from the signal as part of the dark level previously described. A shot noise will nevertheless be contributed by this background since it is governed by the same statistics as the signal. Optics will also contribute a background noise since, for a reflective system, the optics posses a non-zero emittance; similarly, transmissive optics will also contribute from their non-zero absorptivity. Note, however, that placing the detector immediately behind the CVF will greatly reduce background noise since all background radiance will be forced to pass through the CVF, thereby dramatically reducing the bandwidth of the background signal.

Even if readout electronics after the focal plane assembly were perfectly noiseless, the array itself would generate noise. This is a specification given by the manufacturer. For most conditions, high-speed array readout will be dominated by the read-out electronic's noise. Careful attention must be paid to minimizing this source.

For the above stated noise sources, total system noise, referenced to number of electrons is given by

$$\sigma_{\text{total}} = \sqrt{\sigma_s^2 + \sigma_{\text{bg}}^2 + \sigma_{\text{array}}^2 + \sigma_{\text{readout}}^2}$$

where the "bg" subscript indicates the background. By translating this RMS noise electron level back through the imaging system, a Noise Equivalent Spectral Radiance (NESR) can be generated as:

$$\text{NESR}(\lambda_c) = \frac{\sigma_{\text{total}} h \cdot c}{A_i \Omega_i \Delta t \int T_s(\lambda) T_e(\lambda) \lambda F(\lambda, \lambda_c) \eta(\lambda) d\lambda}$$

For SOC's and JPL's proposed MIDIS, expected system performance can now be generated merely by substituting in the appropriate parameters in the equations for signal and noise. Salient parameters are: lens $F/ \# = 1.8$; $l_i = 38\mu\text{m}$ (~90% fill factor); $T_e = 25\%$; $\eta(\lambda) = 50\%$, $1.5\mu\text{m} < \lambda < 5\mu\text{m}$; $f(\lambda, \lambda_c) \approx \text{gaussian with fwhm} = 0.015\lambda_c$; $\sigma_{\text{array}} = 400$; $\sigma_{\text{readout}} = 1000$. The readout noise of 1000 electrons is based on performance already exhibited by SOC's visual RTISR which runs the array at a 40MHz readout rate. Signal noise, of course, is

UNCLASSIFIED

dependent on the signal level. Atmospheric transmission is assumed to be from a three meter path at sea-level.

Target radiance comprises three main sources, self emitted, reflected solar, and reflected ambient earthshine, including skyshine. At low temperature and for wavelengths less than $3\mu\text{m}$, even a low reflectance target will generate significant portion of its radiance through reflected solar or other irradiance. For analysis purposes, total radiance was assumed to be from the red-painted sample at 300°K , illuminated by a 2800°K quartz-tungsten-halogen lamp producing a luminance level of about 1000 cd/m^2 (about $1/40^\text{th}$ the brightness of noon-time sunlight on a white lambertian reflector). Path radiance was ignored for now. Figure 1-20 shows the target's spectral radiance and MIDIS's predicted NESR. Integration time is used as a parameter. Figure 1-21 shows the same information, but with readout noise reduced to only 200 electrons. This shows the importance of minimizing readout noise. Careful attention will be given to minimizing this source during the initial Phase II detailed design. Remember that in spectral staring mode, exposure rates of 600Hz can be attained with 1.6 ms integration times. In the spectral scanning mode, maximum allowable integration time is a function of overall frame rate. For 30Hz frame rates, maximum integration time is $350\mu\text{s}$; at 3Hz it is 3.5 ms; at .3Hz it is 35ms. Note that at low temperature and short integration time, the smooth curves show that the device is readout noise limited, as would be expected with wideband readout electronics. As target temperature and/or integration time increases, the instrument becomes signal shot noise (statistically) limited. These are excellent NESRs. In fact, the AOTF based imager which NASA Goddard Space Flight Center plans to send to Pluto exhibits an NESR at equivalent exposure times an order of magnitude greater than MIDIS (larger NESR is worse).

An alternate way to view the above information is to plot the signal to noise ratio versus temperature at various wavelengths. Figure 1-22 is a plot of SNR versus target temperature for an integration time of $250\mu\text{s}$.

Since SOC's proposed MIDIS performs more than just spectral image collection and calibration, noise performance can be better on a frame-to-frame basis than on an exposure-to-exposure basis as shown above. For instance, assume that the instrument is viewing a scene of spectrally constant radiance so that all bands receive essentially the same signal. Assume also that the instrument is collecting data at a 600Hz exposure rate, 30Hz frame rate so that 20 spectral images are collected in a frame. Finally, assume that the instrument is emulating a broadband $1.5\mu\text{m}$ to $5.5\mu\text{m}$ imager, so that each spectral point is weighted equally and integrated spectrally by the processing electronics. With the above assumptions, signal level is effectively increased by a factor of 20, whereas the noise level increases by only a factor of $\sqrt{20}$ since exposure-to-exposure noise is uncorrelated. Figure 1-23 shows the signal-to-noise performance of MIDIS emulating a $1.5 \mu\text{m}$ to $5.5 \mu\text{m}$ imager versus frame rate and target temperature. Target radiance assumptions are the same as used to generate the previous graphs. Note that as frame rate decreases from 30Hz, SNR rises on a steep slope, then rises less rapidly at frame rates less than 10Hz. This is due to the fact that as frame rate decreases from 30Hz to 10Hz, maximum integration time increases from $350 \mu\text{s}$ to $1050 \mu\text{s}$, and total number of spectral exposures per frame increases from 20 to 50. Below 10Hz, number of exposures per frame remains constant while maximum integration time continues to increase. The graph also shows the noise limit due to the internal processing quantization of 16 bits, and more importantly, the output quantization of 12 bits.

UNCLASSIFIED

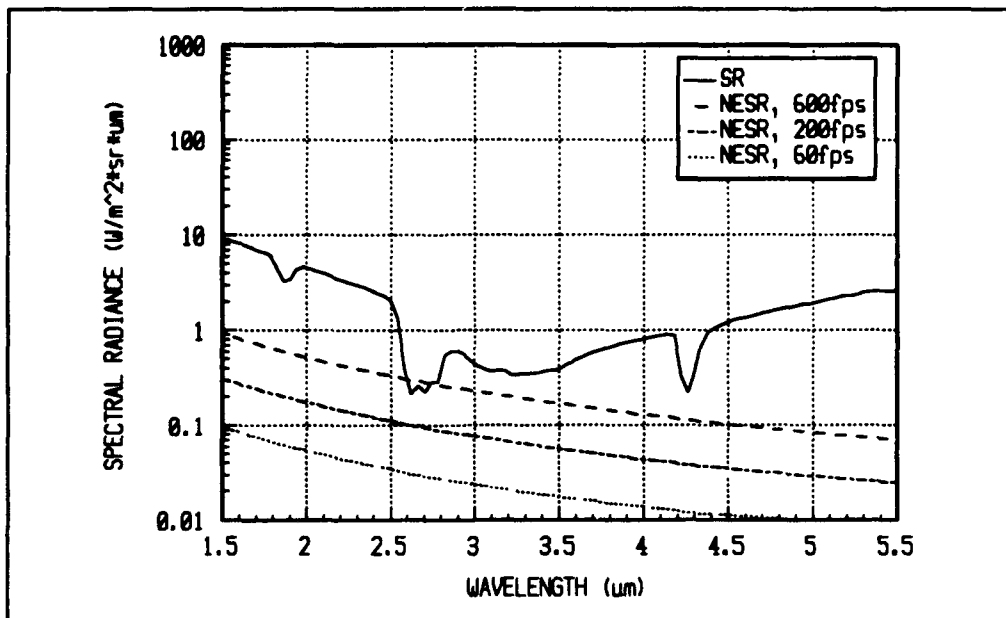


Figure 1-20. NESR and Target Radiance for Spectral Imager.

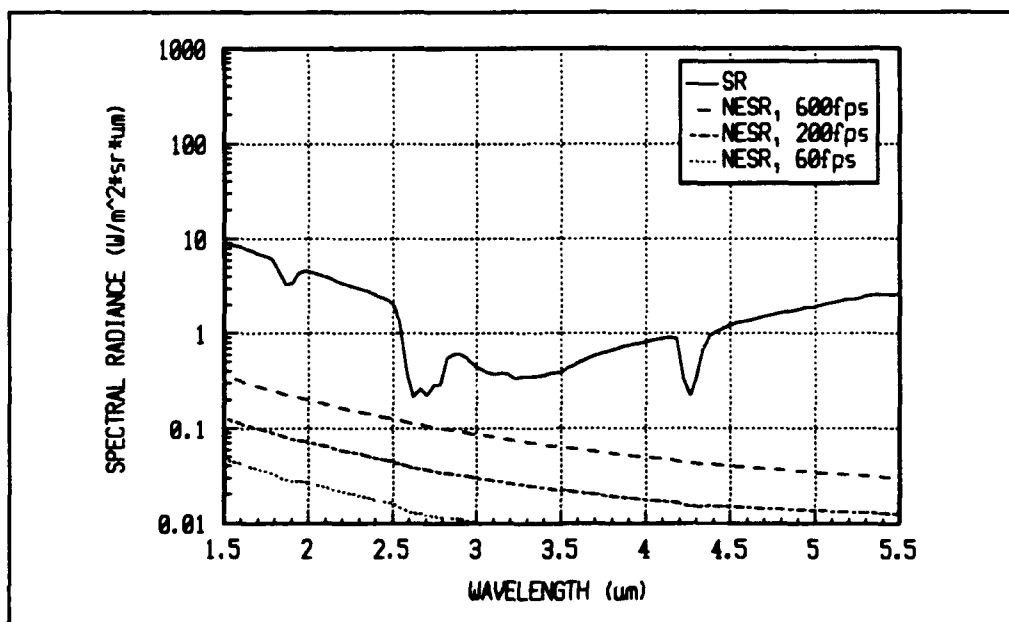


Figure 1-21. NESR and Target Radiance for Reduced Readout Noise Imager.

UNCLASSIFIED

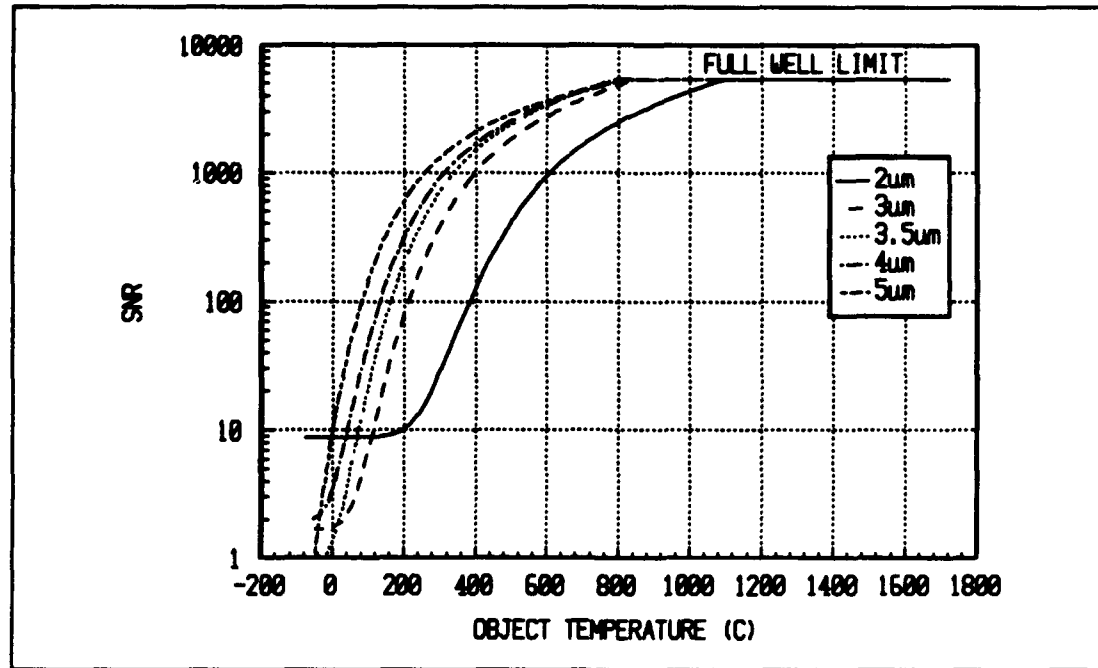


Figure 1-22. SNR vs. Target Temperature for 250 μ s Integration Time.

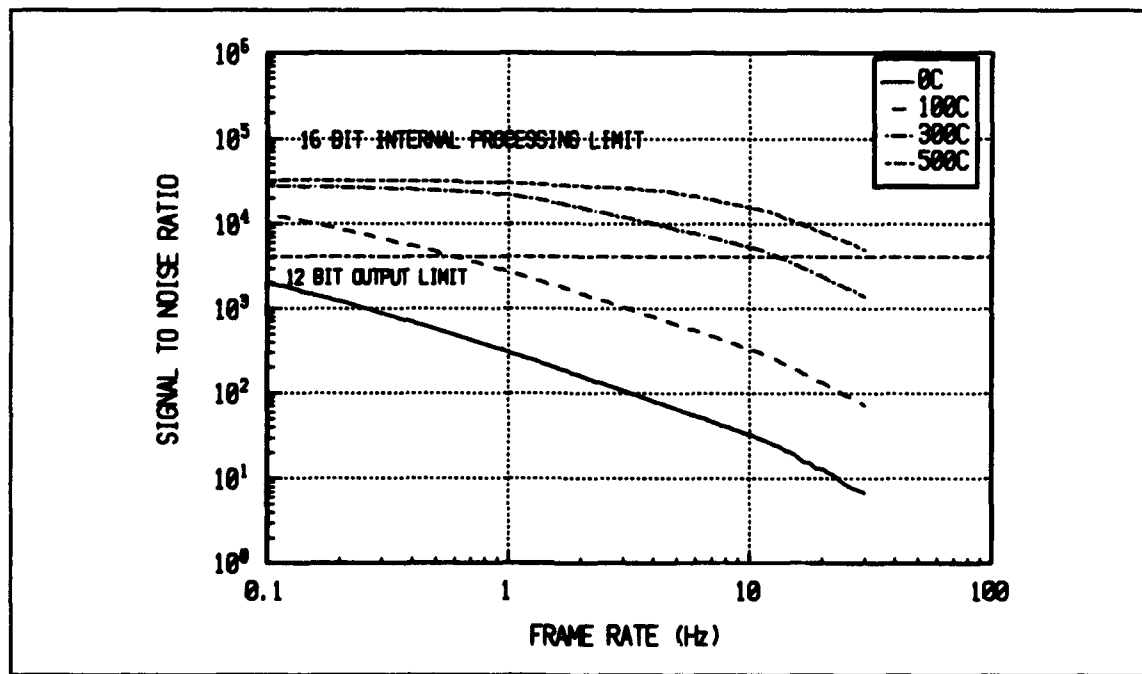


Figure 1-23. Frame-to-Frame SNR vs. Frame Rate, 1.5-5.5 Sensor Emulation.

UNCLASSIFIED

As the preceding analysis and accompanying graphs show, expected performance of SOC's MIDIS is tremendous. This instrument will offer the ability to view objects with temperatures varying over a large range while maintaining good SNR at extremely fast image rates. One final point to make about the imaging spectrometer section of the instrument is that it possess an incredible dynamic range. To quantify this, consider the effects of the variable aperture and integration time working together: Based upon assumptions about background photocharge generation, maximum background generation rate is about 5×10^7 e/sec at 5 μ m. With this generation rate, array will saturate in the absence of any other irradiance source in 600 ms since the full well capacity is 30×10^6 electrons. Maximum integration time, then, is about 500 ms, allowing some image charge to accumulate also. Minimum integration time for a 1.6 ms readout rate as stated previously is 400ns, but minimum used will be 5 μ s. This gives a dynamic range based solely on exposure time control of 500ms/5 μ s, or 100,000:1. Stopping down the lens from its maximum F/1.8 to F/18 (from 30mm aperture to 3mm aperture if $\pm 5^\circ$ FOV is used) provides an additional 100:1 dynamic range for a total of 10⁷:1. At the maximum exposure time, if 3×10^6 signal electrons are generated, SNR is $3 \times 10^6 / \sqrt{25 \times 10^6}$, or about 1000. If snr is allowed to fall to 10, then an additional two decades of dynamic range are acquired. Hence, maximum dynamic range is about 10⁹:1, or from a power point of view, 90dB. This means the instrument will be able to view purely emissive targets (no reflected energy) at 200°K at 5 μ m, all the way to a 6000°K target at 2 μ m, an enormous range indeed.

1.5 Processing Electronics

To this point, much explanation has been given to generating raw spectral images. Generation of images, however, is only a small part of the real goal of generating useful discriminants which can be used to classify, identify, track, or otherwise monitor a desired object, whether for NDI or other purposes. In order to generate useful discriminants from raw data, additional processing is necessary. Having a compact, high-speed spectral imager is of little use if a stand alone super-computer is necessary to process the data at the same rate as the imager generates it, or if a standard processor can process at only a fraction of the generation rate.

In order to effectively exploit the spectral images generated by MIDIS's imaging spectrometer, SOC's instrument will include a high-speed processing section. In addition to spectro-radiometrically calibrating each spectral and spatial pixel at the same rate that they are generated, the instrument will further process the spectrum for each spatial pixel, allowing real-time implementation of spectral response integration and spectral matched filtering. Spectral response integration allows the instrument to emulate any desired SWIR/MWIR imager by integrating the measured spectral radiances with any arbitrary response curve, so that the output at a given pixel, SE(p), is given by

$$SE(p) = \int L(\lambda, p) R(\lambda) d\lambda$$

where R(λ) is the spectral response curve of the sensor being emulated. SOC's visible-band instrument performs six such integrals simultaneously; only three, however, were actually

UNCLASSIFIED

used in operation. Hence, for the next development phase of this technology, only three such integrals will be performed simultaneously, thereby removing unused capability and further reducing electronic's size and power. An even more powerful processing operation to be implemented by the instrument is spectral matched filtering. Here, a desired relative spectral radiance to filter for is loaded into the instrument, either by direct measurement or through an interface bus. Several different filtering algorithms with varying degrees of sensitivity can then be implemented to filter each pixel's spectral radiance against the sought after radiance, with matching pixels appearing bright, while mismatched pixels are dim. A few of the possible algorithms are described below.

The dot product is a very simple filtering algorithm that treats each spectral radiance as an N-dimensional vector and simply computes the dot product of the two vectors. Formally, this algorithm is given by

$$C_{\text{DOP}} = \frac{\sum L(\lambda_n) F(\lambda_n)}{\sqrt{\sum L(\lambda_n)^2 \cdot \sum F(\lambda_n)^2}}$$

where $L(\lambda_n)$ is the measured spectral radiance at the n^{th} wavelength, and $F(\lambda_n)$ is the filter spectral radiance at the n^{th} wavelength. A major problem with this algorithm is that it is extremely broad. That is, the measured and filter radiances need only have roughly the same shape in order for the dot product to produce a high correlation value. The dot product generates the cosine between the two vectors acted upon by the algorithm. An N-dimensional vector can lie in any one of 2^N possible dimensional sectors, e.g., a three dimensional vector can lie in any one of 8 octants. Spectral radiances, however, are always positive, constraining radiance vectors to all lie in only one of their 2^N sectors. Hence, all vectors are necessarily forced to point in the same general direction, with the forced match becoming greater as more spectral points are added. How, then, can a tighter filter be implemented while still retaining spectral features?

The zero-mean dot product accomplishes this task. By removing the mean value from each spectral point, the shape of the spectral radiance curve is maintained, but the new zero-mean spectral radiance vector can now lie in any of the 2^N sectors of its N-space. Performing a dot product on the zero-mean radiance vectors then gives a tighter matching algorithm. This algorithm is given formally by

$$C_{\text{ZMDOP}} = \frac{\sum (L(\lambda_n) - \langle L(\lambda) \rangle)(F(\lambda_n) - \langle F(\lambda) \rangle)}{\sqrt{\sum (L(\lambda_n) - \langle L(\lambda) \rangle)^2 \cdot \sum (F(\lambda_n) - \langle F(\lambda) \rangle)^2}}$$

where the spectral radiance mean is given by

UNCLASSIFIED

$$\langle L(\lambda) \rangle = \frac{1}{N} \cdot \sum_1^N L(\lambda_n)$$

and similarly for $\langle F(\lambda) \rangle$. Close inspection of the above equation reveals that applying the zero-mean dot product to two spectral radiances is equivalent to treating those two radiances as sets of discrete random variables and computing the correlation coefficient between the two. Both the dot product and zero-mean dot product can also be applied to the derivative of the spectral radiances to further tighten their matching characteristics by simply replacing $L(\lambda_n)$ and $F(\lambda_n)$ in the above equations with $(L(\lambda_{n+1}) - L(\lambda_n)) / (\lambda_{n+1} - \lambda_n)$.

Another completely different type of matching algorithm can be formed by normalizing both the measured and filter radiances such that each encloses unity area, and subtracting the area "trapped" between the two curves from 1. For two identical spectral radiances, zero area will be "trapped", and the correlation value will be 1. As more and more area lies between the two curves, the correlation value will become smaller and smaller. For this algorithm, area is always defined as positive. This algorithm, the absolute differential area algorithm, is implemented formally by

$$C_{ADA} = 1 - \sum \left| \frac{L(\lambda_n)}{\sum L(\lambda_n)} - \frac{F(\lambda_n)}{\sum F(\lambda_n)} \right|$$

Although the absolute differential area algorithm is a tighter matching algorithm than the dot product, it suffers from the same problem as the dot product in that all spectral radiance values are positive; again subtracting the mean from each spectral radiance value and using the resultant radiance values in the above algorithm yields the zero-mean absolute differential area algorithm, given formally by

$$C_{ZMADA} = 1 - \sum \left| \frac{L(\lambda_n) - \langle L(\lambda) \rangle}{\sum L(\lambda_n) - \langle L(\lambda) \rangle} - \frac{F(\lambda_n) - \langle F(\lambda) \rangle}{\sum F(\lambda_n) - \langle F(\lambda) \rangle} \right|$$

Note that in the zero-mean absolute differential area algorithm, if the zero-mean spectral radiances are mirror images of each other, then the area trapped between them will be 2, such that C_{ZMADA} will have a value of -1, indicating exact anti-correlation. Using the derivative of the measured and filter spectral radiances in either the absolute differential area or zero-mean absolute differential area algorithm yields even tighter matching algorithms.

The final class of algorithms investigated and analyzed in the processing code is similar to the absolute differential area but rather than using absolute area, it uses RSS area. That is, the RSS value of each spectral radiance is normalized to unity, and the RSS area trapped between the resulting radiances is computed. The RSS differential area algorithm is given formally by

UNCLASSIFIED

$$C_{\text{RSSDA}} = 1 - \sqrt{\sum \left(\frac{L(\lambda_s)}{\sqrt{\sum L(\lambda_s)^2}} - \frac{F(\lambda_s)}{\sqrt{\sum F(\lambda_s)^2}} \right)^2}$$

and the zero-mean RSS differential area algorithm, of course, is given by

$$C_{\text{ZMRSSDA}} = 1 - \sqrt{\sum \left(\frac{L(\lambda_s) - \langle L(\lambda) \rangle}{\sqrt{\sum (L(\lambda_s) - \langle L(\lambda) \rangle)^2}} - \frac{F(\lambda_s) - \langle F(\lambda) \rangle}{\sqrt{\sum (F(\lambda_s) - \langle F(\lambda) \rangle)^2}} \right)^2}$$

Using the derivative of spectral radiance in either of these algorithms creates yet tighter filtering algorithms.

In the infrared, the shape of the individual material spectral radiance curves is dominated by the shape of the Planck blackbody function, which reduces the efficacy of the spectral matched filter algorithms described above. One way to overcome this difficulty is to normalize the material spectral radiance curves to the Planck function for an estimated surface temperature. For this case, the individual spectral radiance values are divided by the Planck blackbody radiance at each wavelength,

$$\epsilon_e(\lambda) = L(\lambda)/N(\lambda, T)$$

providing an estimate of the "effective" emissivity of each material. These emissivities are not the actual surface emissivity because background/atmospheric radiance effects and actual surface temperatures have not been taken into account. However, the "effective" spectral emissivities provide a much better estimate of actual material spectral variations, and are used in place of the radiance values in the spectral filtering algorithms.

These are but a few of the algorithms which SOC's MIDIS will perform at the same rate at which image data is collected. Substantial computational power is needed to perform such processing. In fact, to spectro-radiometrically calibrated each pixel in a set of 256 x 256 pixel images 20 spectral points deep at each pixel, generated at 30Hz frame rate requires 78 million calculations per second. To calibrate the data and then evaluate six integrals of the form given by $SE(p)$ above requires over 500 million calculations per second. To match filter using the algorithm given by $MF_3(p)$ above simultaneously for two filter functions and to perform response curve integration on three channels requires over 1.3 billion calculations per second. Compare this processing rate, albeit fixed-point, to a Cray 1S CFT capable of performing 23 million floating-point calculations per second and the magnitude of the challenge is evident. Electronics designed specifically to perform this task by using pipelined and paralleled processing will yield the required processing speed. In fact, SOC's visible-band instrument currently can perform 500 million calculations per second, and will be upgraded to include matched filtering capability. This tremendous processing capability occupies a volume of less than 300 in³, without any ASICs design. Basic architecture of the processing electronics is shown in Figure 1-24.

Following is a more detailed description of the electronics. Data input conversion from analog to digital and output conversion back to analog is done to 12 bits resolution. All internal processing is done to 16 bits resolution.

UNCLASSIFIED

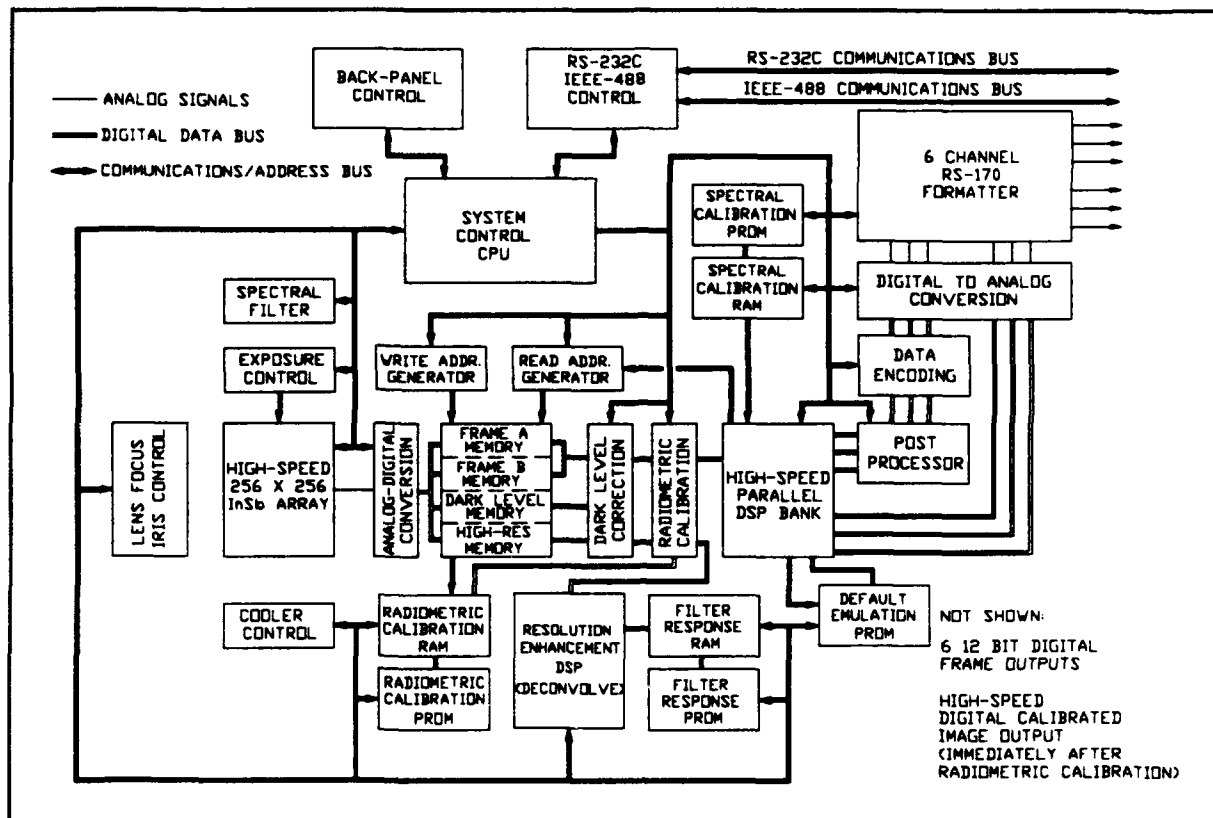


Figure 1-24. MIDIS Processing Electronics Block Diagram.

1.5.1 Data Collection and Storage

Few aspects of MIDIS are unchallenging; conversion of the analog output from the detector is not one of them. Leaving the detector at an effective 40MHz rate, each pixel must be digitized to 12 bits and directed to one of three memory banks capable of storing 50 complete images each. SOC has already developed a 12 bit Analog to Digital converter capable of digitization rates of up to 40MHz. Adaptation of this board to the MIDIS instrument will be straight forward. Two memories are required to allow the instrument to operate in real-time. As one memory is being filled with a new cube of spectral and spatial data, the previously filled second memory is readout and its data processed. When filling of the first memory and processing of the second memory are complete, the memory banks switch roles, with data in the first memory now processed, while the second memory starts collecting new data. This ping-pong use of two memory banks allows uninterrupted operation. The third bank of memory mentioned above and shown in Figure 1-24 holds the dark level data used to compensate for system offsets. Total memory area is about 10Meg x 12 bits, or 15Mbytes.

UNCLASSIFIED

1.5.2 Calibration

In order to convert the raw data from the array to meaningful spectro-radiometric data, a two point calibration will be performed. First, dark level offset will be subtracted from the data, with each pixel in each spectral frame having its own unique dark level value recorded periodically. Two high-speed multipliers will multiply the raw data by calibration factors based on integration time, aperture, and frame-rate with calibration data stored in EPROM. Gain correction is a two step process. First, a spectrally independent spatial uniformity correction factor brings all pixels of the array to the same effective response. Next a spectrally dependent calibration factor converts uniformity corrected raw data to meaningful radiometric values. Effects of varying integration times are included in this calibration. Do not infer, however, that data at this point can be read directly as a spectral radiance, since internal precision is only 16 bits, whereas the dynamic range of the spectral imager is 10^9 , or 30 bits. Having the data in a radiometric form means that all relative spatial and spectral values are correct so that further processing can be properly performed, and actual radiance values read by multiplying any pixel's value by a scale factor encoded onto the data stream. For cases where a non-zero spectral dispersion exists across the array, dispersion will be accounted for when applying the calibration factor. Spectral calibration takes place in the lab by correlating filter encoder counts to known wavelengths produced by a precision spectrometer. Stability of the filter ensures calibration remains accurate.

Absolute calibration takes place at the time of assembly by viewing sources of known spectral radiances under all spectrometer operating conditions. For SOC's visual RTISR, this means at 4 zoom positions, 2 iris positions, and 3 intensifier gain settings. For the proposed MIDIS instrument, this means only 2 aperture positions, plus any zoom positions if zoom is included in the objective lens. Calibration is effected by noting the output of a given pixel viewing a given wavelength and noting the integration time necessary to generate this level. Calibration factors are then generated for each wavelength, after accounting for the spatial correction factor, which have the form:

$$K(\lambda) = \frac{L(\lambda) \Delta t(\lambda)}{C(\lambda) - C_0(\lambda)}$$

where $C(\lambda)$ is the raw A/D counts, $C_0(\lambda)$ is the dark level offset, and Δt is the integration time. By then multiplying dark level corrected raw data taken at a later time by this factor $K(\lambda)$ and dividing by Δt , true radiance is generated. Actually, when the instrument is operating, the true integration time is not used in the calibration. Only the relative exposure-to-exposure magnitude of the integration time is included. This is because exposure time can vary by a factor of about 100,000 over the operating range of the instrument. Absolute integration time is part of what makes up the scale word encoded onto the data stream.

Immediately after MIDIS measures the laboratory calibration source, the instrument will measure its internal source. Define the values produced by measuring the internal source at the time of calibration as $I_c(\lambda, p)$. If the instrument then measures a different internal reference level of $I_c'(\lambda, p)$ at some later time during operation, then calibration can be maintained by scaling the original calibration factors by the ratio of $I_c(\lambda, p)/I_c'(\lambda, p)$. Dark level compensation is implicitly understood to be done at any measurement. Note that the internal reference need not produce a source of known spectral radiance; it need only produce a source of stable spectral radiance.

UNCLASSIFIED

1.5.3 Processing

A great deal of emphasis has been placed on the fact that collection and calibration of spectral images is only the beginning of the battle. Consider the rate at which spectro-radiometric data is collected and calibrated: With the array running at a 600Hz exposure rate, and comprising 256 x 256 pixels, data leaves the array at about 40MHz rate. To allow this flood of data to be processed into a more manageable form containing usable information about the scene, the internal processing electronics will act on the calibrated data to effect integration with any desired spectral response curve, or spectral matched filtering. Since spectral matched filtering requires more hardware to implement than simple sensor emulation, one of the four processing channels will contain filtering/emulation architectures, while the other three will contain just emulation architectures. Basic Architecture of a filtering/emulation block is shown in Figure 1-25.

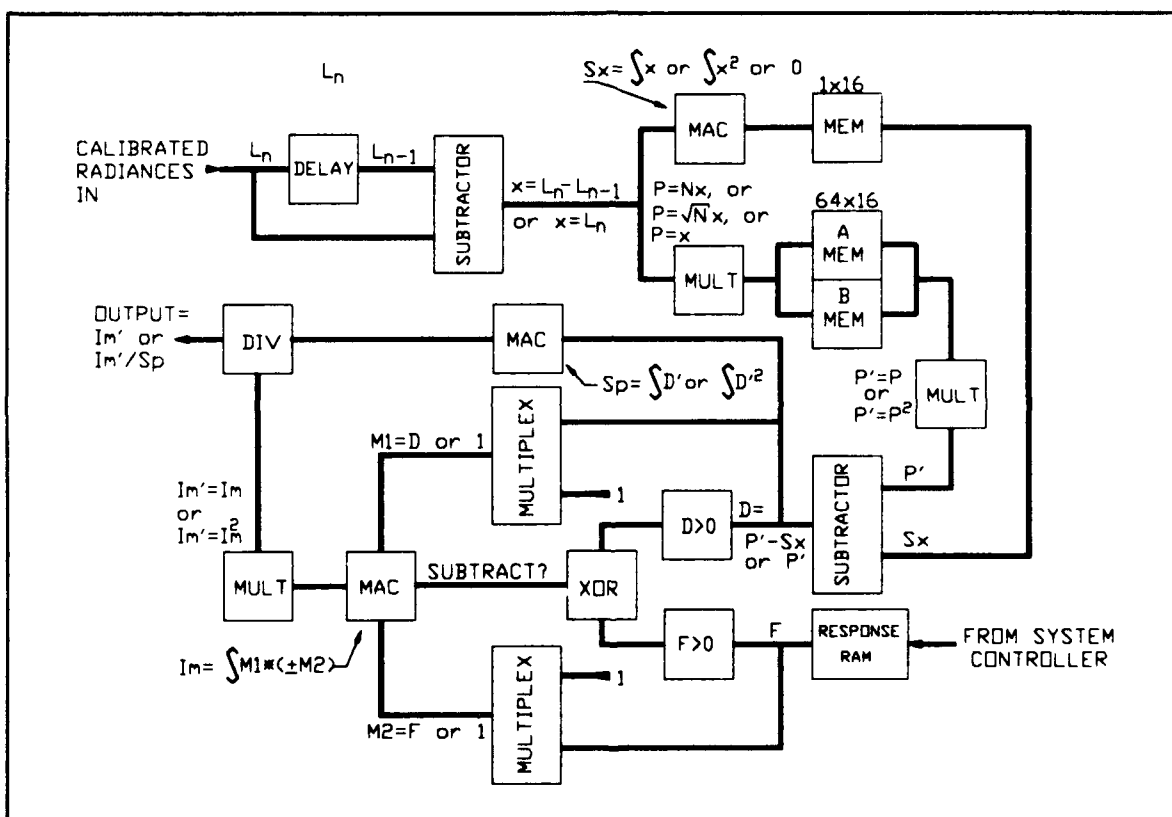


Figure 1-25. Detail of Matched Filtering Channel.

This architecture makes use of high-speed multipliers, multiply-accumulators, and subtractors to allow a large range of filtering and emulation algorithms to be implemented in real-time. Not shown are control signals to control how the architecture implements a given algorithm. Note that this architecture is just an extension of the already proven hardware design used in SOC's RTISR. Since inclusion of ASICs to dramatically reduce

UNCLASSIFIED

UNCLASSIFIED

electronics size is impractical given the funding level of a Phase II SBIR, no ASICs will be designed yet. Xilinx programmable gate arrays, however, will be used wherever possible.

For spectral matched filter processing, the matching curve can be generated either by using known material characteristics, i.e., spectral emissivity, of the object being sought, in conjunction with estimated temperature to generate the sought after object's spectral radiance; Alternately, direct measurement where possible will automatically generate this function which can then be used to find similar objects, or to reject other objects of dissimilar material characteristics which might appear similar when viewed broad band. Beyond its use in non-destructive inspection, such capability also has tremendous spin-off potential for threat sensing by allowing discrimination of threat from decoy or background based on material characteristics. Technology transfer applications also include, as mentioned previously, drug interdiction, medical diagnostics, mineralogical mapping, and agricultural monitoring among others.

1.5.4 Control and Data Interfaces

Control of instrument is through either a standard RS-232C serial port, or through an IEEE-488 parallel port. All instrument functions such as frame rate, integration times, processing options, focus and iris can be controlled through these ports with simple commands. The instrument will also be capable of fully autonomous operation, setting operating parameters to achieve the best signal to noise ratio for any given viewing condition. All data within the instrument can be accessed via these busses. For instance, if the spectra for a given set of pixels is desired, the appropriate command is issued to the instrument and the data is returned over the interface bus. A keypad control and simple display will also be included for operation without a computer.

Main output data busses consist of an RS-170 RGB analog video bus and accompanying 12 bit digital counterparts, and a high-speed 16 bit spectral image output bus. Video busses allow viewing and collection of processed data by standard video displays or frame grabbers. Encoded onto the video signal is both a scale word and a grey scale. The grey scale allows for correction of any gain or offset errors, or nonlinearities introduced during transmission or recording of the video signal. Using this greyscale in conjunction with a binary encoded scale word also on the video signal allows absolute radiometric interpretation of the data, even if data has been degraded by long-term storage on video tape. If collection of individual spectral images is desired, then data can be recorded through a high-speed digital port which outputs the data immediately after spectro-radiometric calibration at a 40MHz rate.

UNCLASSIFIED

2.0 POTENTIAL FOLLOW-ON APPLICATIONS

2.1 Introduction

In addition to the basic tasks in Phase I, a comprehensive effort was made to identify specific follow-on and technology-transfer applications for the proposed radiometer. In order to minimize the probability that any given promising application would not be overlooked, two distinct approaches were undertaken. A literature search revealed specific applications for which broad-band spectral imagers are currently used, thus suggesting areas for which the incorporation of additional spectral features might offer improvement over current capabilities. The results of this study were discussed in Section 1.0 in which the detection of rust and corrosion, and quality control of composite materials and electronic circuit boards were discussed in detail, and initial laboratory measurements described. Recognizing that a "bottom-up" approach such as a literature search would reveal old applications which may be improved upon, but would not necessarily reveal new applications not yet reported, a second study was conducted, which was essentially a "top-down" approach. The methodology employed for this approach is illustrated in Figure 2-1.

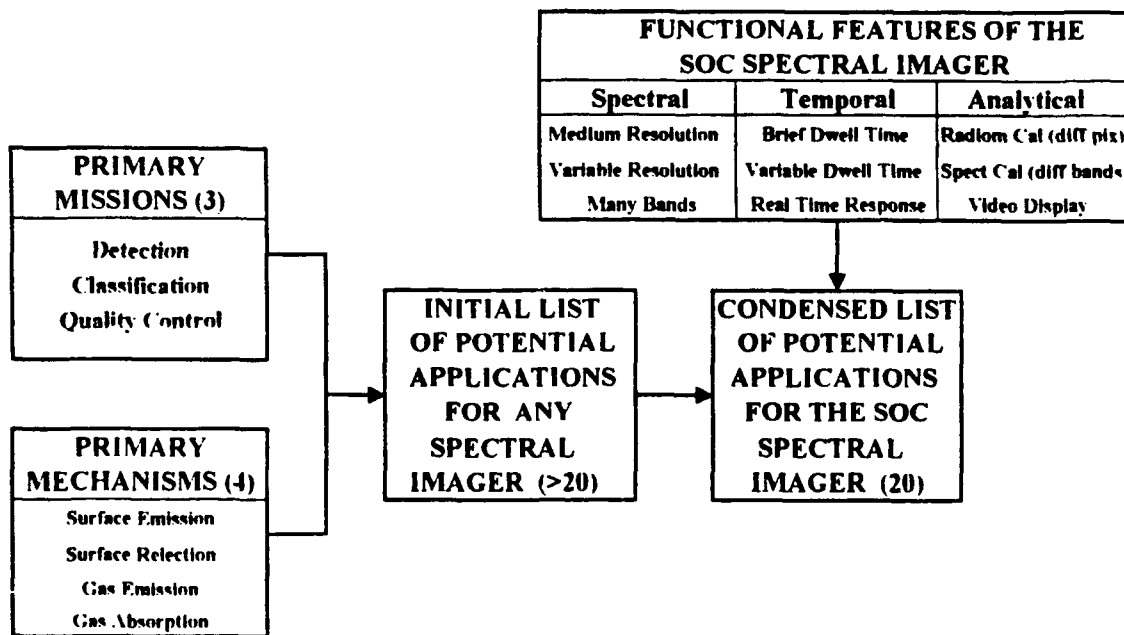


Figure 2-1. Methodology for Application Survey.

The primary missions and mechanisms were combined with the functional features of the spectral imager as the template to conduct a systematic search for applications. A matrix was created and cells examined for high potential applications. After the matrix had

UNCLASSIFIED

been filled with as many entries as could be conceived, a sorting procedure was developed to discard the less attractive applications and retain the more promising ones. This was accomplished by first defining those unique functional features offered by the proposed spectral imager. Nine features emerged, three of which were spectral in nature, three of which were temporal, and three of which were analytical. The resultant matrix is illustrated in Figure 2-2.

Each potential application generated within the matrix was then examined, one by one, to determine whether there was a relatively good match between the nine features that the spectral imager provides and those requirements inherent to the particular application. There was no single application which required all six of the unique features offered by the proposed instrument. On the other hand, because the selection process was conducted judiciously, there were no applications for which there were not at least two direct matches between mission requirements and sensor features. Those applications which would be served by at least four of the nine sensor features were chosen for further investigation.

This matrix was then presented to a wide variety of commercial and Government personnel to solicit input into determining applicable application areas. In the remainder of this section, a short discussion will be dedicated to some of the application areas as presented to industry. In addition to the technical discussion, efforts to generate Government Agency interest will also be discussed.

2.2 Potential Commercial or Private Sector Applications

SOC is pursuing commercial applications with two parallel paths. First, SOC has formed a strategic alliance with Titan Corporation to form an Optical Sensors Consortium. In addition, SOC is also pursuing application areas independently as illustrated in Table 2-1. The following sections discuss the Consortium and, by way of example, two of the promising commercial areas that SOC is pursuing.

UNCLASSIFIED

PRIMARY MISSION	OBJECT or ENTITY OBSERVED or DERIVED	PRIMARY MECHANISM	SPECT DOMAIN	SPECTRAL				TEMPORAL		OTHER	
				Mod Resol	Var Resol	Many Bands	Brief Dwell	Var Dwell	Rapid Anal	Absol Cal	Video Displ
Detection	Rust & Corrosion	Surface Reflect	S, M	X		X	X	X		X	XX
	Illegal Crops	Surface Reflect	S, M	X		X	XX	X	X	X	X
	Buried Objects	Surface Emit	M, L			X	XX	X	X	X	X
	Camouflaged Objects	Surf Refl & Emit	S, M, L	X		X	XX	X	XX	X	X
	Tracer Paint	Surf Refl & Emit	S, M	XX		X	XX	X	XX	X	XX
Classification	Missile Plumes	Hot Gas Emit	S, M	X		X	X	X	X	X	X
	Low Observ Airborne Threats	Gas Absorp	S, M	XX		X	XX	X	X	X	X
	Volatile Solvents	Gas Absorp	M, L	X		XX	X	X	X	X	X
	Poison Gas	Gas Absorp	M, L	XX		X	XX	X	X	X	X
	Surface Material	Surf Refl & Emit	S, M, L	X		XX	X	X	X	X	X
Quality Control	Strategic Missile Payload	Surf Refl & Emit	S, M, L	X		X	XX	X	X	X	X
	Earth Resources	Surf Refl & Emit	S, M, L	XX		X	XX	X	XX	X	X
	Missile Characteristics	Hot Gas Emit	S, M	X		X	XX	X	X	X	X
	Clouds & Snow	Gas Absorp	S, M	X		XX	X	X	X	X	X
	Automobile Exhaust	Gas Absorp	M	X		XX	X		XX	X	X
	Composite Materials	Surface Refl	S, M, L	X		X			XX	X	X
	Electronic Components	Surface Refl	S, M, L	X		X			XX	X	X
	Fabrics & Coverings	Surface Refl	S, M	X		XX	X	X	XX	X	X
	Misc Assembled Products	Surface Refl	S, M	X		XX	X	X	XX	X	X
	Edible Produce	Surface Refl	S, M	X		X			XX	X	X

Studied in Detail

S: NUV-NIR

M: MWIR

L: LWIR

XX: Required

X: Desired

Figure 2-2. Spectral Imager Applications.

UNCLASSIFIED

UNCLASSIFIED

Table 2-1
Potential Commercial Applications

BUSINESS NAME	APPLICATION
Loma-Linda University Medical Center	Non-invasive medical diagnostics
University of Oklahoma Health Sciences Center	Monitoring atmospheric pollution
GDE Systems	Mine Detection
Teledyne Brown Engineering	Missile Interception
Martin Marietta ADTO	Agricultural monitoring
Lockheed Missiles and Space	Missile Interception
Mission Research Corporation	Covert surveillance
Neutronics (automobile pollution control devices)	Automobile pollution monitoring
CI Systems (manufacturer of imaging spectrometers)	Has sought business relationship for marketing our imaging spectroradiometers
SETS Technology(manufacturer of imaging spectrometers)	Approached SOC at International Symposium on Spectral Sensing Research about establishing business relationship

2.2.1 The Optical Sensor Consortium

SOC has teamed with Titan Corporation and E.C. Zipf Associates to form a consortium to commercialize our current line of radiometers as well as the proposed radiometer. Titan Corporation, based in San Diego, is a 1500 employee company with annual sales of ~150M. Their focus is in sensor research and development, sensor manufacturing and integration, and data fusion. E.C. Zipf Associates is a small company in Pittsburgh, Pennsylvania that helps Titan with sensor research and development.

The purpose of this consortium is to allow for SOC to draw on Titan's experience in commercializing sensors and their ability to manufacture sensors. Titan receives an injection of new technology into their sensor research and development as well as another product line. Titan has agreed to commit funds for Phase III of this program.

UNCLASSIFIED

2.2.2

Example Application #1: Ranging and Detection

The detection of objects and their range from an observer has traditionally been of great interest to industry, such as range finders, and to the military for target detection. SOC is independently pursuing this technology to determine its commercial potential. As a start, a concept was presented to GDE System of the Carlyle Group located in San Diego for a novel ranging device to solicit comments.

This concept is based on the fact that an object is always closer to the sensor than is the background. Consequently, the radiation originating from the object must have traversed through less atmosphere than that originating from the background. Targets and backgrounds can thus be differentiated by the relative amounts of atmospheric absorption which has occurred. This is achieved by employing the proposed radiometers capability to resolve spectral images by gating the scene into two windows, one at an absorption band and one located close to the absorption band. By virtue of the bands being close together, the optical properties of the target and background surface will be nearly the same in each band, but the optical properties of their lines-of-sight will be quite different. The ratio of the observed radiances in the two bands will be nearly constant for each background pixel, but will change when a target fills a significant fraction of a pixel.

In order for this dual-band concept to work, spectral resolution is important, as the bands must be close enough to ensure that no significant change in surface reflectivity or emissivity, and must be located just inside and just outside of an atmospheric absorption band. As the line-of-sight will change from one scenario to the next, it is also important that each band be adjustable, so that each band radiance remains within a useful dynamic range. The pixel dwell time must be brief, since the field-of-regard for surveillance systems is usually large. Real-time processing is also essential, as is the case for threat detection systems.

An analysis performed with the Lowtran 6 model indicates that this concept of ranging is feasible. Using the simplifying assumption that solar reflection is much greater than self emission then:

$$I = S \tau_D \rho \tau_U$$

where

I = Observed intensity given spectral band

S = Solar flux in band

ρ = Reflectivity of pixel surface

τ_D = Atmospheric transmission from sun to surface

τ_U = Atmospheric transmission from surface to sensor

then

UNCLASSIFIED

$$\frac{I_{\text{win}}}{I_{\text{abs}}} = \left(\frac{S_{\text{win}}}{S_{\text{abs}}} \right) \left(\frac{\rho_{\text{win}}}{\rho_{\text{abs}}} \right) \left(\frac{\tau_{\text{win}}}{\tau_{\text{abs}}} \right)_D \left(\frac{\tau_{\text{win}}}{\tau_{\text{abs}}} \right)_U - \left(\frac{\tau_{\text{win}}}{\tau_{\text{abs}}} \right)_{\text{TWO WAY}} > 1$$

This yields the following plot as shown in Figure 2-3. Note that the accurate determination of range is possible down to 1.5 kilometers without knowing the atmospheric conditions and can extend below that limit if some measure of aerosol scattering is accounted for (i.e., entering a haze index).

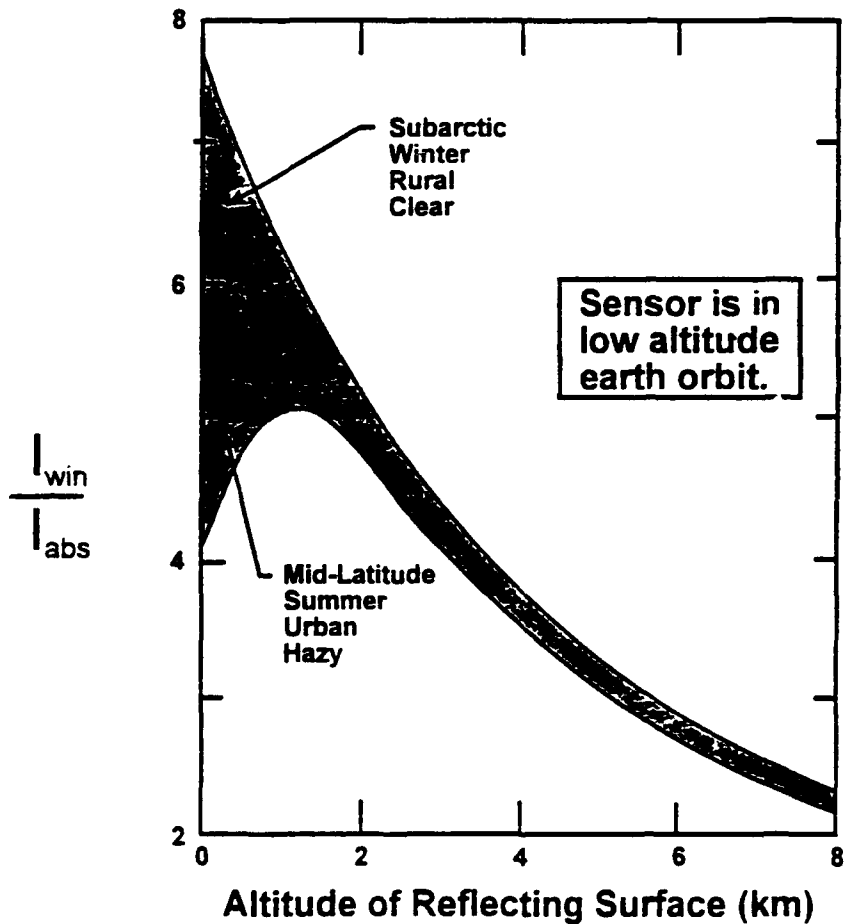


Figure 2-3. Intensity Ratio Versus Distance.

The proposed radiometer is unique for this application in that it ensures that one optimal pair of spectral bands will be available. A carbon dioxide, water or oxygen absorption band can be selected. In addition, the instrument allows for the selection of a contiguous band. The proposed instrument will also have the capability to tune the width and center

UNCLASSIFIED

of each band to realize the maximum degree of contrast. The sensor also yields a real time display.

2.2.3

Example #2: Automobile Exhaust Testing

In this case, SOC is developing an application of the proposed instrument to conduct automobile exhaust testing.

Currently, the procedure used in the United States is time consuming and does not measure two important exhaust pollutants. First, the particulates in the exhaust are not collected and measured. Second, nitric oxide is not measured since it is only produced when the engine is under load. Remote testing systems have been proposed that utilize an infrared beam spanning the road and a single spot measurement is taken before and after the vehicle passes. There are some drawbacks to this method in that it is susceptible to interference by water lines in the spectra and the measurements are questionable because of pollution from previous cars. Figure 2-4 illustrates the interference by water when trying to detect nitric oxide. Note that very fine spectral resolution is required to differentiate the narrow bands.

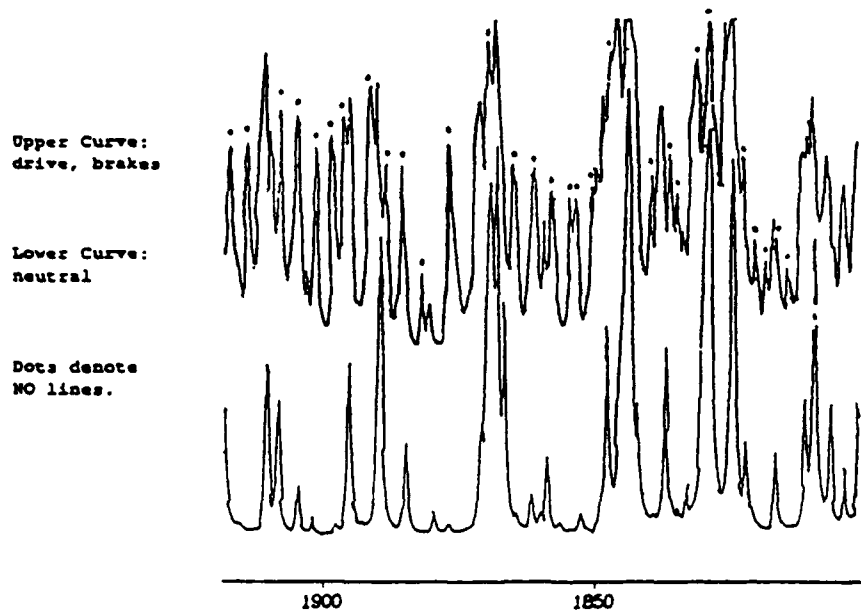


Figure 2-4. Spectral Plot of Nitric Oxide.

In this application, the spectral capabilities of the proposed system would employ a moderate spectral resolution and real time image processing to measure the parameters. This method uses dual "outrigger" bands to extract the amount of nitric oxide that is in the exhaust. These dual bands, illustrated in Figure 2-5, are selected such that the spectral integral of each band is equivalent to the integral across the water band.

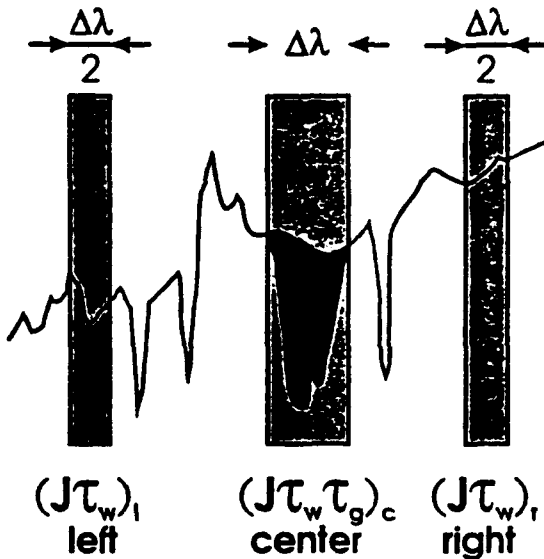
UNCLASSIFIED

Figure 2-5. Application of Outrigger Bands.

These bands are selected so that for a blackbody source:

$$(J \tau_w)_L + (J \tau_w)_R = (J \tau_w)_C$$

where

J = Radiance

τ_w = Transmittance of the water

τ_c = Transmittance of the gas

then

$$\tau_c = \frac{\int J \tau_w \tau_c d\lambda}{\int J \tau_w d\lambda}$$

Note that now the contribution to the water spectral band from the nitric oxide is explicit. There are several advantages to this method. It allows for rapid extraction of the nitric oxide content. The vehicle wake is being sensed by not just one infrared beam but by 256x256 (the array size) beams. This allows for a significant reduction of noise in the signal. Furthermore, this method has the ability to place part of the sensing image in front of the exhaust pipe to generate a "null" or reference area to compare with the exhaust. This would eliminate the effects of other vehicles. In addition, this method averages over the exhaust which integrates turbulence effects.

UNCLASSIFIED

2.3

Potential Uses by the Federal Government

In an effort to discern potential uses of the proposed technology by the Federal Government, SOC contacted a number of agencies within the Government. These agencies were briefed on the current state of the technology (i.e., our visible band radiometer) as well as the proposed instrument, the infrared radiometer. These agencies were then requested to provide ideas for application areas for the proposed instrument. This section will summarize the contact meetings as well as the potential application areas.

The contact meetings were conducted in several ways: individual briefings, symposiums, and group meetings with multi-agency personnel. Tables 2-2 and 2-3 show the organizations that were exposed to the proposed technology during the Phase I program.

Table 2-2

List of Government Organizations Briefed on the Proposed Technology

U.S. Army CECOM (Night Vision Labs - Ft. Belvoir, VA)
U.S. Army TACOM (Tank Automotive Command - Warren, MI)
U.S. Army ARDEC (Picatinny Arsenal - Dover, New Jersey)
U.S. Army Research Lab (White Sands Missile Range - White Sands, NM)
U.S. Army Electronic Sensors Division (Night Vision Labs - Ft. Belvoir, VA)
U.S. Army Corps of Engineers (Topographic Engineering Center - Ft. Belvoir, VA)
U.S. Army Space and Strategic Defense Command (Arlington, VA)
U.S. Army Corps of Engineers (Cold Regions R&D Lab - Hanover NH))
Drug Enforcement Agency (Lorton, VA)
U.S. Army Space Command (Colorado Springs, CO)
U.S. Army Combined Arms Center
U.S. Army TRADOC

UNCLASSIFIED

Table 2-3
**List of Government Agencies Briefed at Symposia
on the Proposed Technology**

U.S. Army CAC	USA Tobyhanna Eng Ctr	NAVSPACECOM
U.S. Army TRADOC	USA AVNC	USA FAS
USASC&FG	USA EC	USA IS
USAIC&FH	USA SOC	USA ADSCH
USACASCOM	USA INS COM	USA SPO
USAARMC	10th Mtn Div	LAM Task Force
USA CECOM	29th Eng Bn	U.S. Army Digitization Office
USA FORSCOM	104th MI Bn	Defense Mapping Agency
USA Ordnance Ctr & School	Naval Air Warfare Center	Phillips Laboratory, Space and Missiles Directorate

After the meetings, the personnel were asked to summarize the application areas for the proposed technology. Table 2-4 summarizes the application areas identified by the Government personnel.

Table 2-4
Application Areas Identified by Government Personnel

ORGANIZATION	APPLICATION AREAS
CECOM	Camouflage design and detection
TACOM	Target detection, background characterization
Army Research Lab	Validation of atmospheric modelling techniques.
Electronic Sensors Division	Mine detection.
Army Corps of Engineers	Topography and mineral identification
Space and Strategic Defense Command	Remote sensing
Drug Enforcement Agency	Detection of illegal crops
U.S. Army Space Command	Remote sensing

UNCLASSIFIED

SOC believes that during the Phase I program significant third party interest has been generated. The next step is to follow up with these organizations. A contact plan is being developed at SOC to individually talk to the organizations. The purpose of these discussions will be to expand upon the respective application area. SOC will collect the requirements from the organizations and determine the commonality from organization to organization as well as the applicability to the proposed instrument.

APPENDIX A

APPENDIX A

**NON-DESTRUCTIVE INSPECTION
BY INFRARED
IMAGING SPECTROSCOPY**

PROGRESS REPORT #1

APPENDIX A

APPENDIX A

APPENDIX A

SOC-R875-001-0494

**NON-DESTRUCTIVE INSPECTION
BY INFRARED
IMAGING SPECTROSCOPY**

PROGRESS REPORT #1

Prepared for:

**DEPARTMENT OF THE ARMY
U.S. ARMY ARDEC
Picatinny Arsenal, New Jersey 07806-5000**

Prepared under:

CONTRACT NUMBER DAAA21-94-C-0013

APRIL 1994

TABLE OF CONTENTS

<u>SECTION</u>		<u>PAGE</u>
1.0	INTRODUCTION	1
2.0	NDI APPLICATIONS OF IR IMAGING SPECTROSCOPY (IRIS)	2
2.1	Surface Characterization of Materials	3
2.2	Circuit Board Inspection	4
2.3	Composite Materials Inspection	6
2.4	Non-NDI Applications	7
2.4.1	Sub-Surface Object Detection	10
2.4.2	Environmental Monitoring and Geological Surveying	11
3.0	PLAN FOR LAB DEMONSTRATION OF IRIS TO NDI	11
3.1	Theoretical Development	12
3.2	Computer Simulation of IRIS	13
3.3	Spectral Radiance as a Discriminant	14
3.4	Development of Material Data Base	16
4.0	SPECTRAL IMAGER DESIGN PROGRESS	17
4.1	Spectral Filtering Technique	17
4.1.1	Circular Variable Filter Design Analysis	18
4.1.2	Integration Time Limits for Spectral Scanning	19
4.1.3	Number of Spectral Exposures per Frame	21
4.2	Method of Coverage from NUV to LWIR	23
5.0	ELECTRONICS DESIGN PROGRESS	24
5.1	Data Collection and Storage	24
5.2	Calibration	25
5.3	Processing	26
5.4	Control and Data Interfaces	27
6.0	SUMMARY	28
7.0	REFERENCES	28

TABLE OF APPENDICES

<u>APPENDIX</u>		<u>PAGE</u>
A	JPL Spectral Discriminators Review	A-1
B	Laboratory Measurement Techniques	B-1
C	Measurement Results: Rusty Iron, SOC Sample Number FS6829	C-1
D	Measurement Results: Iron Painted with Dutch Boy Brand #1560 Acrylic Enamel Red Primer, SOC Sample Number FS6830	D-1
E	Measurement Results: Iron Painted with Dutch Boy Brand #1560 Acrylic Enamel Red Primer and Smeared with Machine Oil, SOC Sample Number FS6831	E-1
F	Measurement Results: A, Solder, Cooled in Air (87°F), SOC Sample Number FS6842 ...	F-1
G	Measurement Results: B, Solder, Cooled in LN ₂ (-77°F), SOC Sample Number FS6843	G-1
H	Measurement Results: Computer Chip (top), SOC Sample Number FS6844	H-1
I	Measurement Results: Circuit Board (top), SOC Sample Number FS6845	I-1
J	Measurement Results: Circuit Board (bottom), SOC Sample Number FS6846	J-1
K	Measurement Results: #1, Graphite Epoxy Composite with Silicon Contamination, SOC Sample Number FS6854	K-1
L	Measurement Results: #2, Graphite Epoxy Composite, Clean, SOC Sample Number FS6855	L-1
M	Measurement Results: #3, Graphite Epoxy Composite with Silicon Contamination, SOC Sample Number FS6856	M-1
N	Measurement Results: Graphite Epoxy Composite - Resin Rich with Flourine, SOC Sample Number FS6857	N-1
O	Measurement Results: 1-29, Graphite Epoxy Composite - Control, SOC Sample Number FS6858	O-1

LIST OF FIGURES

<u>FIGURE</u>		<u>PAGE</u>
1	Spectral Directional Reflectance of Rusted Iron (FS6829), Red Painted Iron (FS6830), and Red Painted Iron Contaminated with a Thin Film of Machine Oil (FS6831)	4
2	The Geometric Facet Model of the PCB that will be used in the Simulation	5
3	Spectral Reflectance Measurements of "hot" (FS6842) and "cold" (FS6843) Solder on Copper Substrates	6
4	Comparison of Clean Sample (FS6855) with a Silica Contaminated Sample (FS6854)	8
5	Comparison of a Clean Sample (FS6855) with a Silica Contaminated Sample (FS6856) ..	8
6	Comparison of a Clean Sample (FS6855) with a Resin-Rich, Fluorine Contaminated Sample (FS6857)	9
7	Comparison of a Clean Sample (FS6855) with an Unknown Sample (FS6858)	9
8	A Comparison of the Directional Reflectance of Grass (FS4054), Earth (FS4055), and Concrete (FS4056)	10
9	A Block Diagram of the Infrared Imaging Spectrometer Simulation Process	14
10	Measurement Matrix for the Materials Selected for this Program	16
11	Filter Bandwidth vs. Cone Angle of Illumination	19
12	Effect of Integration Time on Filter Bandwidth	20
13	Number of Spectral Images vs. Frame Rate	21
14	Total Spectral Dispersion Across Array vs. Frame Rate	23
15	Detail of Matched Filtering Channel	26

This page intentionally left blank.

1.0 INTRODUCTION

The goal of this Phase I SBIR program is to demonstrate the feasibility of Non-Destructive Inspection (NDI) using infrared imaging spectroscopy and to develop a design for a prototype NDI imaging spectro-radiometer. The most fundamental form of NDI is simply visual inspection of an object. The human eye and brain combination is the most powerful sensor/image processing system known. It is estimated (Reference 1) that the human eye can physically sample images into at least 100 different levels of brightness and about 50 distinguishable colors. However, due to biologically constrained filters inherent in the human eye/brain, most of that information is "thrown away." Moreover, the human eye spectrally integrates this information over the visible band, which also washes out a wealth of detailed information about the object. Thus, one of the major goals of this program is to capture as much spectral information as possible and make use of that information, through spectral filtering techniques, to provide additional discrimination capability that is not possible from spectrally integrated images.

Also, it is well known that materials reflect and emit energy throughout the entire electromagnetic spectrum, and that radiant energy from an object, outside of the visible spectrum, provides a tremendous amount of information about the characteristics of that object. Broad band IR imagery has been used for years in NDI applications to provide temperature diagnostic information on materials and processes. The science of spectroscopy has been developed since the time of Sir Isaac Newton to provide fundamental information about material characteristics based on the total spectrum of reflected and emitted energy. A second goal of this program is to use spectroscopic techniques in the IR region of the spectrum for material characterization applied to NDI. For example, IR spectroscopy can identify the surface optical properties of a material, which can be used to determine if an object has been properly manufactured and finished, or detect the presence of minute amounts of contaminants on the surface of an object.

For many NDI applications, the ability to monitor and determine the characteristics of an object in real-time is essential. This is required for NDI scenarios which call for the inspection of large numbers of objects, or for assembly line inspection of objects for quality assurance and process control. This is currently possible for broad band imaging systems; however, the ability to spectrally process and display visible through IR images requires a data throughput one to two orders of magnitude larger than for broad band imagers. Also, most visible and IR imagers produce uncalibrated images, whereas a spectroscopic instrument requires calibrated spectral data, thus imposing an additional processing burden. The third goal for this program is to develop a preliminary design for integrated high speed digital processing electronics for spectral calibration and processing of the data.

Finally, the application of IR imaging spectroscopy to NDI requires instrumentation that is compact, portable and rugged. Many NDI applications require in-situ measurements and analysis of the imagery. Removal of samples from their natural setting for laboratory analysis may alter the sample, thus violating the non-destructive aspects of the testing. Assembly line, or field testing of materials are often in environments that are non-ideal, with wide ranges of illumination, temperature, and humidity. Also, the instrument will probably be used for multiple NDI applications, necessitating a compact instrument that can be easily transported and set-up.

The preceding discussion summarizes the goals of this SBIR program. Surface Optics Corporation (SOC) and NASA's Jet Propulsion Laboratory (JPL) are teamed to define the design and operating characteristics of this instrument during Phase I, develop and demonstrate a prototype instrument during Phase II, and bring the instrument to commercial viability during Phase III. JPL has extensive experience in the development and application of

spectroscopic imaging sensors for remote sensing applications, and also has a strong group working on NDI systems. SOC is a nationally recognized optical measurements and analysis laboratory, which is currently expanding its business base to include NDI instrumentation. One current project involves the development of a single band UV imager as a process control monitor for a material manufacturing application. This involved an optics/sensor/processing design that was geared for a specific application: the detection of the presence of, and irregularities in a specific material in the lay-up based on its UV reflectance properties.

Another SOC NDI application is based on an Air Force requirement to test and evaluate new materials and surface treatments that are being implemented in the exhaust ducts of jet aircraft engines. These treatments must be able to withstand the harsh environmental conditions during engine operation and maintain their optical characteristics. The Air Force needed an instrument to measure the infrared surface optical properties of these treatments in-situ, in the engine exhaust duct, avoiding the costly and destructive process of cutting samples for laboratory measurements. The Air Force initiated a Phase I and Phase II SBIR program to design and develop an In-Situ Bidirectional Reflectometer with SOC, based the company's long history of optical property measurements. The challenge of this program was to reduce a laboratory scale instrument to a miniaturized, automated instrument that was easy to insert and operate in the field.

This Phase I progress report will describe the initial work on this program. Section 2 will discuss the initial NDI applications that will be explored, as well as other potential applications for the instrument. Section 3 will describe our plan for demonstrating the system capabilities of IR imaging spectroscopy for NDI. Sections 4 and 5 will review the current status of the instrument design analysis, and Section 6 will summarize the current program status.

2.0 NDI APPLICATIONS OF IR IMAGING SPECTROSCOPY (IRIS)

One of the requirements of this program is to demonstrate the applicability of IRIS to multiple NDI applications. The goal here is to "get our hands dirty" in the sense of identifying "real" NDI opportunities for the instrument by contact and discussions with potential end users of the instrument. This will provide insight into realistic technical and operational requirements for the instrument, develop initial practical applications, and form the basis for a business plan for commercializing the instrument. Toward this end, we have performed literature search of the existing uses of thermal IR imagery in NDI and made contacts with a number of local organizations with NDI interests and applications. After initial review, we have selected three application areas which, with ARDEC concurrence, we will pursue.

2.1

Surface Characterization of Materials

Many NDI applications require the ability to determine the physical characteristics of materials that are applied during the manufacturing process, or the nature of surface wear or surface contamination of previously manufactured objects. Broad-band thermal imagery has been successfully used to provide much valuable information in this regard. Reference 2 describes techniques to post process thermal image data to obtain material properties such as thermal diffusivity, coefficient of thermal expansion, and time resolved thermal signatures to diagnose material delaminations. Reference 3 provides an analysis of the methodology for detecting plastic coating omissions on an aluminum substrate, and Reference 4 describes an implementation of thermal imagery for paint skip detection used in the manufacture of aluminum beverage containers.

All of the broad-band thermal imagery techniques rely on inferring material temperature variations based on measured radiometric differences without any information on the surface emissivity of the object. Indeed, this is the main source of uncertainty in obtaining quantitative information on the surface temperature and emissivity of objects. While much valuable quantitative work on NDI has been done based on relative temperature difference estimates, either spatially or temporally, which can be made with high accuracy using broad-band imagers; there is still a need for instrumentation for quantitative estimates of material surface temperature and emissivity. Reference 5 compares a number of the common algorithms used for non-contact temperature measurements and provides a summary of the advantages and disadvantages associated with these techniques. In general, single-band and two-band techniques have the advantage of being simple and fast, but suffer from low accuracy without detailed knowledge of the surface emissivity. Multi-wavelength techniques have high accuracy and have the potential for emissivity determination (which will be discussed in detail below), with the disadvantage of being computationally slow and complex. The speed of multi-wavelength techniques is an issue that will be addressed in this SBIR program.

For the actual demonstration of infrared imaging spectroscopy to NDI during this Phase I program, it is hoped that the surface characterization application will be directly applicable to the ARDEC mission. That is, during our kick-off meeting at ARDEC a number of interesting application problems were described that would be ideal for demonstrating the capabilities of spectroscopic imaging. The process of identifying the presence of red paint versus rust on the inside of shell casings is one application that is readily performed using spectroscopic techniques. Figure 1 shows a comparison of the spectral directional reflectance, i.e., one minus the emittance, for a rusted iron sample (FS6829), a clean iron sample that was treated with a rust colored red paint (FS6830), and a painted sample that has been contaminated with a thin film of machine oil (FS6831).

The data in Figure 1 clearly shows major spectral differences between the rusted sample and the painted sample in the near- to mid-IR spectral regions, and oil contamination of the paint is easily identified in the 4 to 5 micron band. It will subsequently be demonstrated during this Phase I program that spectroscopic imaging techniques can be used to discern these types of material variations in non-laboratory conditions. Other ARDEC applications that we would like to explore during this Phase I program are the determination of the composition and spectral properties of non-metallic shell casings, and the presence of contaminants on the surface of banded metallic shell casings.

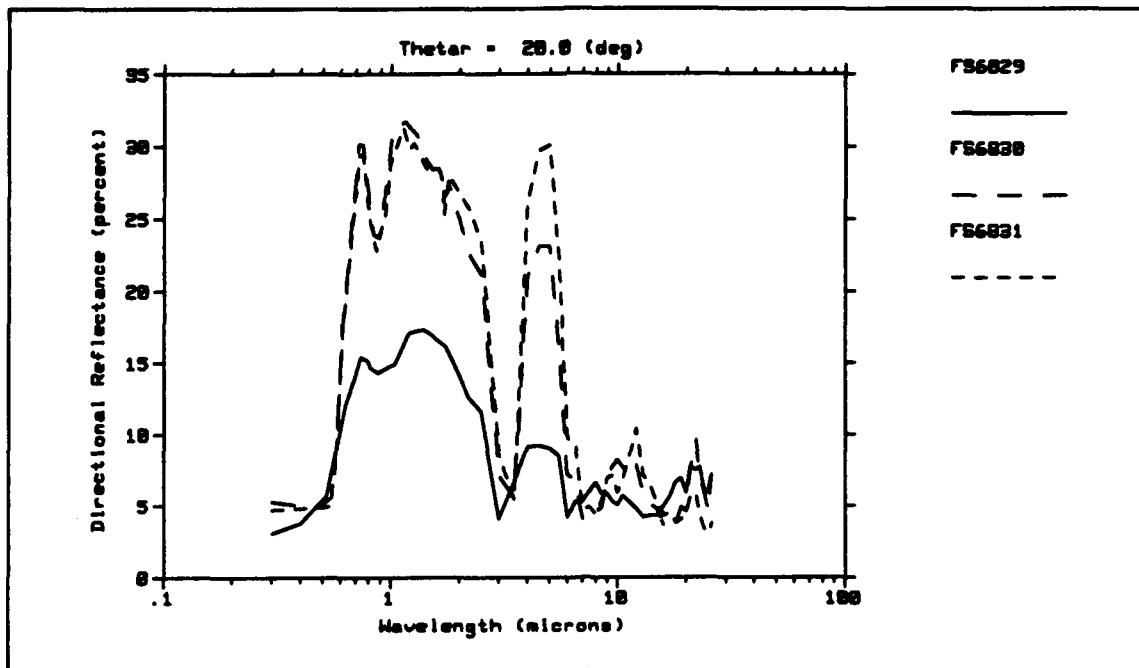


Figure 1. Spectral Directional Reflectance of Rusted Iron (FS6829), Red Painted Iron (FS6830), and Red Painted Iron Contaminated with a Thin Film of Machine Oil (FS6831).

2.2

Circuit Board Inspection

Another likely area for the application of infrared imaging spectroscopy is in the inspection of printed circuit boards (PCB's). We have had meetings with a consultant to IRT Corporation, who has worked on an X-ray systems for PCB inspection. It was noted that X-ray systems, although quite expensive, have only had limited success in the role of quality assurance of PCB's.

A number of thermal IR techniques have been demonstrated for fault location on PCB's. Reference 6 describes the use of thermal imagery for failure analysis of PCB's. Short circuits can be identified by viewing the temperature rise due to solder bridges and faulty connections even, to some degree, on buried conductors in multi-layered boards. The limitations to this technique are related to insufficient temperature sensitivity of the instrument to discern conductor traces hidden under ground planes or reduced current due to high resistance shorts. A British group in Reference 7, coupled finite element thermal analysis with IR imagery and successfully produced heat transfer correlations for a complex package/substrate system. This is similar to the approach that we will pursue. Using the techniques described in Section 3, a detailed thermal and radiative analysis will be performed on a PCB. The spectral signature of the PCB will be used to simulate the sensor performance in viewing the board, and will be correlated with actual spectral IR images. It is anticipated that higher accuracy temperature estimates using multispectral techniques will perform better for powered fault analysis. We will also investigate the time dependent thermal effects on non-powered PCB's using techniques for imposing a thermal pulse on the system and measuring

its time-dependent response. SOC has performed thermal analysis on electronics components in the past and the results have correlated well with measurements. These IR images will also be compared to high resolution visible and X-ray images of the same PCB. Figure 2 shows the wire-frame, facet model of the PCB that will be used in the analysis.

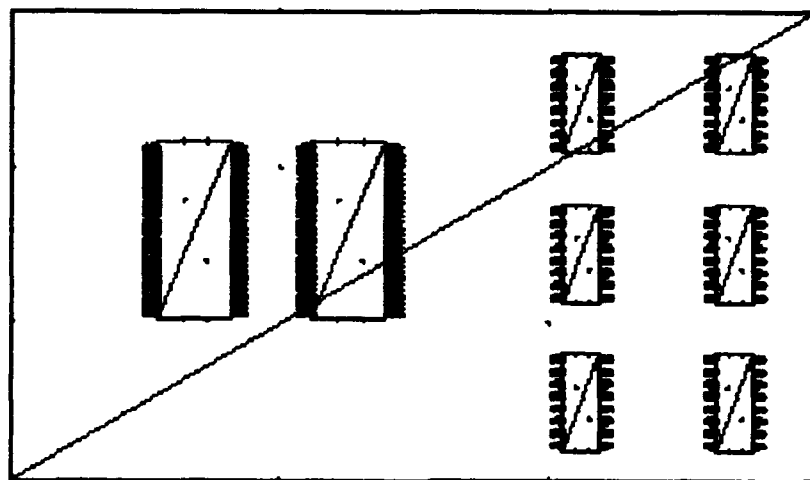


Figure 2. The Geometric Facet Model of the PCB that will be used in the Simulation.

Another important area of application of NDI to electronic components is in the inspection of the quality of solder joints. Visual inspection of solder joints is, at best, tedious and cannot detect the large number of internal defects (e.g., voids, cold solder, de-wetting) that are a major source of concern. While X-ray, ultrasonic and other techniques have been tried, with mixed success, infrared techniques can also play a role here. In particular, laser heating of solder joints correlated with the resultant thermal signatures obtained with broad band thermal imagers has been used to identify internal defects in solder connections. Reference 8 discusses this technique and describes research into increasing the signal-to-noise of these systems.

The ability of infrared imaging spectroscopic techniques to discern faulty solder connections will also be investigated using simulated and measured imagery. Here, the spectral capability of the instrument will be used to assess solder quality, and the thermal analysis will correlate the measurements to specific types of defects. For example, a preliminary experiment was performed on the spectral reflectance of "hot" versus "cold" solder applications. Two copper samples were heated to high temperature and solder was applied, and one sample was immediately immersed in a bath of LN₂ to simulate a "cold" solder joint. The laboratory measurement results are shown in Figure 3.

The results of this preliminary measurement of "good" and "bad" solder connections shows the possibility of spectral discrimination in the 3 to 5 micron region. We will develop samples of other types of defective solder connections and perform similar measurements to assess their spectral variations. The measurements of other PCB materials that will be used in the analysis will be discussed in Section 3.3.

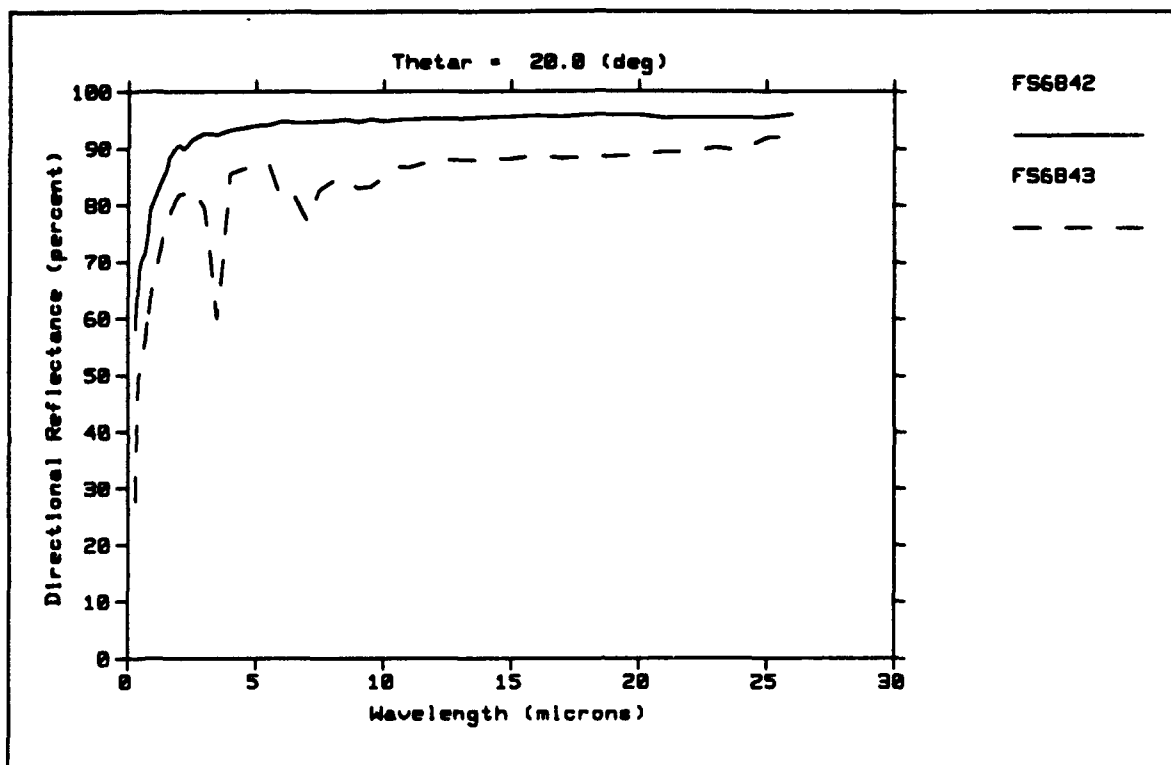


Figure 3. Spectral Reflectance Measurements of "hot" (FS6842) and "cold" (FS6843) Solder on Copper Substrates.

2.3

Composite Materials Inspection

Another application of infrared imaging spectroscopy to NDI which we will consider during this Phase I program is that of identifying structural defects and surface contamination of composite materials. Non-contact, IR techniques for identifying structural defects (e.g. delaminations, voids) in composite materials have received a great deal of attention in recent years. References 9 to 15 describe a number of approaches to NDI using thermographic imaging. All of these methods use an external heat source, in reflection and/or transmission, and make use of 1- or 2-D thermal models to correlate spatial or temporal temperature variations to hidden structural defects. These techniques have also been demonstrated (References 16 and 17) to diagnose sub-surface corrosion in metallic aircraft components.

Here, again, more accurate temperature determination using multi-spectral data will improve the performance of these systems, possibly to the point of reducing or eliminating the need for external heat sources. Also, internal structural defects could be associated with local variations of the polymeric matrix composition, and these variations should be detectable to spectroscopic analysis of the spectral emittance of the material.

Currently, SOC is working with a local company, Composite Optics, Inc. (COI), that produces light weight, parabolic reflectors (microwave and optical) for spacecraft applications. The reflector surfaces are made from a graphite-epoxy composite, and are subsequently coated with a metals and other materials. SOC has performed

vacuum deposition coatings and optical analysis for a number of COI applications. One of the areas of concern is the surface preparation prior to metalization. Many applications require a specific surface roughness on the reflector surface, and COI is exploring a number of surface preparation techniques, including chemical etching. The chemical residue from the etching process, and its effect on the adhesion and quality of the subsequent metalization is a major concern to COI.

COI is in the process of investigating techniques for the identification and characterization of contaminants on graphite-epoxy materials, and is enthusiastic about collaborating with us on our SBIR program. They are particularly interested in the capability to identify and spatially resolve surface contaminants on their reflector surfaces as part of their process control procedure. COI has provided samples of their materials to SOC for laboratory measurements, with the results shown in Figures 4 to 7.

COI identified two samples as contaminated with silica compounds (samples FS6854 and FS6856), a clean sample (FS6855), a fourth sample was identified as resin-rich and contaminated with fluorine (FS6857), and a fifth sample was designated as unknown (FS6858). Examination of the figures suggests that the samples were mislabeled. Figure 6 which shows the comparison of the fluorine contaminated sample looks almost identical to silica contaminated sample in Figure 4. One would suspect that FS6857 is in fact the silica contaminated sample and that FS6856 is contaminated with fluorine. Also, comparing the unknown sample shown in Figure 7 with what we now think is the fluorine contaminated sample in Figure 5 suggests possible fluorine contamination based on the spectral features beyond 12 microns.

Based on the initial measurements of the graphite-epoxy composite materials it is evident that there is a rich spectral content, in the clean and contaminated materials, that can be exploited using an imaging spectroscopic system. With ARDEC's concurrence, we will continue to work with COI to demonstrate the capabilities of infrared imaging spectroscopy to NDI of composite materials.

2.4 Non-NDI Applications

In addition to the NDI applications described above, infrared imaging spectroscopy would be a valuable tool to a number of other disciplines, including sub-surface object detection, environmental monitoring, geological surveying, medical diagnostics, and art inspection. In fact, the technical contact at the Army White Sands Missile Range, who is currently procuring the SOC visible imaging spectral radiometer, expressed great interest in the development of the IR version of the instrument (including requesting a copy of this SBIR proposal), and can be considered as a possible source of additional support for the Phase II development effort. Some of the non-NDI applications of the instrument are discussed below.

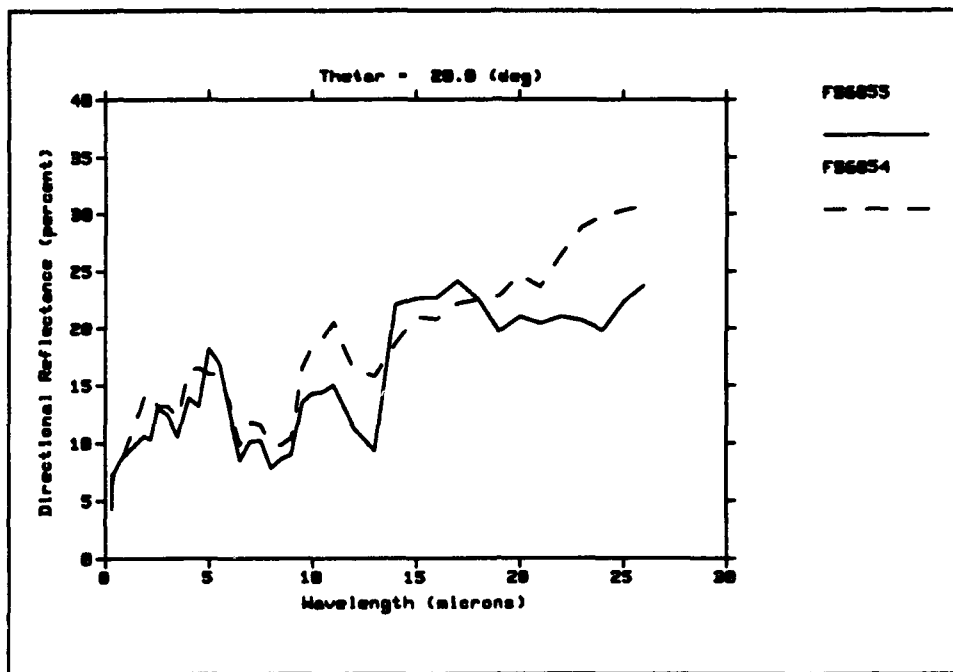


Figure 4. Comparison of Clean Sample (FS6855) with a Silica Contaminated Sample (FS6854).

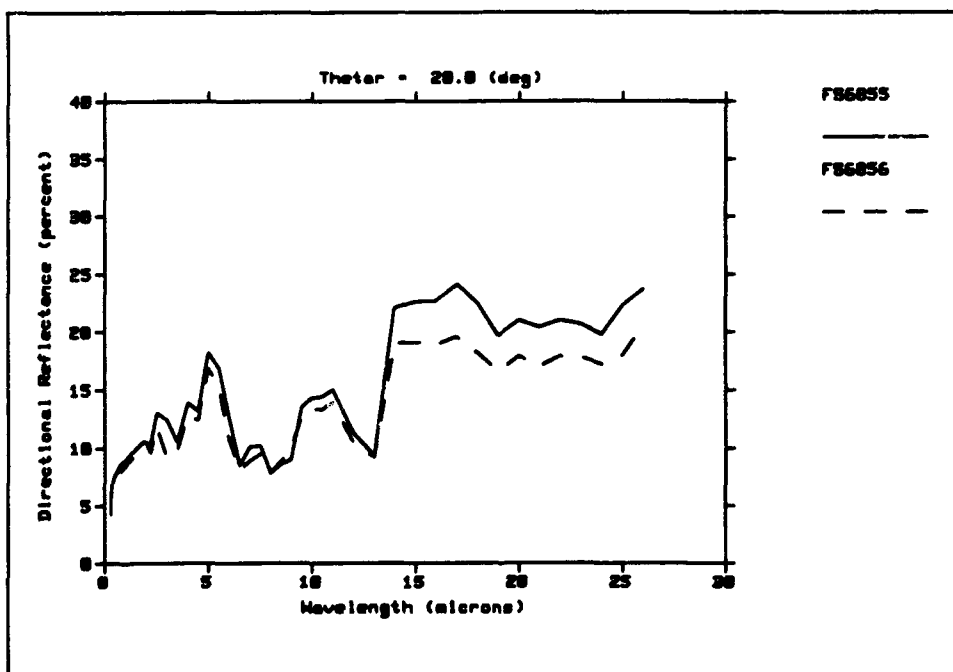


Figure 5. Comparison of a Clean Sample (FS6855) with a Silica Contaminated Sample (FS6856).

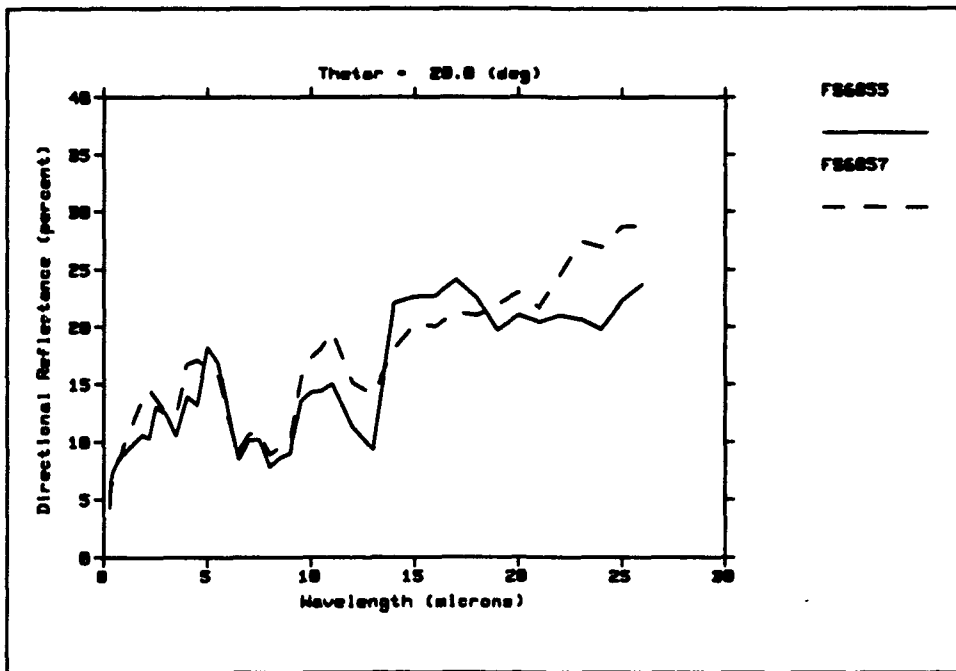


Figure 6. Comparison of a Clean Sample (FS6855) with a Resin-Rich, Fluorine Contaminated Sample (FS6857).

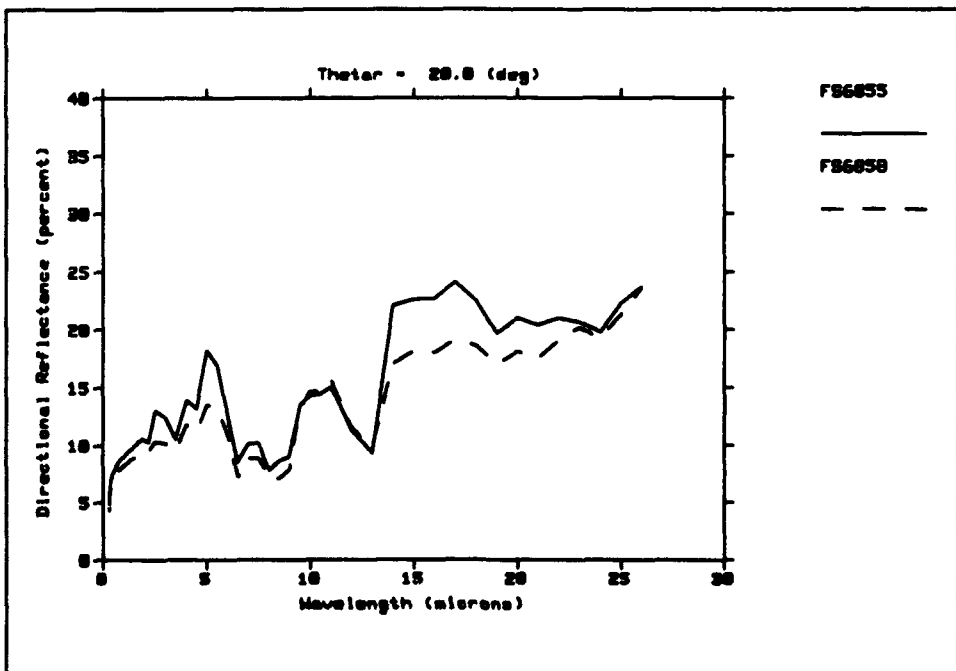


Figure 7. Comparison of a Clean Sample (FS6855) with an Unknown Sample (FS6858).

2.4.1

Sub-Surface Object Detection

The detection of surface or near surface anti-personnel mines in the infrared spectral region is based on detecting spectral radiometric differences between the mine and the disturbed soil surrounding the mine and that of the nearby undisturbed background soil. Previous work at the Lawrence Livermore National Laboratory (Reference 18) has demonstrated the effectiveness of broad band thermal imaging systems for identifying small temperature variations ($\sim 0.2^{\circ}\text{C}$) due to differential conductivity of soils and the emissivity of surface materials. These techniques would have application to, and have been demonstrated for the detection of other sub-surface objects.

Current discrimination algorithms generally use only two colors, typically broad band in the 3 to 5 and 8 to 12 μm region. They also make the assumption that the emissivity of the background and target materials does not vary spectrally (i.e., the "grey body" assumption). SOC has made numerous measurements of the reflectance (i.e., one minus the emittance) of background materials which show that the optical properties are far from "grey." This is shown in Figure 8, which plots the near normal directional reflectance of grass, earth, and concrete as a function of wavelength from 0.3 to 15 μm , and shows significant spectral variation between the 3 to 5 and 8 to 12 μm bands for these materials. This non-grey nature of materials results in limitations in the temperature differences that can be recovered using two color techniques.

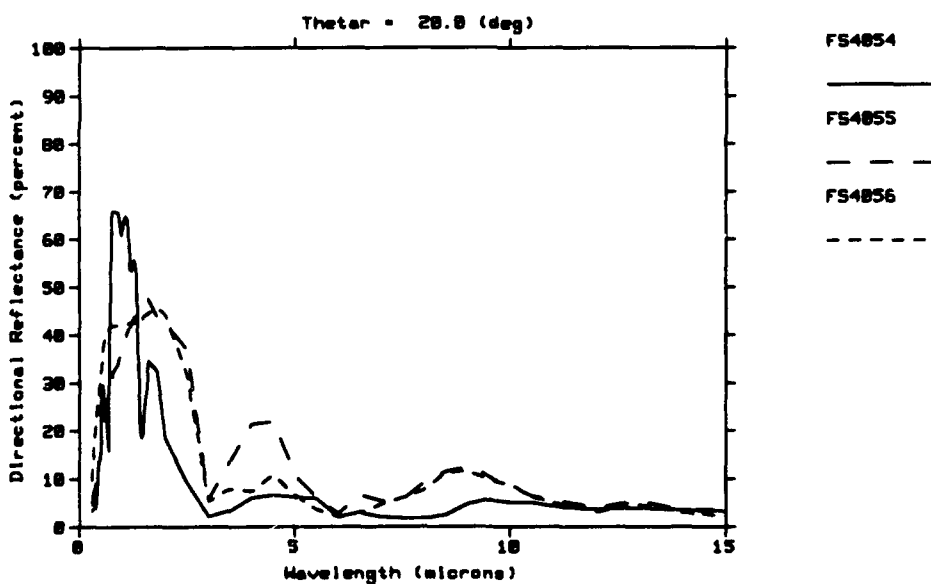


Figure 8. A Comparison of the Directional Reflectance of Grass (FS4054), Earth (FS4055), and Concrete (FS4056).

In addition, the optical and thermal characteristics of soils that have been disturbed by burying the mine will be modified from that of soil in an "undisturbed" state. The optical properties are determined from light multiple scattering in a medium of silica and other inorganic particulates, water, and organic materials. The scattering properties of the mixture are dependent on the optical properties of the components, the size of the particles and

the packing density. When the soils are disturbed, by the act of burying a mine, the composition of the mixture and its packing density is changed, with a resultant change in the optical characteristics of the composite. Similarly, the thermal conductivity and heat capacity of the soil will be changed by altering the composition and density of the soil mixture. Changes in the optical and thermal characteristics of disturbed soils will be readily discernable with a radiometer with high spectral and spatial resolution.

2.4.2 Environmental Monitoring and Geological Surveying

Another application of infrared imaging spectroscopy that is rapidly evolving in the scientific community is for environmental monitoring and geological surveying. This is an area that JPL is heavily involved in, and holds annual geoscience workshops to promote technology development. JPL developed the Airborne Visible and Infrared Imaging Spectrometer (AVIRIS) and NASA annually supports airborne measurement campaigns for international research and development programs. In essence, the geoscience applications for visible and infrared imaging spectrometry that are developed using the AVIRIS data are all potential end-users of the portable radiometer that will be developed under the Phase II effort.

Some examples of the research and development into environmental applications are taken from the JPL Geoscience Workshop publications. Reference 19 describes the results of sensing smoke, clouds, and fire using AVIRIS data. Their analysis shows that water and ice clouds, an important climatological parameter, can be differentiated in the 1.6 to 2.2 micron region; smokes are more readily identified in the near-IR, and surface fires at longer wavelengths. An application of imaging spectroscopy to agricultural monitoring is described in Reference 20. Here biomass estimates of remotely sensed, undeveloped areas were obtained from AVIRIS data using spectral processing of the imagery. Waste management applications using infrared spectral imagery are also possible. Reference 21 describes an application of near-infrared spectroscopy and neural networks to the problem of sorting recycled plastic waste according to the type of polymer resin.

The JPL AVIRIS data has also been exploited for the purpose of geological surveying and mapping. Reference 22 demonstrated the use of AVIRIS data for detecting a number of different mineral deposits at one of the test sites. Reference 23 describes the successful use of AVIRIS data for mapping various mineralogy and lithology features using reference spectra to overcome natural variations in the spectral reflectance.

SOC has obtained data tapes from JPL for a number of AVIRIS scenes. We will work with this data, using IRAD support, to develop algorithms for environmental and geological applications of the Phase II instrumentation.

3.0 PLAN FOR LAB DEMONSTRATION OF IRIS TO NDI

The plan for demonstrating the application of infrared imaging spectrometry to NDI is based on a combination of computer simulations, using laboratory measurements of materials, and laboratory simulation using

broad band IR imagers. The computer analysis will provide a detailed analysis of the performance of the IRIS system, and will enable demonstration of the effectiveness of spectral filtering algorithms for NDI. In addition, a limited laboratory demonstration will be performed with the assistance of the NDI personnel and equipment at JPL. This will entail the use of broad-band, 3 to 5 and 8 to 12 micron, uncalibrated infrared cameras, and discrete spectral filters manually positioned in front of the camera. This will necessarily be a very limited demonstration of the capabilities of IRIS, but will provide some level of verification of the approach. Based on the results of the computer simulations, the NDI application with the largest spectral discriminants will be selected. The details of the lab demonstration will be provided in the second progress report.

3.1 Theoretical Development

The current application of IR imagery for NDI is geared toward broad-band, 3 to 5 and 8 to 12 microns, imagery for thermography. A better approach is to make use of the spectral characteristics of materials with an algorithm that will provide much better spectral resolution and also produce and exploit estimates of the spectral emissivities of the target and background. This approach has been described in Reference 24 using Fourier Transform infrared spectrometer (FTIR) data and a special calibration procedure employing three black body calibration sources. Another technique is described in Reference 25 using a multispectral pyrometer for measuring the surface temperature of ceramics used in advanced propulsion systems.

An algorithm of this type was developed by Spitzberg (Reference 26) to enable the discrimination of decoys from targets for strategic defense applications. The algorithm is based on an equation that represents the actual pixel radiance that is recorded by the radiometer.

$$J(\lambda) = \epsilon(\lambda) \cdot N(\lambda, T) + (1 - \epsilon(\lambda)) \cdot L(\lambda) \quad (1)$$

Here, $\epsilon(\lambda)$ is the spectral emissivity, $N(\lambda, T)$ is the spectral blackbody function, and $L(\lambda)$ is the spectral background radiance. The technique is to write the spectral emissivity in terms of a Legendre expansion,

$$\epsilon(\lambda) = \sum_{k=1}^N a_k \cdot P_k(\lambda) \quad (2)$$

Given a set of ($i=1, \dots, M$) measured spectral pixel radiances, $J_m(\lambda_i)$, solve for the set of N Legendre coefficients, a_k , that minimizes the equation,

$$SSQ = \sum_{i=1}^M (W_m(\lambda_i) - J(\lambda_i))^2 \quad (3)$$

which will yield M spectral estimates of $\varepsilon(\lambda_i)$, and the temperature, T , of the material in the pixel.

This technique has the advantage of not only providing a more accurate estimate of pixel-to-pixel temperature differences, but it also provides spectral emissivity estimates of the material in the pixel. The extension of this approach, based on using measurement estimates of the spectral emissivities of the background and target materials and processing the spectral image data using spectrally matched filters is described in Section 3.3 below.

3.2 Computer Simulation of IRIS

In order to perform accurate simulations of spectral infrared imagery, a detailed thermal analysis of the object in the background is required. This is performed using an ensemble of computer codes for predicting the visual and infrared signature of the object. The code ensemble uses in-house and industry standard codes that have been extensively validated against measurements. Predictions of visual/infrared signatures entails accurate calculations of the radiative environment surrounding the target, including direct and scattered solar illumination as well as environmental thermal emission. The visual signature is computed by accounting for the bi-directional optical characteristics of the treated surface, which determines how the environmental illumination is redirected towards the observer. In the infrared the directional dependence of the thermal emission must also be included.

The modeling procedure uses wire-frame, facet models of the surface geometry of the object and background and a detailed thermal model for predicting surface temperatures. Determining the surface temperature of an object as a function of time is essentially an accounting procedure. An object of known temperature gains or loses heat through various paths and connections to other objects. The heat flow along these paths is determined by temperature differences and by object and path physical characteristics. The temperature of the object at any particular time is determined by summing up the heat gained and lost from time zero, dividing the loss or gain by the thermal mass of the object, and adding the change in temperature to the initial temperature.

The thermal model generates temperatures of the facets for each time step in the simulation. The facet temperatures are then used to generate the spectral facet radiance, using Equation (1). The radiance calculation uses the measured optical properties of the materials to compute the self emitted and reflected radiance components. Spectral atmospheric radiance corrections are applied using LOWTRAN to account for atmospheric absorption and path radiance between the object and background and the sensor.

At this point, the spectral facet radiances are projected onto the sensor image plane, and the sensor (spectral, spatial and electronic) modulation of the image is computed. The spectral modulation accounts for optics transmission and detector sensitivity. The transfer functions of the optics and detector array are used to compute the spatial modulation of the image. The spatial modulation is a convolution of the component transfer functions with the spatial image. This is performed in spatial frequency space using 2D Fourier transforms. Electronic noise in the systems is also modeled as a transfer function and convolved with the image.

After calculation of the spectral and spatial modulation effects, the image is essentially "as viewed" by the sensor. At this point spectral and spatial image processing algorithms are applied in order to highlight features of the object under inspection. For this program, spectral filtering techniques will be simulated in order to identify specific spectral characteristics (e.g., defects in material composition) of the object being inspected. A block diagram of the process is shown in Figure 9.

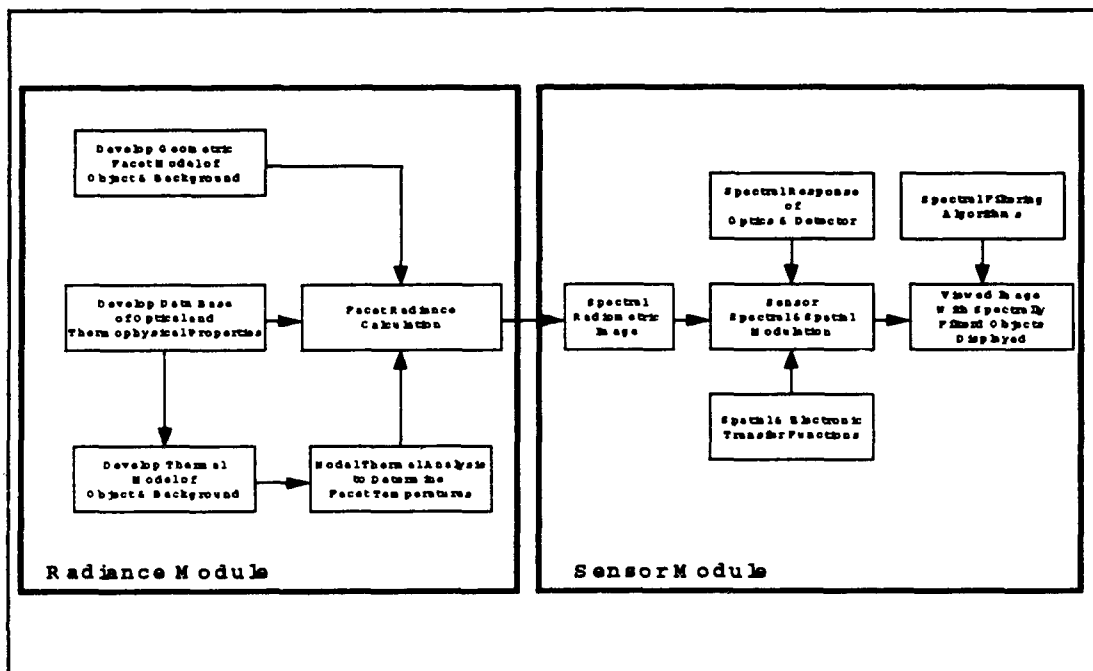


Figure 9. A Block Diagram of the Infrared Imaging Spectrometer Simulation Process.

3.3

Spectral Radiance as a Discriminant

As described above, the infrared spectral radiance of an object is a combination of self-emitted and reflected radiance plus the atmospheric transmission and path radiance between the object and the sensor. When viewing an object with broad-band infrared radiometers, the detected radiance is integrated over the band of the detector,

$$J = \int_{\lambda_1}^{\lambda_2} \{[\epsilon(\lambda) \cdot M(\lambda, T) + (1 - \epsilon(\lambda)) \cdot L(\lambda)] \tau(\lambda) + L_p(\lambda)\} R(\lambda) d\lambda \quad (4)$$

where $\tau(\lambda)$ is the path transmission, $L_p(\lambda)$ is the path radiance, and $R(\lambda)$ is the spectral response of the sensor (optics and detector). Just as two paints with different spectral reflectances can appear to be the same color to the eye depending upon the illumination source (e.g. the sun versus fluorescent lights) because of the spectral integrating

effect of the eye's photoreceptor, so can areas of different spectral emissivity, thermal mass, and thermal conductivity appear to have the same broadband radiance depending upon the thermal conditions of the surrounding environment.

At any point in a scene, a broadband radiometer produces only one parameter to be used as a discriminant - the integrated radiance. A spectroradiometer, on the other hand, produces a large number of parameters to be used as discriminants - the distribution of spectral radiances. Spectral radiance distributions, when processed properly, provide a distinct signature for both the condition and type of material being viewed. As related to the task of identifying surface defects of objects in a viewed scene, this "appropriate processing" means spectral matched filtering. Through this process, a desired relative spectral radiance distribution is used as the matching curve in a specific matching algorithm. Many such algorithms may be used with varying degrees of sensitivity to spectral differences. A simple and relatively loose matching algorithm is given below in Equation 5.

$$D = \frac{\int J(\lambda) C(\lambda) d\lambda}{\sqrt{\int J(\lambda)^2 d\lambda}} \quad (5)$$

Here, $J(\lambda)$ is the measured spectral radiance from the scene, and $C(\lambda)$ is the desired matching spectral radiance. Because the IRIS is internally calibrated, the spectral response of the sensor, $R(\lambda)$, is not a factor here. With the application of this algorithm, objects in the scene whose relative spectral radiance closely matches the desired spectral radiance will appear bright, while other objects will appear dimmer. Application of a threshold value will set all objects whose degree of correlation, D , is less than the threshold to black, thereby displaying only the desired objects. Through simple recombination with the standard image, defective objects will be highlighted in the scene.

Given that defective objects will produce spectral radiances which differ from the non-defective objects, how can the matching function $C(\lambda)$ be generated? Several methods may be employed to generate this function. If the physical properties of the non-defective object are known, simple calculations may be performed to yield its relative spectral radiance in a given environment. This may not always be the best method. In the case of inspecting previously manufactured articles, such as ammunition stockpiles, theoretical knowledge of non-defective articles may not be available. Instead, an alternate approach is more readily implemented to identify defective objects.

First, by viewing an object known to be non-defective, a baseline, or normal, spectral radiance can be measured. Using this baseline radiance as the filter will show any spectral deviations to the baseline as dark areas; reversing contrast will make these areas bright and more readily detected by someone viewing the output of the IRIS. If clutter, such as non-relevant background objects, is also present in the scene, these too will be filtered out of the scene. Filtering against baselines and correlating the processed images generated by these baseline rejects any clutter, leaving only the defective articles in the scene. In most cases, however, such clutter rejection would be unnecessary since the cognitive ability of the operator will be able to discriminate the highlighted defective objects based on shape and location within the image.

3.4

Development of Material Data Base

In order to perform the sensor simulations described above, a detailed data base of material optical and thermal properties is required, and SOC's measurement laboratory is nationally recognized for providing this data. Currently we are developing the data base around the three applications described in Section 2. That is, we have developed a measurement matrix for obtaining optical and thermal properties of PCB components, rusted metal, painted metal, and contaminated painted metal, and a number of clean and contaminated graphite-epoxy materials. The current measurement matrix is shown in Figure 10, and we will be adding to this matrix as the program develops. The measurement instrumentation and data reduction techniques used to obtain the data are described in Appendix B, and the measurement results are presented in Appendices C through O.

ERAS FORMAT BASIC NUMBER	MATERIAL DESCRIPTION	DIRECTIONAL REFLECTANCE	
		$\phi_i = 0^\circ$	$\theta_i = 20^\circ$
		$\lambda = 0.3$ to $2.0 \mu\text{m}$	$\lambda = 2.0$ to $26.0 \mu\text{m}$
FS6829	Rusty Iron	X	X
FS6830	Iron Painted with Dutch Boy Brand #1560 Acrylic Enamel Red Primer	X	X
FS6831	Iron Painted with Dutch Boy Brand #1560 Acrylic Enamel Red Primer and Smeared with Machine Oil	X	X
FS6842	A: Solder, Cooled in Air (87°F)	X	X
FS6843	B: Solder, Cooled in LN_2 (-77° F)	X	X
FS6844	Computer Chip (top)	X	X
FS6845	Circuit Board (top)	X	X
FS6846	Circuit Board (bottom)	X	X
FS6854	#1: Graphite Epoxy Composite with Silicon Contamination	X	X
FS6855	#2: Graphite Epoxy Composite, Clean	X	X
FS6856	#3: Graphite Epoxy Composite with Silicon Contamination	X	X
FS6857	Graphite Epoxy Composite - Resin Rich with Flourine	X	X
FS6858	1-29: Graphite Epoxy Composite - Control	X	X

Figure 10. Measurement Matrix for the Materials Selected for this Program.

4.0 SPECTRAL IMAGER DESIGN PROGRESS

Preliminary design of the imaging spectrometer portion of the instrument is progressing well with two major design issues already addressed. Both the method of spectral filtering and the implementation of coverage from near-ultraviolet (NUV) to long-wave infrared (LWIR) have been studied and a design approach decided on.

4.1 Spectral Filtering Technique

SOC developed its spectral imaging capability two years ago based on CVF technology; other technologies for spectral filtering are available, and might have become better developed in the two years since initial development. Section 2.2 of SOC's proposal stated that a major goal of this Phase I SBIR effort would be to re-evaluate various methods of spectral imaging from NUV to LWIR and decide on the optimum implementation of spectral imaging. "Optimum", of course, must be used carefully, since many factors must be weighed in the decision. One spectral filtering method, for instance, might give significantly better spectral resolution than another, but cost correspondingly more or cover a smaller spectral range. The factors, then, that were considered in evaluating various filtering technologies included spectral resolution, ability to be used in an imaging format, speed of scanning, polarization effects, band of coverage, optical speed (F-number effects), temporal and temperature stability, cost, reliability, and ease of use. Included in Appendix A is a summary of various filtering techniques generated by JPL. Following is a brief description of the more promising spectral filtering techniques with their associated advantages and disadvantages.

One of the most recently introduced spectral filters is the acoustooptic tunable filter (AOTF). AOTFs rely on the photoelastic effect, in which mechanical strain introduces a first-order (linear) change in the refractive index of a material. Reference 27 provides a very good discussion of the physics involved in the photoelastic effect. If a vibrating transducer is connected to a material displaying the photoelastic effect, then an index diffraction grating can be produced in the material, with the "ruling" of the grating (peaks in refractive index per millimeter) being defined by the frequency of vibration and sound propagation velocity in the material. When light encounters this material, it will undergo Bragg diffraction from the index grating and simultaneously be shifted in frequency by an amount equal to the transducer's excitation frequency. AOTFs exploit the first phenomenon. If a multichromatic beam encounters a transducer-driven photoelastic material, then each component wavelength in the beam will be diffracted at a different angle defined by both the wavelength and the frequency of the transducer. A slit, or other optical technique, can then select only a single wavelength for viewing. The real elegance of an AOTF lies in the fact that the wavelength being viewed can be changed merely by changing the frequency at which the material is vibrating, thereby changing the ruling of the resultant index grating.

AOTFs offer very good spectral resolution, tune quickly, and have no (macroscopically) moving parts. Due to the birefringent nature of the photoelastic effect, however, AOTFs split the incident light into orthogonal polarizations, requiring two sensors to maintain instrument polarization insensitivity. This effect is exactly what is needed if an imaging spectro-polarimeter is being designed, but this is not SOCs goal; our goal is to build a polarization insensitive instrument. AOTF technology is also currently limited in spectral coverage, but current R&D,

with which JPL is familiar, could ultimately lead to AOTFs operating in any band at extremely low cost. Currently, however, due to the high cost, limited spectral coverage, and polarization effects of AOTFs, AOTFs are not deemed the optimum choice for IRIS.

Another interesting technique for spectral filtering is FTIR (Fourier-Transform InfraRed) spectroscopy. Although FTIR is an acronym for an infrared technique, it is used generically to refer to any spectral band of coverage. FTIR uses interference to determine the spectral distribution of a beam. By introducing light into a Michelson (or similar) interferometer and moving one mirror in the interferometer, a time varying signal is generated at the detector. Fourier transformation of this signal to frequency space yields the spectral content of the beam. This technique can be used in an imaging format to provide excellent spectral resolution. The major drawbacks of FTIR imaging spectrometry, however, are size, vibrational and temperature sensitivity, and the massive processing which must be performed on the time varying signals to retrieve the spectral information.

Liquid-crystal tunable filters (LCTFs) were also considered as a candidate filtering technology, but cannot currently operate beyond the visible band. LCTFs also suffer from very poor peak transmission and maintain good bandwidth only when illuminated with low cone angle (high F-number) beams. LCTF technology, then, is currently unacceptable for IRIS development.

Although SOC has previous experience in using CVFs in spectral imaging schemes, this experience was not intended to be the overriding factor when evaluating spectral imaging techniques. Having reviewed alternate techniques, however, CVFs still appear to be best suited to IRIS development. More detailed discussion of CVF operation will be provided below, but the major factors contributing to the decision to proceed with CVF technology are ease of use, good spectral resolution, band coverage from NUV through LWIR, filter stability over both time and temperature, and low cost.

4.1.1 Circular Variable Filter Design Analysis

To the end of producing as flexible and marketable instrument as possible, SOC has decided to allow for coverage from NUV to LWIR, with the means of covering that broad range discussed in Section 4.2. Three separate filters will be necessary to provide coverage from 400 nm to greater than 12 μ m. For the NUV-NIR band, two semicircular filters will cover the range from 380 nm to 700 nm, and 700 nm to 1200 nm at about 2% bandwidth; For the MWIR band, the filter segments will cover the range from 1.25 μ m to 2.5 μ m, and 2.5 μ m to 5 μ m at about 1.5% bandwidth; the LWIR segment will cover 8 μ m to 14 μ m at about 1.5% bandwidth, with two such segments used back-to-back. Similar filters are available as standard technology from OCLI. Position of the filters will be encoded to 4,095 points per revolution, ensuring accurate determination of exact wavelength being viewed.

As shown in Figure 11, a narrow-band dielectric filter's bandwidth varies with cone angle of incident light. This graph was generated with data from OCLI⁽²⁸⁾ based on a filter's center wavelength shift versus angle of incidence of collimated light. As this figure shows, a 2% filter will see a negligible increase in its bandwidth when used in a fast F/1.8 system (cone angle = $\pm 15.5^\circ$); the narrower filters exhibit very similar performance. Hence, the imaging spectrometer portion of this instrument will have tremendous light gathering capability. The CVF is also temperature stable, exhibiting a center wavelength change of only about 70 ppm/ $^\circ$ C, or only $\pm 0.6\%$ over the military

temperature range of -55°C to 125°C . This is less than a half-bandwidth change, or only 3 nm at 500 nm for extremely harsh environmental conditions. Figure 11 shows the bandwidth change of an all dielectric filter as will be used in the MWIR and LWIR. The NUV-NIR filter is actually an "induced-transmission filter", so called because dielectrics are used to impedance match very thin layers of silver in the coating stack. Cone-angle performance of this filter is slightly worse than an all dielectric filter, but still exhibits only a minimal 10% increase in bandwidth when used in an F/1.8 system.

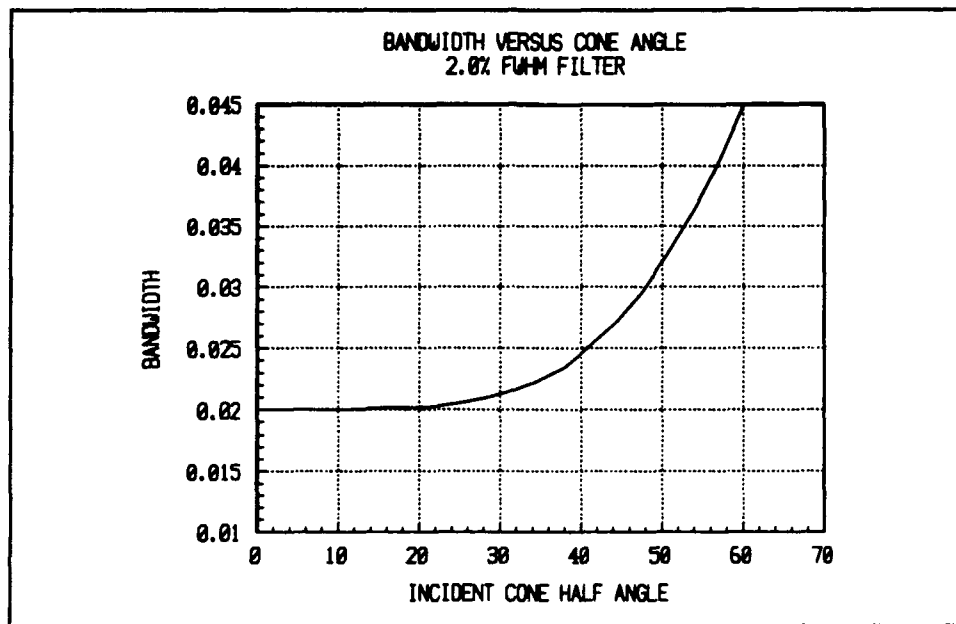


Figure 11. Filter Bandwidth vs. Cone Angle of Illumination.

4.1.2

Integration Time Limits For Spectral Scanning

When the CVF is rotating, integration time on the array must be controlled to effectively freeze the rotation of the filter. If integration time were not properly controlled, then bandwidth spreading would occur as the CVF changed its center wavelength while a pixel was integrating. Assume that a pixel views a wavelength of λ_1 at the start of the integration time. If the CVF rotates at a rate of N revolutions per second, then at the end of an integration period Δt , the same pixel will now view a wavelength of $\lambda_2 = \lambda_1 + (\lambda_{\max} - \lambda_{\min}) \cdot N \cdot \Delta t$, where λ_{\min} and λ_{\max} are respectively the CVF's minimum and maximum wavelengths. The new filter response curve, $F'(\lambda, \lambda_c)$, for this pixel will then be the integral of the nominal filter response, $F(\lambda, \lambda_c)$, over the range of center wavelengths from λ_1 to λ_2 :

$$F(\lambda, \lambda'_c) = \int_{\lambda_1}^{\lambda_2} F(\lambda, \lambda_c) d\lambda_c \quad (6)$$

Effect of this change in filter response function is shown graphically in Figure 12, which plots the increase in filter bandwidth for varying effective slit width normalized to filter bandwidth, i.e., $s = (\lambda_{\max} - \lambda_{\min}) \cdot N \cdot \Delta t / \Delta \lambda$. This plot also shows the change in effective center wavelength which is simply $(\lambda_1 + \lambda_2)/2$.

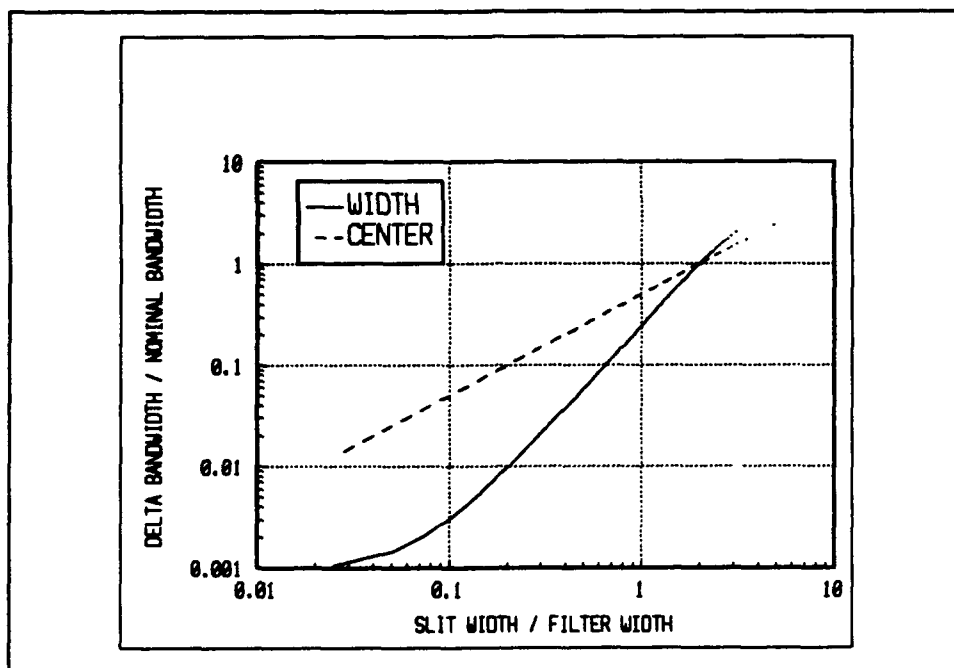


Figure 12. Effect of Integration Time on Filter Bandwidth.

Using a maximum increase in bandwidth of 10%, i.e., from 2% to 2.2%, and the above graph, the filter rotation must not change the center wavelength by any more than 70% of the filter's bandwidth. For a given filter rotation rate N , full-width-at-half-max bandwidth of $\Delta\lambda_{\text{FWHM}}$, and filter minimum and maximum wavelengths of λ_{\min} and λ_{\max} respectively, this bounds the maximum integration time for a given filter rotation rate as $\Delta t_{\max}(N) = .7 \cdot \Delta\lambda_{\text{FWHM}} / ((\lambda_{\max} - \lambda_{\min}) \cdot N)$. For the three filters with a spectral coverage of 300 nm to 1100 nm, 1.25 μm to 5 μm , and 8 μm to 14 μm , and at filter rotation rate of 30 Hz, this equates to a maximum integration time of about 250 μs .

A very important feature of the instrument to note at this point is that bandwidth of the instrument is completely controllable through exposure time. By increasing the exposure time, the filter is allowed to rotate further during an exposure, broadening the bandwidth. The preceding analysis arrived at a maximum allowable exposure time for a given filter rotation rate to prevent broadening of the bandwidth. This feature, however, can easily be exploited to increase bandwidth from the minimum of about 2% of center wavelength all the way to completely panchromatic, i.e., the full spectral range of the filter.

4.1.3

Number of Spectral Exposures per Frame

As detailed next, spectral scanning mode of the instrument can be further broken down into two sub modes. These two modes are distinguished by their differing spectral dispersion across the height of the array (in the SWIR-MWIR and LWIR bands). Note that this discussion, except where noted, applies only to the two longer wavelength imaging systems which do not have gated image intensifiers.

When the instrument collects a set of spectral images for sensor emulation or spectral matched filtering, the total number of images that it can collect in a given frame is dependent on frame rate, the array readout time, and any dead time between readouts. To maximize the number of spectral images which can be collected and then processed by the instrument, the array must be read out continuously. That is, as soon as the 256th row is read out of the array, read out must begin again immediately at the first row. Under this condition, the imager can acquire

M spectral images for a given filter rotation rate N as defined by
$$M = \frac{1}{N \tau_{\text{exp}}}$$
 where τ_{exp} is the image readout

time for a given spectral exposure. For an array with a minimum full image readout time of 1.25 ms (one which appears to be a good choice for the instrument but which is still being investigated), and at a 30 Hz frame rate, each frame can contain 26 spectral images. Maximum number of spectral exposures per frame will increase inversely with overall frame rate, up to a maximum of at least 50 (60 more likely, but this is still being investigated). Number of spectral exposures collected versus frame rate in maximum collection mode is shown in Figure 13. This figure applies to all three bands.

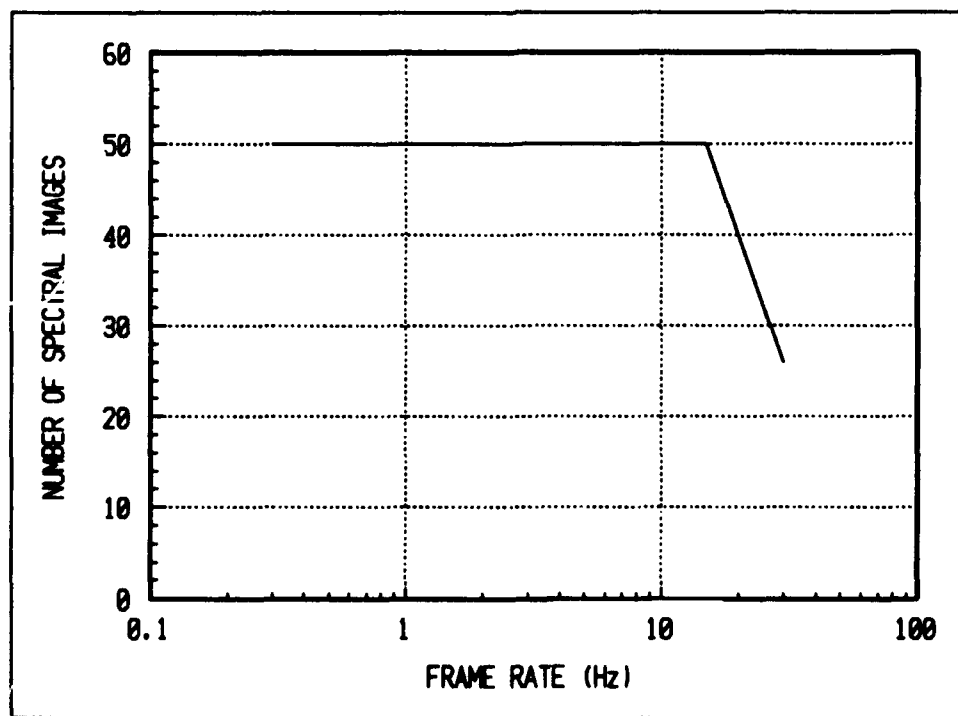


Figure 13. Number of Spectral Images vs. Frame Rate.

Note that the caveat was made above that this curve is for the maximum number of exposures per frame, i.e. each exposure follows its predecessor immediately. At a nominal radius of $1.75''$, the NUV-NIR filter exhibits a lineal spectral dispersion of $900 \text{ nm}/(2\pi \cdot 1.75'')$, or 81 nm per inch , or $3 \text{ nm per millimeter}$ in the NUV-NIR band; equivalent lineal spectral dispersions in the other two bands are 13 nm/mm for the SWIR-MWIR band, and 43 nm/mm in the LWIR band. The arrays each cover an area of about $10 \text{ mm} \times 10 \text{ mm}$. If the array is situated such that its projection onto the CVF places the center row on a radial vector, and is demagnified onto the filter by a factor of 1.5, then a dispersion of $\pm 10 \text{ nm}$ exist across the array in the NUV-NIR band, or only $\pm 1.25\%$ of the passband; equivalent array dispersions in the SWIR-MWIR band and LWIR band are $\pm 43 \text{ nm}$ ($\pm 1.15\%$ of the passband) and $\pm 143 \text{ nm}$ ($\pm 2.4\%$ of the passband) - twice the relative dispersion of the other two bands since total band is covered twice in 360° respectively. What this means is that each pixel views the scene at the resolution of the filter (2%), but at a slightly different wavelength. At $4 \mu\text{m}$ at the center of the array, for instance, pixels in the first row view a wavelength of $4.04 \mu\text{m}$, while pixels in the last row view a wavelength of $3.96 \mu\text{m}$. This dispersion exists with the CVF stationary. If the CVF is rotating during exposure and readout of the array, then the wavelength illuminating any given row will change during the readout. The variable integration time of the SWIR-MWIR and LWIR arrays can be viewed as a window of exposure and readout scanned across the rows of the array. The rate at which this window scans across the array and the rotation of the CVF will operate together to vary the effective dispersion across the array. If the exposure window scans in the same direction as the filter is rotating, then the rates of both can be synchronized so that each row is exposed to the same wavelength as any other row. For a given full-array readout time τ_{exp} , this rotation rate is given explicitly by the following equation:

$$N_{\text{monochrome}} = \frac{\Delta\lambda_{\text{array}}}{\tau_{\text{exp}} (\lambda_{\text{max}} - \lambda_{\text{min}})}$$

where $\Delta\lambda_{\text{array}}$ is the total spectral dispersion across the array with the CVF stationary. Using a minimum readout time of 1.25 ms means that the monochrome frame rate is 17.7 Hz for the SWIR-MWIR band, and 37.7 Hz for the LWIR array. In order to maintain the frame rate at an integer submultiple of the standard 30 Hz video rate, a 15 Hz rate would be used with 50 spectral images per frame. The relationship between spectral dispersion across the rows of the array versus frame rate and maximum number of exposures per frame is shown in Figure 14. Note that this figure plots the total array dispersion relative to the SWIR-MWIR passband, not the plus or minus value.

At any frame rate and number of spectral exposures per frame, dispersion across the array will be constant. Processing electronics will automatically account for this dispersion in applying the correct spectro-radiometric calibration factors and when performing spectral response curve integration and matched filtering.

In summary, when the system is scanning spectrally, it can operate in two different modes: First, it can maximize the number of spectral images per frame based on frame rate. Second, it can minimize spectral dispersion across the array based on desired number of spectral images. For the gated, image-intensified NUV-NIR band, spectral dispersion across the array is constant, but can be driven to zero through appropriate collection of spectral images and application of response curves.

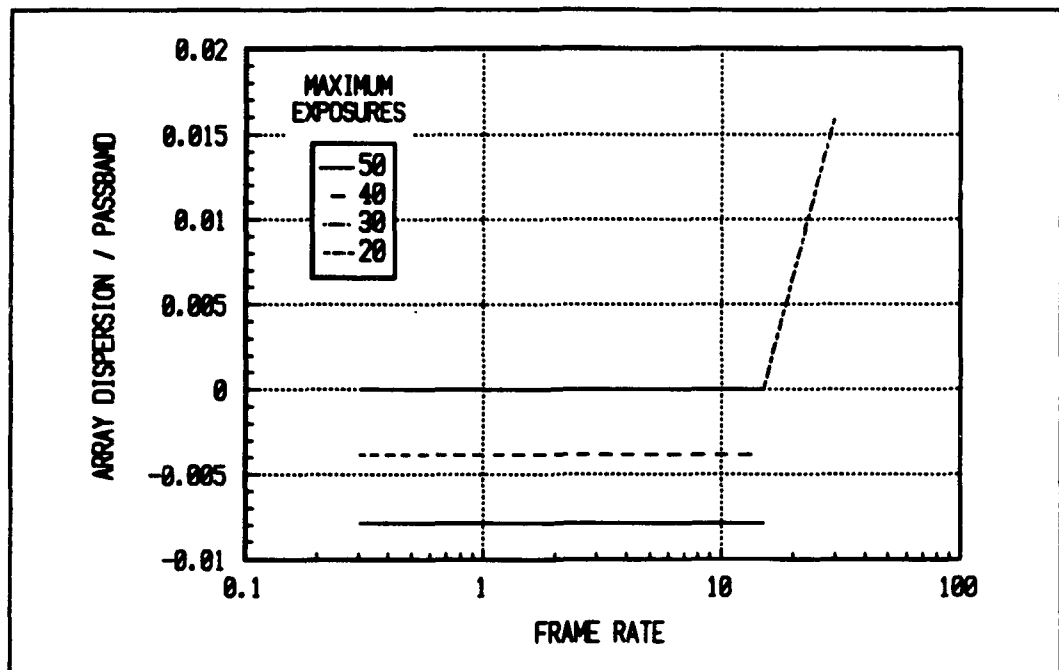


Figure 14. Total Spectral Dispersion Across Array vs. Frame Rate.

4.2

Method of Coverage From NUV to LWIR

SOC's goal in development of this NDI imaging spectroradiometer is to produce an instrument with maximum flexibility to benefit ARDEC and society in general as much as possible. Such an instrument, however, must be very marketable. If SOC were to produce an instrument which could perform any task, from finding flaws in composites to monitoring plant health to aiding in barbecuing steaks to perfection, but which cost millions of dollars, no one would benefit since few, if any, instruments would be built. To maximize benefit to ARDEC, SOC, JPL, and society in general, performance must be traded off against marketability, read as cost. Cost is, in fact, the major factor governing how broad spectral coverage should be accomplished.

In order to cover the broad range from NUV to LWIR, three separate detector/filter systems must be used as explained above. Ideally, these three systems should have the exact same view of the scene, meaning that all share a common fore-optic. However, to design an instrument around an imaging head which contains all three bands would yield a minimally marketable instrument. Such an instrument would be big and very expensive; additionally, most users would probably not need the broad coverage, but instead would be most interested in only one or two of the three bands of coverage. With these thoughts in mind, SOC has opted to design the imaging spectrometer portion of the instrument in three separate heads: a NUV-NIR head, a MWIR head, and a LWIR head. In phase II, ARDEC will have the option of pursuing the development of the bands of most interest (MWIR and LWIR was what the SBIR solicitation indicated, but important information is also available in the NUV-NIR band). Beyond Phase II, customers purchasing an instrument will be able to specify which bands they want to cover. All three

heads can be connected to the processing electronics simultaneously to allow coverage from NUV to LWIR, provided that the heads are properly aligned.

This modular design philosophy is being applied to as many aspects of the instrument design as possible to ensure maximum flexibility and marketability. For instance, many applications may require high-speed imaging, as proposed to ARDEC; many others may not. High-speed imaging comes at a price, so users who do not need speed would be paying (or worse, not paying) for unneeded performance. In the modular design which SOC is pursuing, a low speed version of the instrument could be developed at minimal cost by simply changing the detector read-out board and timing control board.

5.0 ELECTRONICS DESIGN PROGRESS

Modularity is also being adopted in the electronics design. Much of the design work for the electronics was accomplished when the visible-band instrument was developed. SOC is building on this design to increase performance and flexibility. For instance, in the visible-band instrument, a single board controls all operating parameters of the imaging spectrometer, i.e., intensifier gain and gating, CVF speed, lens iris focus and zoom, and array timing signal generation. That means that a change to one function -- choice of detector, for example -- mandates complete redesign of the board at considerable expense. To increase flexibility and to minimize cost, the IRIS instrument will be designed with only one major function on a granddaughter board which then plugs into a daughter card; each daughter card will then control a major function of the instrument such as the previously mentioned imaging spectrometer control, spectral data memory, calibration, processing, or video output memory and post processing. These daughter boards then plug into a mother board which allows data transfer between appropriate daughter boards, sets operational registers and accessible memories on the daughter boards, communicates with the user through a keypad or computer interface and runs the firmware for operating the system.

5.1 Data Collection and Storage

Leaving the detector at an effective 40MHz rate, each pixel must be digitized to 12 bits and directed to one of three memory banks capable of storing 50 (60, more likely) complete images each. SOC has already developed a 12 bit Analog to Digital converter capable of digitization rates of up to 40MHz. Two memories are required to allow the instrument to operate in real-time. As one memory is being filled with a new cube of spectral and spatial data, the previously filled second memory is readout and its data processed. When filling of the first memory and processing of the second memory are complete, the memory banks switch roles, with data in the first memory now processed, while the second memory starts collecting new data. This ping-pong use of two memory banks allows uninterrupted operation. The third bank of memory mentioned above holds the dark level data taken with the detector viewing itself through a narcissus shutter (MWIR and LWIR) or with the intensifier gated off (NUV-NIR).

Total memory area is about 10Meg x 12 bits, or 15Mbytes. SOC's RTISR currently uses high speed SRAM, but conversion to potentially more cost effective DRAM is being studied.

5.2 Calibration

In order to convert the raw data from the array to meaningful spectro-radiometric data, a two point calibration is performed. First, dark level offset is subtracted from the data, with each pixel in each spectral frame having its own unique dark level value recorded periodically. Two high-speed multipliers multiply the raw data by calibration factors based on integration time, aperture, and frame-rate with calibration data stored in EPROM on the motherboard. Gain correction is a two step process. First, a spectrally independent spatial uniformity correction factor brings all pixels of the array to the same effective response. Next a spectrally dependent calibration factor converts spatial-uniformity corrected raw data to meaningful radiometric values. Effects of varying integration times are included in this calibration. Do not infer, however, that data at this point can be read directly as a spectral radiance, since internal precision is only 16 bits, whereas the dynamic range of the spectral imager is as much as 10^9 , or 30 bits. Having the data in a radiometric form means that all relative spatial and spectral values are correct so that further processing can be properly performed, and actual radiance values read by multiplying any pixel's value by a scale factor encoded onto the data stream. For cases where a non-zero spectral dispersion exists across the array, dispersion will be accounted for when applying the calibration factor. Spectral calibration takes place in the lab by correlating filter encoder counts to known wavelengths produced by a precision spectrometer. Stability of the filter ensures calibration remains good without internal molecular absorption references.

Absolute calibration takes place at the time of assembly by viewing sources of known spectral radiances under all spectrometer operating conditions. For SOC's visual RTISR, this means at 4 zoom positions, 2 iris positions, and 3 intensifier gain settings. Calibration is effected by noting the output of a given pixel viewing a given wavelength and noting the integration time necessary to generate this level. Calibration factors are then generated for each wavelength, after accounting for the spatial correction factor, which have the form:

$$K(\lambda) = \frac{L(\lambda) \Delta t(\lambda)}{C(\lambda) - C_0(\lambda)} \quad (7)$$

where $C(\lambda)$ is the raw A/D counts, $C_0(\lambda)$ is the dark level offset, and Δt is the integration time. By then multiplying dark level corrected raw data taken at a later time by this factor $K(\lambda)$ and dividing by Δt , true radiance is generated. Actually, when the instrument is operating, the true integration time is not used in the calibration. Only the relative exposure-to-exposure magnitude of the integration time is included. This is because exposure time can vary by a factor of about 100,000 over the operating range of the instrument. Absolute integration time is part of what makes up the scale word encoded onto the data stream.

Immediately after the IRIS measures the laboratory calibration source, the instrument will measure its internal source. Define the values produced by measuring the internal source at the time of calibration as $I_c(\lambda, p)$. If the instrument then measures a different internal reference level of $I'_c(\lambda, p)$ at some later time during operation, then

calibration can be maintained by scaling the original calibration factors by the ratio of $I_c(\lambda, p)/I'_c(\lambda, p)$. Dark level compensation is implicitly understood to be done at any measurement. Note that the internal reference need not produce a source of known spectral radiance; it need only produce a source of stable spectral radiance.

5.3

Processing

Both in SOC's SBIR proposal and at the kick-off meeting, a great deal of emphasis was placed on the fact that collection and calibration of spectral images is only the beginning of the battle of NDI through spectro-radiometric imaging. Consider the rate at which spectro-radiometric data is collected and calibrated: With the array running at a 600Hz exposure rate, and comprising 256 x 256 pixels, data leaves the array at about 40MHz rate. To allow this flood of data to be processed into a more manageable form containing usable information about the scene, the internal processing electronics will act on the calibrated data to effect integration with any desired spectral response curve, or spectral matched filtering. SOC's current instrument has six processing channels; to reduce cost and complexity in the next generation of instruments, this will likely be reduced to three or four channels, although this is still being studied. Since spectral matched filtering requires more hardware to implement than simple sensor emulation, only one of the channels will contain filtering/emulation architectures, while the others will contain just emulation architectures. Basic Architecture of a filtering/emulation block is shown in Figure 15.

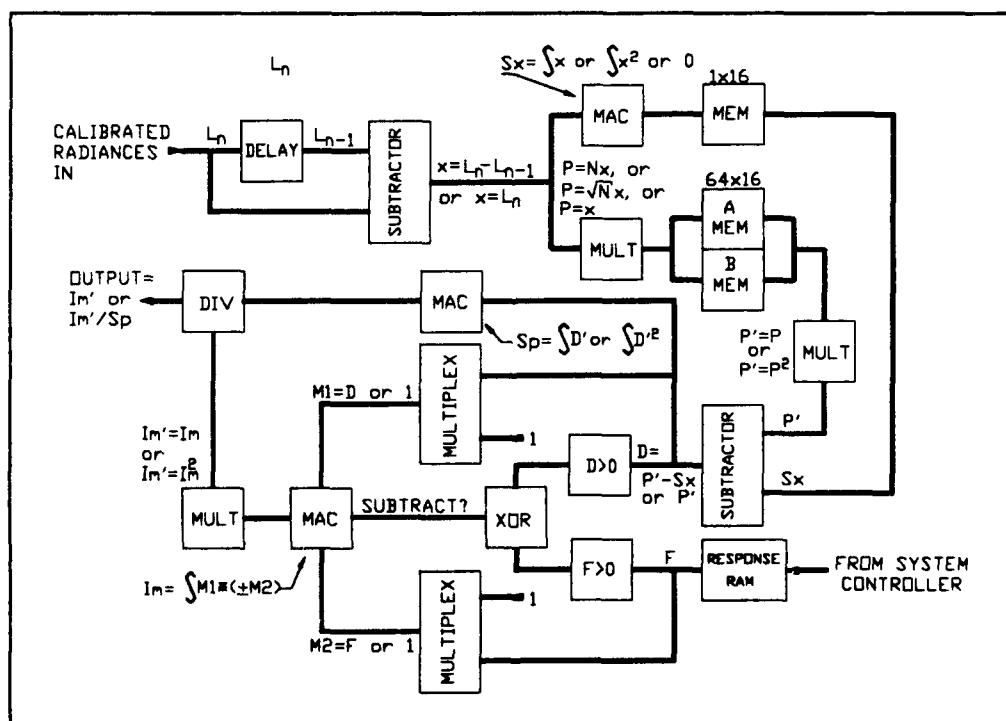


Figure 15. Detail of Matched Filtering Channel.

This architecture makes use of high-speed multipliers, multiply-accumulators, and subtractors to allow a large range of filtering and emulation algorithms to be implemented in real-time. Not shown are control signals to control how the architecture implements a given algorithm. Note that this architecture is just an extension of the already proven hardware design used in SOC's RTISR.

For spectral matched filter processing, the matching curve can be generated either by using known material characteristics, i.e., spectral emissivity/reflectivity, of the object being sought, in conjunction with estimated temperature and irradiance to generate the sought after object's spectral radiance; Alternately, direct measurement where possible will automatically generate this function which can then be used to find similar objects, or to reject other objects of dissimilar material characteristics which might appear similar when viewed broad band. As an example of this technique, consider: the production of burnable shell casings. A sensor viewing the production of casings could record spectral data as casings were produced. Once these casings were determined to be good, this spectral radiance could then be used as a "good" filter. Appropriate collection of data would yield a tolerance range for the spectral radiance of a good casing. Any casing exhibiting a spectral radiance outside of this range could then be identified as bad by the instrument.

A processing function yet to be studied is hardware architecture for performing temperature/emissivity estimation as detailed in Section 3.1. Since the methodology presented in Section 3.1 relies on an iterative process to determine temperature and spectral emissivity, strict hardware implementation might not be the best approach; rather, one or more high-speed digital signal processors (DSPs) running appropriate firmware might be the better approach. Since accurate temperature and spectral emissivity determination has considerable benefit for detection of sub-surface objects, such capability could be important to producing a marketable instrument.

5.4 Control and Data Interfaces

Control of instrument is through either a standard RS-232C serial port, or through an IEEE-488 parallel port. All instrument functions such as frame rate, integration times, processing options, focus and iris can be controlled through these ports with simple commands. The instrument is also capable of fully autonomous operation, setting operating parameters to achieve the best signal to noise ratio for any given viewing condition. All data within the instrument can be accessed via these busses. For instance, if the spectra for a given set of pixels is desired, the appropriate command is issued to the instrument and the data is returned over the interface bus. A keypad control and simple display is also be included for operation without a computer.

For SOC's visible band RTISR, the main output data lines consist of two sets of RS-170 RGB analog video and accompanying 12 bit digital counterparts. For IRIS, these outputs will likely be limited to three or four, but a high-speed, 16-bit digital output will also be included for any one who desires access to calibrated data as it flows through the instrument. Video outputs allow viewing and collection of processed data by standard video displays or frame grabbers. Encoded onto the video signal is both a scale word and a grey scale. The grey scale allows for correction of any gain or offset errors, or nonlinearities introduced during transmission or recording of the video signal. Using this greyscale in conjunction with a binary encoded scale word also on the video signal allows absolute radiometric interpretation of the data, even if data has been degraded by long-term storage on video tape. If

collection of individual spectral images is desired, then data can be recorded through a high-speed digital port which outputs the data immediately after spectro-radiometric calibration at a 40MHz rate.

6.0 SUMMARY

This Phase I SBIR program is to demonstrate the feasibility of infrared imaging spectroscopy to NDI applications, and develop a prototype design. This first progress report has presented a brief literature review of thermal imaging sensors to NDI applications, and has identified three potential NDI applications that will be addressed during this program. The applications are: characterization of the surface properties of materials, printed circuit board inspection, and inspection of graphite-epoxy composite systems for surface contamination.

We have described in this report our simulation procedure for demonstrating the performance of infrared imaging spectroscopy to NDI applications. We have also performed laboratory measurements of sample materials that will be used in the simulation. Initial examination of the data shows promise of exploiting the spectral capabilities of the instrument. The next progress report will present the simulation results and the plan for the laboratory demonstration using broad-band IR cameras.

Preliminary design of the instrument is well underway, with the major goals of revisiting spectral filtering techniques and determining the method of subdivision of NUV-LWIR range already accomplished. More detailed functional design of the imaging spectrometer will now proceed with JPL lending much support. Electronics development is also progressing with the key desire being modularity. With this approach, the instrument should have a very broad range of application.

7.0 REFERENCES

1. Ginsburg, A., Visual Information Processing Based on Spatial Filters Constrained by Biological Data, Ph.D. Thesis, AMRL-TR-78-129, Volumes I & II (1978).
2. Welch, C., Winfree, W., Heath, D., Cramer, E. and Howell, P., "Material Property Measurements with Post Processed Thermal Image Data", SPIE Vol. 1313, 124-133 (1990).
3. Orlove, G. "Development of a Radiometric Model for the Detection of Plastic Coating Omissions on an Aluminum Substrate", SPIE Vol. 1313, 184-189 (1990).
4. Haugh, M., Stone, D., and Thangavelu, M., "Paint Skip Detector", SPIE Vol. 1313, 190-199 (1990).
5. Barani, G. and Tofani, A., "Comparison of some Algorithms used in Infrared Pyrometry: a Computer Simulation", SPIE Vol. 1467, 458-468 (1991).

6. Reizman, F., "Fault Location in Printed Wiring Boards using Thermal Imaging", SPIE Vol. 1313, 172-177 (1990).
7. Hardisty, H. and Shirvani, H., "Thermal Imaging in Electronics and Rotating Machinery", Br. J. NonDestr. Test., Vol. 36, No. 2, 73-78 (1994).
8. Zhnegjun, X., Xuezhong, C. and Xiande, L., "Research on Enhancing Signal and S/N in Laser/IR Inspection of Solder Joints Quality", SPIE Vol. 1467, 410-415 (1991).
9. Laine A., "Detection Failures in Plastic Composites using Thermography", SPIE Vol. 1682, 207-212 (1992).
10. Cowell, S. and Burleigh, D., "Numerical Modeling of Thermographic Nondestructive Testing for Graphite Epoxy Laminates", SPIE Vol. 1313, 143-150 (1990).
11. Burleigh D. and De La Torre, W., "Thermographic Analysis of the Anisotropy in the Thermal Conductivity of Composite Materials", SPIE Vol. 1467, 303-310 (1991).
12. Vavilov, V., Maldague, X., Dufort, B., Robitaille, F., and Picard, J., "Thermal Nondestructive Testing of Carbon Epoxy Composites: Detailed Analysis and data Processing", NDT & E Int., Vol. 26, No. 2, 85-95 (1993).
13. Spicer, J., Kerns, W., Aamodt, L. and Murphy, J., "Time-resolved Infrared Radiometry (TRIR) of Multilayer Organic Coatings using Surface and Subsurface Heating", SPIE Vol. 1467, 311-321 (1991).
14. Troitsky, O., "Pulsed Thermal Nondestructive Testing of Layered Materials", SPIE Vol. 1933, 309-312 (1993).
15. Selman, J and Miller, J., "Evaluation of a Prototype Thermal Wave Imaging System for Nondestructive Evaluation of Composite Aluminum Aerospace Structures", SPIE Vol. 1933, 178-187 (1993).
16. Spicer, J., Kerns, W., Aamodt, L., Osiander, R., and Murphy, J., "Time Resolved Infrared Radiometry (TRIR) using a Focalplane Array for Characterization of Hidden Corrosion", SPIE Vol. 1933, 148-159 (1993).
17. Syed, H. and Cramer, K., "Corrosion Detection in Aircraft Skin", SPIE Vol. 1933, 160-165 (1993).
18. Del Grande, Nancy; "Integration of TEMPS Dual-Band IR with Other Buried Mine Detection Technologies", DARPA 10th Countermine Technology Symposium, 22 January 1992, SPC, Arlington, VA.
19. Gao, B., Kaufman, Y. and Green, R., "Remote Sensing of Smoke, Clouds, and Fire using AVIRIS Data", Summaries of the Fourth Annual JPL Airborne Geoscience Workshop, October 25-29, 1993, JPL Pub. 93-26, Vol. 1, 61-64 (1993).
20. Hart, Q., Ustin, S., Duan, L. and Scheer, G., "Estimating Dry Grass Residues using Landscape Integration Analysis", Summaries of the Fourth Annual JPL Airborne Geoscience Workshop, October 25-29, 1993, JPL Pub. 93-26, Vol. 1, 89-92 (1993).
21. Alam, M., Stanton, S. and Hebner, G., "Near-infrared Spectroscopy and Neural Networks for Resin Identification", Spectroscopy, Vol. 9, No. 2, 30-40 (1994).

22. Hook, S. and Rast, M., "Mineralogic Mapping using Airborne Visible Infrared Imaging Spectrometer (AVIRIS) Shortwave Infrared (SWIR) Data Acquired over Cuprite, Nevada", Proceedings of the Second Airborne Visible/Infrared Imaging Spectrometer (AVIRIS) Workshop June 4, 1990, JPL Pub. 90-54, 199-207 (1990).
23. Clark, R, Swaze, G. and Gallagher, A, "Mapping the Mineralogy and Lithology of Canyonlands, Utah with Imaging Spectrometer Data and the Multiple Spectral Feature Mapping Algorithm", Summaries of the Third Annual JPL Airborne Geoscience Workshop June 1-5, 1992, JPL Pub. 92-14, Vol. 1, 11-13 (1992).
24. Lindermeir, E., Tank, V. and Haschberger, P., "Contactless Measurement of Spectral Emissivity and Temperature of Surfaces with a Fourier Transform Infrared Spectrometer", SPIE Vol. 1682, 354-364 (1992).
25. Ng, D and Williams, W., "Full-spectrum Multiwavelength Pyrometry for Nongray Surfaces", SPIE Vol. 1682, 260-270 (1992).
26. Spitzberg, Richard M.; "Spectrum Analysis Techniques for Non-Grey Targets", Conference on Optical Discrimination Algorithms, 17 October 1991, TBE, Huntsville, AL.
27. Yariv, A., Quantum Electronics, Wiley & Sons (1975).
28. Baker, Martin L. and Ten, Victor L., "Effects of the Variation of Angle of Incidence and Temperature on Infrared Filter Characteristics", Applied Optics, Vol. 6, 1343-1351 (August 1967).

APPENDIX B

APPENDIX B

**NON-DESTRUCTIVE INSPECTION
BY INFRARED
IMAGING SPECTROSCOPY**

PROGRESS REPORT #2

APPENDIX B

APPENDIX B

APPENDIX B

SOC-R875-002-0994

**NON-DESTRUCTIVE INSPECTION
BY INFRARED
IMAGING SPECTROSCOPY**

PROGRESS REPORT #2

Prepared for:

**DEPARTMENT OF THE ARMY
U.S. ARMY ARDEC
Picatinny Arsenal, New Jersey 07806-5000**

Prepared under:

CONTRACT NUMBER DAAA21-94-C-0013

SEPTEMBER 1994

TABLE OF CONTENTS

SECTION	PAGE
1.0 EXECUTIVE SUMMARY	1
2.0 DETAILED DESIGN DISCUSSION	3
2.1 Array Performance Analysis	3
2.1.1 Short-Wave to Mid-Wave IR Detector	4
2.1.1.1 Platinum-Silicide Performance	4
2.1.1.2 Indium-Antimonide Performance	8
2.1.2 Long-Wave Infrared Detector	10
2.1.2.1 Mercury-Cadmium-Telluride	11
2.1.2.2 Extrinsic Silicon	11
2.2 Imager Head Design	12
3.0 ANALYTICAL STUDIES	17
3.1 Description of Computer Codes	17
3.1.1 SPCFLT Computer Code	17
3.1.2 TEMPFIT Computer Code	21
3.2 Results	23
3.3 Conclusions	35
4.0 SPECTRAL-MATCHED FILTERING EXPERIMENTAL DEMONSTRATION	36
4.1 Experimental Setup	36
4.2 Data Processing	38
4.3 Spectral Filtering Demonstration Results	39

LIST OF FIGURES

<u>FIGURE</u>		<u>PAGE</u>
1	Spectral response of PtSi sensor	5
2	Red paint spectral radiance and PtSi NESR	6
3	PtSi spectral imager SNR versus temperature	7
4	Paint spectral radiance and InSb NESR	8
5	Paint spectral radiance and reduced read-out noise InSb NESR	9
6	InSb spectral imager SNR versus temperature	10
7	HgCdTe spectral imager NESR and red paint spectral radiance	11
8	HgCdTe spectral imager SNR versus temperature	12
9	Si:As NESR and red paint spectral radiance	13
10	Si:As spectral imager SNR versus temperature	13
11	CVF-based high speed spectral imager, VNIR version	16
12	CVF-based high speed spectral imager, all waveband version	16
13	Spectral Hemispherical Directional Reflectance (HDR) measurement of red paint, FS6830	25
14	Spectral radiance for red paint sample (diamonds) and Planck function at 295 K	25
15	Fit to spectral emissivity data for red paint at guess temperature 295 K	26
16	Comparison of spectral radiance data for red paint (diamonds), and the radiance using the emissivity curve fit	26
17	Spectral Hemispherical Directional Reflectance (HDR) measurement of low emissivity paint, FS4789	27

LIST OF FIGURES (continued)

<u>FIGURE</u>		<u>PAGE</u>
18	Spectral radiance of low emissivity paint sample (diamonds) and Planck function at 282.5 K	27
19	Fit to spectral emissivity data for low emissivity paint at guess temperature 282.5 K	28
20	Comparison of spectral radiance data for low emissivity paint (diamonds), and the radiance using the emissivity curve fit	28
21	Spectral Hemispherical Directional Reflectance (HDR) measurement of graphite composite sample, FS6854	30
22	Spectral radiance for graphite composite sample (diamonds) and Planck function at 293.1 K	30
23	Fit to spectral emissivity data for graphite composite at guess temperature 293.1 K	31
24	Comparison of spectral radiance data for graphite composite (diamonds), and the radiance using the emissivity curve fit	31
25	Simulated 3 to 5 micron image of panel painted with checker board pattern of four paint samples shown in Figure 26	32
26	Spectral HDR of the materials used in the simulation: grey paint, rust, red paint, oil contaminated red paint	32
27	Simulated 3 to 5 micron image of painted panel that has been spectrally filtered using the normalized spectral radiance for the rust sample	33
28	Spectral HDR of the graphite composite materials used in the simulation: silica contaminated, clean sample, fluorine contaminated, unknown	34
29	Simulated 8 to 12 micron image of graphite composite panel which has to be spectrally filtered to identify the silicon contaminated material	34

LIST OF FIGURES (continued)

<u>FIGURE</u>		<u>PAGE</u>
30	8 μm - 12 μm broad-band image of COI samples	40
31	Relative spectrum of COI samples	41
32	Filtered image using F56854 as filter spectral radiance	42
33	Filtered image using F56855 as filter spectral radiance	42
34	Filtered image using bright areas of F56856 as filter spectral radiance	43
35	Filtered image using F56857 as filter spectral radince	43
36	Filtered image using dark areas of F56856 as filter spectral radiance	44
37	Filtered image using kapton tape as filter spectral radiance	44
38	8 μm - 12 μm broad band image of rust, red paint, and oil-coated red paint	46
39	Relative spectral radiances of rust, paint and oil-coated paint samples	46
40	Filtered image using oil-coated paint as filter spectral radiance	47
41	Filtered image using paint as filter spectral radiance	47
42	Filtered image using rust as filter spectral radiance	48

1.0 EXECUTIVE SUMMARY

SOC and JPL have made substantial progress on the phase I development of the material-identifying infrared imaging spectroradiometer (MIIRIS). Major accomplishments since the last progress report are:

- ▶ The types of arrays to be used in the SWIR/MWIR and LWIR imaging heads have been identified and performance analyzed. The SWIR/MWIR head will use an Indium-Antimonide array, which will be purchased either from Amber or Litton Electron Devices. The LWIR will use either a Mercury-Cadmium-Telluride array from Amber or Hughes-SBRC, or Extrinsic Silicon from Amber or Rockwell. See Section 2.1.
- ▶ Imager head design has been greatly simplified by removing the relay optic between the CVF and detector. Similar to SOC's second version of the visible-band instrument, the detector will lie immediately behind the CVF, increasing performance while reducing cost and complexity. Imager head will be evacuated, a process with which JPL is intimately familiar. The port where the input objective will reside will be sealed with a window, allowing any object lens to be used with the head, thereby allowing tailoring of the lens type and field of view to any given application. All three bands will have nearly identical head configurations, reducing the number of separate parts required to be designed and manufactured. See Section 2.2.
- ▶ Theoretical modeling of spectral-matched filtering, temperature and emissivity determination was performed to provide a capability for implementing and evaluating spectral algorithms for NDI applications. Two computer codes have been developed for spectral filtering (SPCFLT) and temperature and spectral emissivity determination (TEMPFIT) from spectral radiometric images. The theoretical basis for the codes and results of simulations of NDI applications are presented in Section 3.0.

- ▶ SOC has performed a laboratory demonstration of the reality and power of spectral-matched filtering as a tool to identify materials in an image. SOC worked with JPL's test/measurement lab, using an Inframetrics model 760 IR imager in conjunction with spectral filters to collect spectral images of various test samples. A computer program was written to process the collected spectral images and apply various spectral-matched filtering algorithms, many developed by SOC, to the spectral images. Even though the experiment used only 5 spectral filters which were about 7 times broader than the CVFs which will be used in the final instrument, filtering algorithms were able to clearly identify pixels in the image which possessed the same spectral characteristics as the desired spectrum. Given the simplicity and limitations of the experiment, results were nothing short of astounding. See Section 4.0.
- ▶ Progress has been made on the development of a MIIRIS instrument commercialization plan. To this end, SOC is well along the path towards the creation of a strategic alliance with the Titan Corporation. Titan is a \$150 million defense and commercial company headquartered in San Diego, California. Titan has extensive facilities for the development and manufacture of electronic instruments such as the MIIRIS system.

2.0 DETAILED DESIGN DISCUSSION

Since the preparation of the first progress report, substantial progress has been made on the top-level design, conceptual verification, and application development of the material identifying, infrared imaging spectroradiometer (MIIRIS) being developed under this SBIR. Design has been significantly simplified over what was originally anticipated in the original proposal due to work done with JPL. Theoretical modeling of the instrument's ability to identify materials throughout an image based on spectral radiances has been conducted, as has a laboratory demonstration of such capability; results of the laboratory experiment were astoundingly good considering the simplicity of the experiment.

2.1 Array Performance Analysis

Since the most significant difference between the MIIRIS instrument being developed through this SBIR and SOC's current visible-band instrument is the wavelength range of coverage, a great deal of design time has been spent identifying the appropriate imaging arrays to use in the short-wave to mid-wave infrared (SWIR to MWIR) and in the long-wave infrared (LWIR); these two bands cover, respectively, about 1.5 μm to 5.5 μm , and about 5.5 μm to 11 μm or 30 μm , depending on the type of detector used in the LWIR. As detailed in the first progress report, the broad spectral range to be covered by MIIRIS (400 nm to \sim 12 μm) will be divided into three separate imaging heads, one for the visible/near-IR (VIS/NIR), one for the SWIR/MWIR, and one for the LWIR. Such an approach will produce an instrument which will have a broader market than the substantially more expensive approach of covering all three bands in a single imaging head, whether a single fore-optic or multiple fore-optics are used. Some additional time has been devoted to investigating newer detectors to use in the visible-band head of this instrument. Presented below is a detailed discussion of the arrays investigated and identification of the arrays which currently appear to be the best choices for the MIIRIS prototype produced in the Phase II effort.

2.1.1 Short-Wave to Mid-Wave IR Detector

Three different detector material types were considered for the SWIR/MWIR head of the instrument, namely Indium-Antimonide (InSb), MWIR Mercury-Cadmium-Telluride (HgCdTe), and Platinum-Silicide (PtSi). All three types of detectors are commercially available from many manufacturers, including Rockwell (HgCdTe), Litton (InSb), Amber (InSb and HgCdTe), and Loral Fairchild (PtSi). Of these, and as detailed below, the best detector appears to be a 256 x 256 InSb from either Amber or Litton.

2.1.1.1 Platinum-Silicide Performance

Platinum-Silicide is an attractive material to use for manufacturing infrared detectors in that it is easily worked to produce sensors with very good pixel-to-pixel uniformity. Cost for PtSi detectors is also extremely attractive, with a 240 x 256 detector costing about \$5K (in low volume). Unfortunately, Platinum-Silicide's attractive uniformity performance and cost are offset by extremely poor quantum efficiency. Figure 1 shows typical spectral responsivity and quantum efficiency of PtSi. Note that even at its peak, quantum efficiency is a meager 8% at about 1.5 μm , and plunges to a miserable 0.1% at 5 μm .

To understand how this meager quantum efficiency translates to instrument performance, detailed signal and noise calculations must be performed on the detector system. Without re-deriving the equations for detector signal level (in number of electrons) and noise-equivalent spectral radiance (NESR), recall from Sections 3.2 and 3.3 of the phase I proposal that detector signal level is given by

$$N_e(\lambda_c) = \int \frac{L(\lambda) A_j Q_e T_o(\lambda) T_e(\lambda) F(\lambda, \lambda_c) \eta(\lambda) \Delta t}{h \frac{c}{\lambda}} d\lambda$$

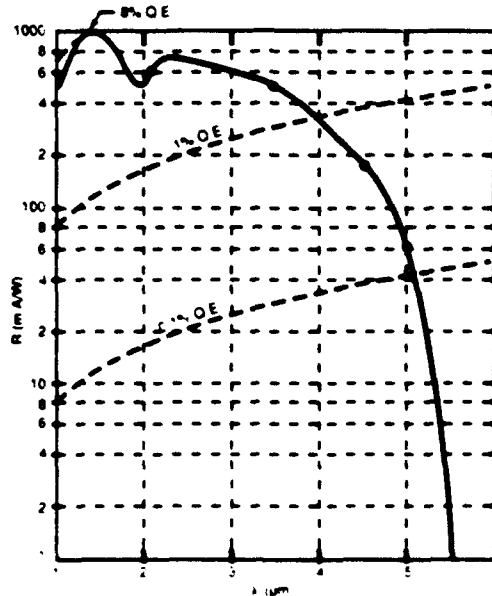


Figure 1. Spectral response of PtSi sensor.

and the detector system's noise-equivalent spectral radiance is given by:

$$\text{NESR}(\lambda_e) = \frac{\sigma_{\text{total}} h \cdot c}{A_p \Omega_p \Delta t \int T_o(\lambda) T_s(\lambda) \lambda F(\lambda, \lambda_e) \eta(\lambda) d\lambda}$$

Where σ_{total} is the RSS combination of collected photon flux Bose-Einstein statistic fluctuations (photon shot noise), instrument background level shot noise, array noise, and readout electronics noise.

Applying appropriate parameters for the detector system using a PtSi detector, namely lens $F/ \# = 1.8$, $l_p = 31 \mu\text{m} \times 25 \mu\text{m}$, $T_o = 25\%$, $F(\lambda, \lambda_e) = \text{Gaussian}$ with FWHM = 0.15% of center wavelength, $\sigma_{\text{array}} = 400$, and $\sigma_{\text{readout}} = 1000$, detector system performance can be assessed. Target radiance comprises two components, reflected and self-emitted. In the phase I proposal, spectral reflectance was assumed to be that of grass, and incident irradiance was assumed to be from the sun. distance from sensor to target was assumed to be 1 km, such that atmospheric absorption was significant in the water and carbon dioxide absorption regions. For this analysis, however, target reflectance was assumed to be the previously measured red paint;

incident irradiance was assumed to be from a bank of quartz-tungsten-halogen (QTH) lamps burning at 2800 K, and producing a luminance (from a 100% reflector) of 1,000 cd/m² (by comparison, sunlight on a white card is roughly 20 times brighter). Atmospheric transmission losses were assumed to be from a 3 meter path. Target temperature was assumed to be 25° C.

Given these parameters, Target spectral radiance from 1.5 μ m to 5 μ m is shown in Figure 2. Also shown is the NESR of the spectral imager using a PtSi array, with the array running at 600 frames per second (fps), 200 fps, and 60 fps. Note that the two higher speeds are actually unobtainable in PtSi, but are given by way of comparison to InSb, which will be presented next.

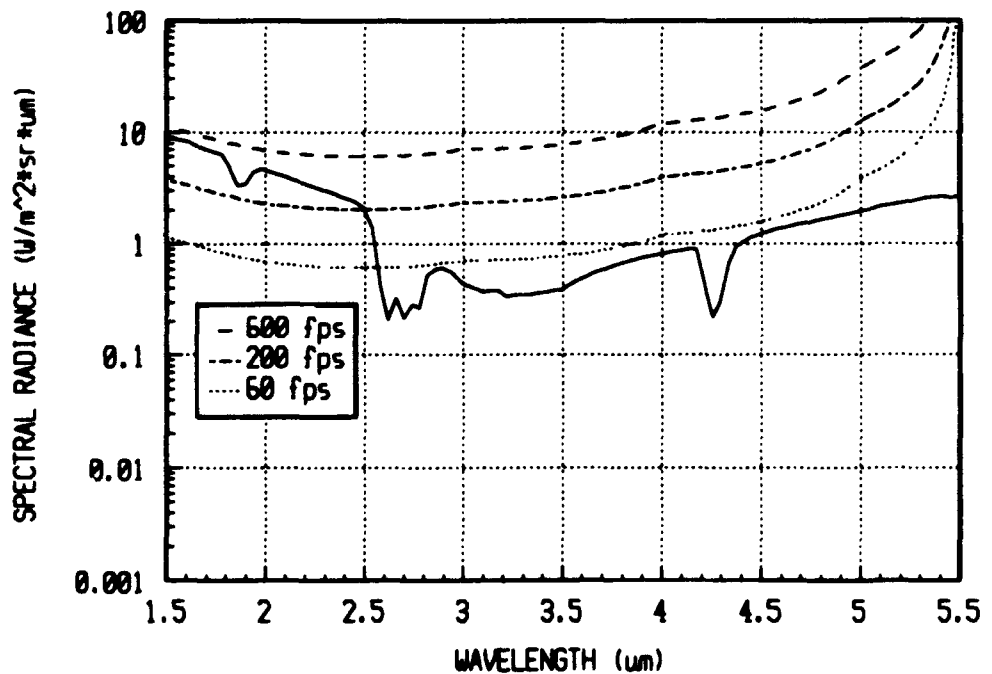


Figure 2. Red paint spectral radiance and PtSi NESR.

This figure clearly displays the performance problem associated with using PtSi in a spectral imager. Even at the "low" frame rate of 60 fps (3 spectra per second with a 20 point spectrum), maximum signal-to-noise ratio is only about 10. Over the majority of the spectral range, NESR is greater than the spectral radiance at any

frame rate, indicating SNR less than 1; clearly this is unacceptable performance. The fact that PtSi arrays are not available with frame rates above 60 fps is also a major problem, since the spectral imager is intended to run at high frame rates (under appropriate radiance conditions) in order to achieve processed image rates near video rates of 30 Hz.

Figure 2 presents target radiance and NESR at target temperature of 25° C. Another way to examine instrument performance is to plot signal-to-noise ratio versus target temperature. As target temperature and, hence, radiance increases, so will SNR. Such a plot is useful in determining instrument performance against targets of elevated temperature. Figure 3 shows the PtSi spectral imager's temperature dependant SNR at 2 μ m, 3 μ m, 3.5 μ m, 4 μ m, and 5 μ m (based on a fictitious 600 fps array). Note that SNR for any wavelength does not exceed 10 until target temperature is over 200° C. PtSi, then, although attractive for its relatively low cost and good uniformity, is completely unacceptable for developing a spectral imager because of its poor quantum efficiency.

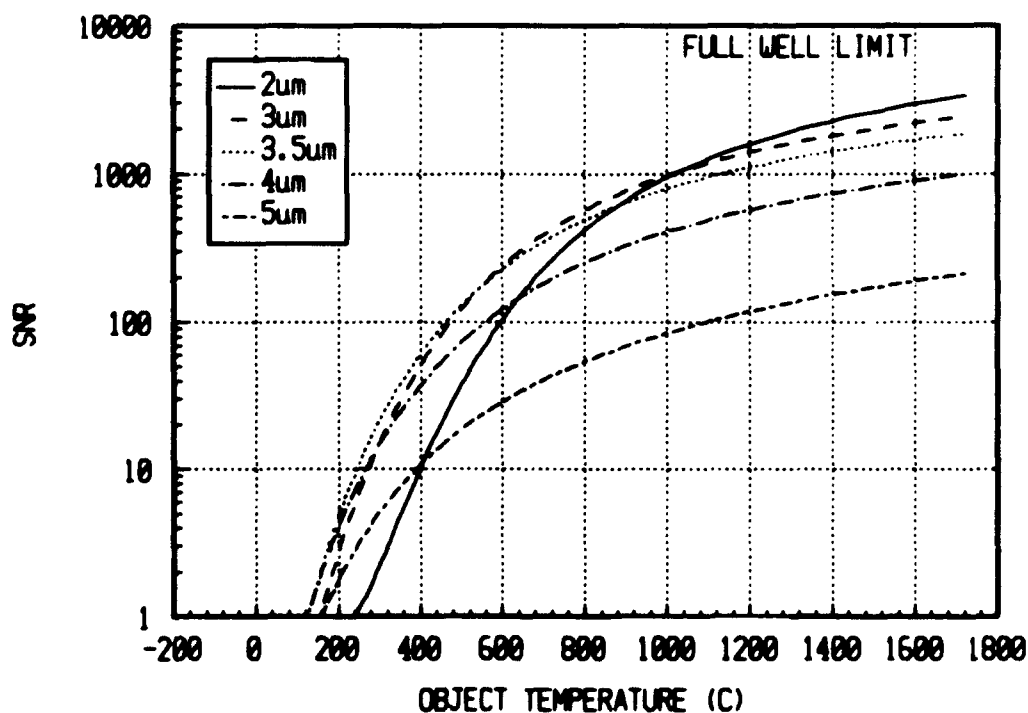


Figure 3. PtSi spectral imager SNR versus temperature.

2.1.1.2 Indium-Antimonide Performance

Indium-Antimonide, with a nearly constant 50% to 70% quantum efficiency from about 1.5 μm to 5.5 μm , exhibits dramatically improved performance relative to PtSi. Using the same conditions as above to elicit the performance of and InSb equipped spectral imager yield the NESR curves shown in Figure 4. Note that NESR is an order of magnitude lower at short wavelength, and 2.5 orders of magnitude lower at 5 μm than for PtSi. This analysis was carried out assuming readout noise is similar to what is already achieved in SOC's visible band instrument.

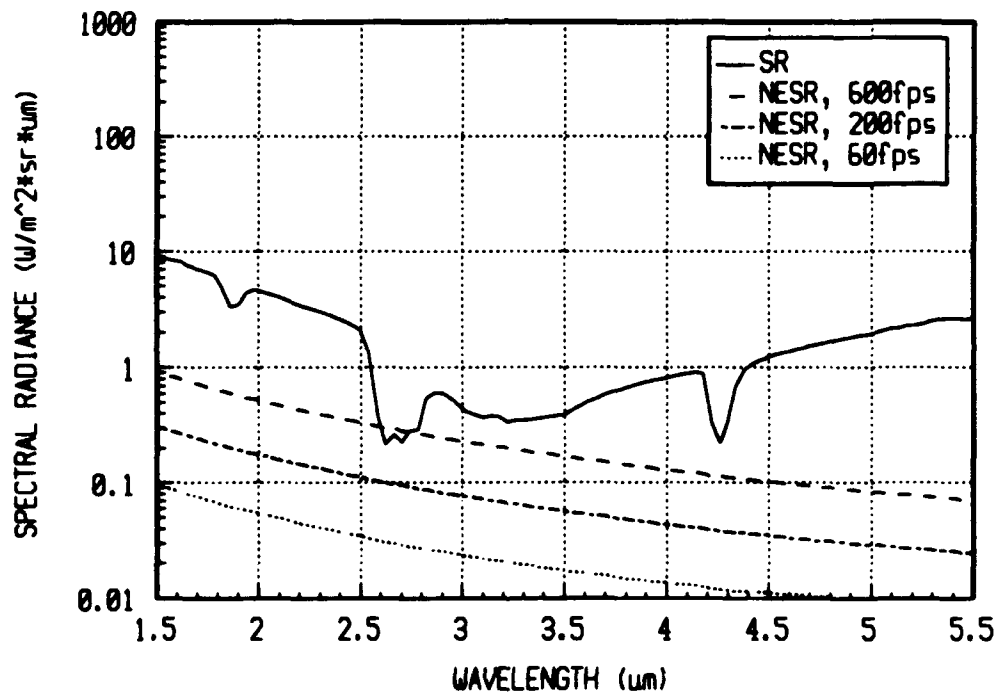


Figure 4. Paint spectral radiance and InSb NESR.

The smooth shape of the curves show that the instrument is readout-noise limited at these frame rates. To investigate the increase in performance that would be achieved by decreasing readout noise, an analysis of NESR was conducted assuming that readout noise was negligible compared to the 400 electron detector noise. Results of this analysis are shown in Figure 5.

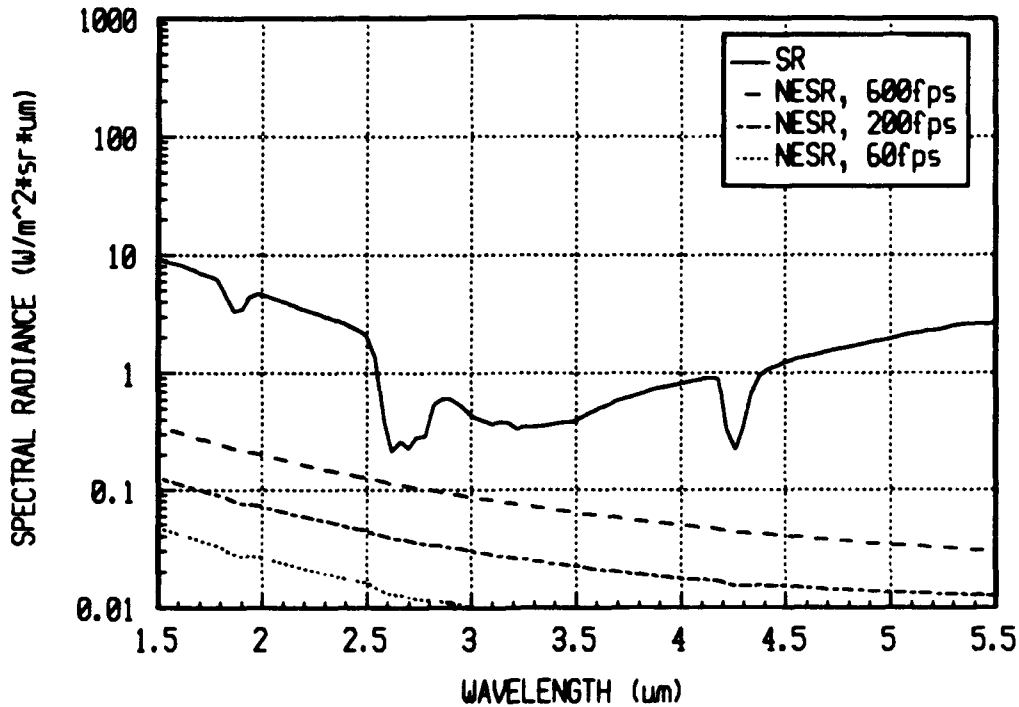


Figure 5. Paint spectral radiance and reduced read-out noise InSb NESR.

Note that the decreasing electronics noise from 1080 electrons to 400 electrons drops the 600 fps NESR by a factor of 2.5, indicating that at this frame rate, the instrument is still electronics noise limited. At lower frame rates, however, some of the spectral radiance features begin to appear in the NESR indicating the onset of quantum-noise limitation. Hence, when detailed design of the readout electronics commences, special attention will be given to decreasing noise, including limiting bandwidth at lower frame rates, where pixel rates decrease.

Temperature dependant SNR performance was also elicited for the InSb-based spectral imager. Results of this analysis are shown in Figure 6. Note the dramatically improved performance of the InSb system over the previously discussed PtSi system. Leveling out of the 2 μ m SNR curve at low temperature is caused by radiance being dominated by reflected rather than emitted light.

MWIR Mercury-Cadmium-Telluride exhibits similar performance to InSb and at similar cost. Hence, InSb is the clear choice for the SWIR/MWIR sensor for this instrument. Two different arrays, one from Amber and one from Litton Electron Devices, both offer exceptional performance. The Litton array is a somewhat better

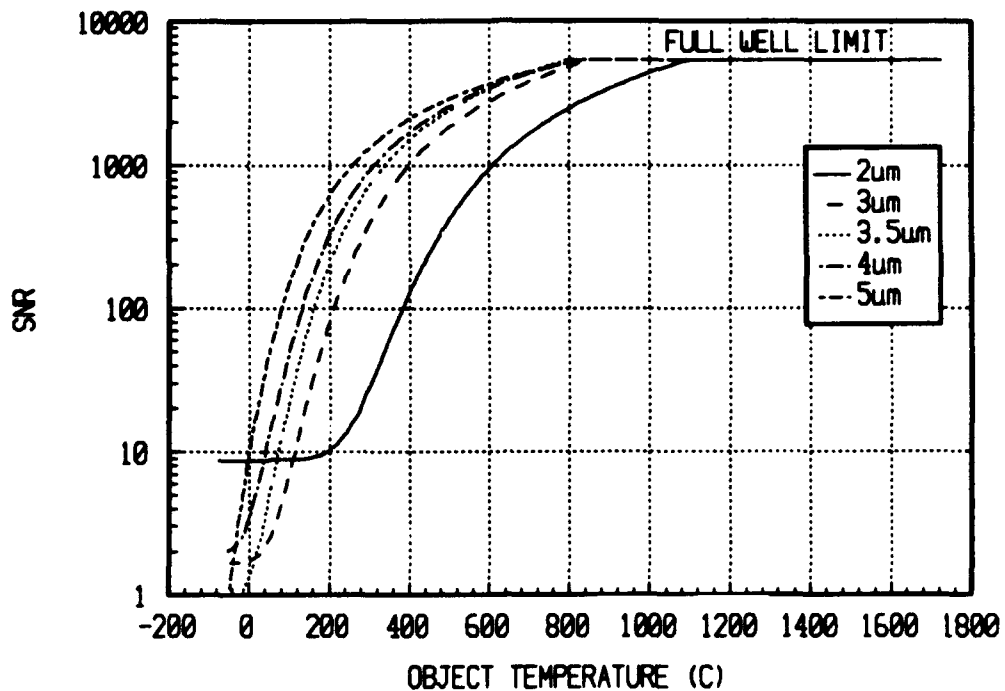


Figure 6. InSb spectral imager SNR versus temperature.

array than the Amber array (offering higher maximum frame rate), but is also more expensive. Litton expects the price of their array to drop, so both arrays will be reconsidered at the time when it is necessary to purchase one for the prototype to be built under the phase II effort.

2.1.2 Long-Wave Infrared Detector

Two different detector technologies have been investigated for the LWIR head of this instrument, namely HgCdTe, and extrinsic Silicon (Silicon doped with an impurity such as arsenic or gallium). Long wave HgCdTe arrays are available, but the technology is not as well developed as it is for SWIR/MWIR detectors. Hence, LWIR HgCdTe arrays are rather expensive. These detectors offer cutoff wavelengths in the 10 μm to 12 μm range, and operate at liquid Nitrogen temperatures (77 K), temperatures readily achieved with closed-cycle coolers. Extrinsic Silicon offers cut-off wavelengths as high as 18 μm to 30 μm , but their operation is complicated by the fact that they operate at liquid Helium temperatures.

2.1.2.1 Mercury-Cadmium-Telluride

Noise performance of a spectral imager using a 256 x 256 HgCdTe array from Hughes-SBRC was conducted to elicit imager performance. Pixel size for HgCdTe is similar to that of InSb. Quantum efficiency is about 70% from 5.5 μm to about 11 μm . Detector noise of the Hughes-SBRC array is a high 2800 electrons. Other HgCdTe arrays are currently being investigated to see if any better arrays exist. Figure 7 shows the NESR of a spectral imager using a HgCdTe array from SBRC. Temperature dependent SNR is plotted in Figure 8. Note that NESR and SNR are very good throughout the 5.5 μm to 11 μm range.

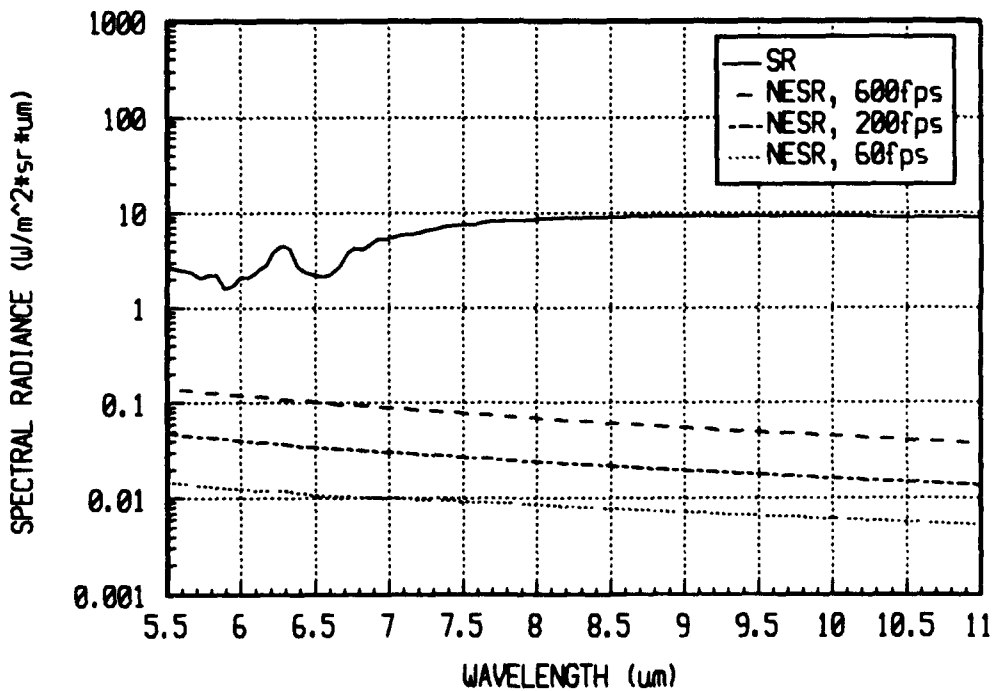


Figure 7. HgCdTe spectral imager NESR and red paint spectral radiance.

2.1.2.2 Extrinsic Silicon

Two types of extrinsic silicon have been investigated, namely Arsenic doped Silicon (Si:As) BIB detectors, and Gallium doped Silicon (Si:Ga). Arsenic doped

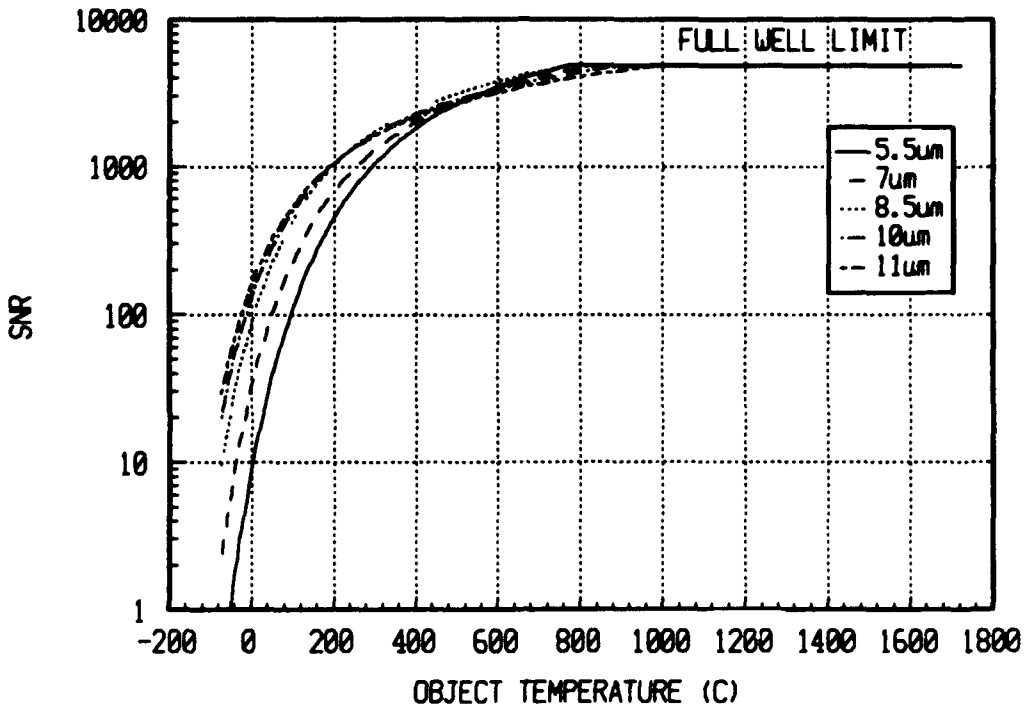


Figure 8. HgCdTe spectral imager SNR versus temperature.

Silicon, operated at a frigid 14 K, has a useful spectral range from about 3 μm to 30 μm ; quantum efficiency starts at 10% at 3 μm , rises to 50% at about 14 μm , stays at about 50% out to 24 μm , then falls to 10% at 30 μm . Gallium doped Silicon's quantum efficiency curve is similar, except that it cuts off at 18 μm when operated at 25°K. NESR and temperature dependent SNR of Si:As are presented in Figures 9 and 10, respectively. NESR for the extrinsic silicon is much lower than the HgCdTe, since the pixels of the Si:As are nearly 4 times the area of the HgCdTe pixels.

2.2 Imager Head Design

As originally envisioned in the phase I proposal, the MIIRIS instrument would generate spectral images by forming a primary image, generated by the front-end objective lens, on a CVF; the primary image would then be relayed to the detector through a relay lens system. This approach, however, is complicated by the fact that the relay lens system must be twice as fast as the objective lens if the image on the detector is to remain unvignetted. If the relay has the same F/# as the objective,

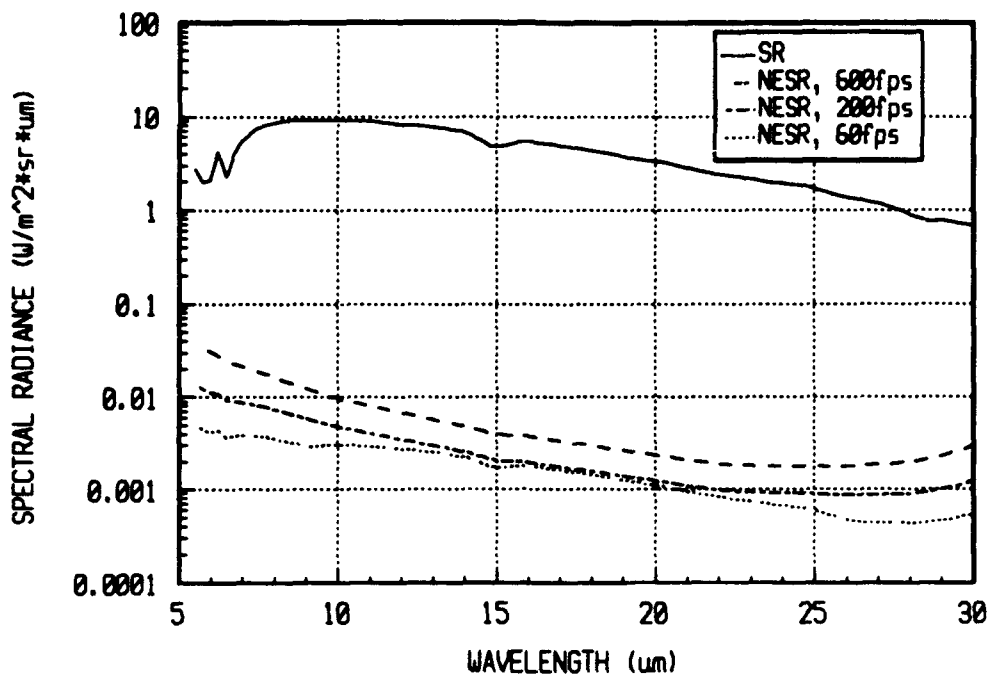


Figure 9. Si:As NESR and red paint spectral radiance.

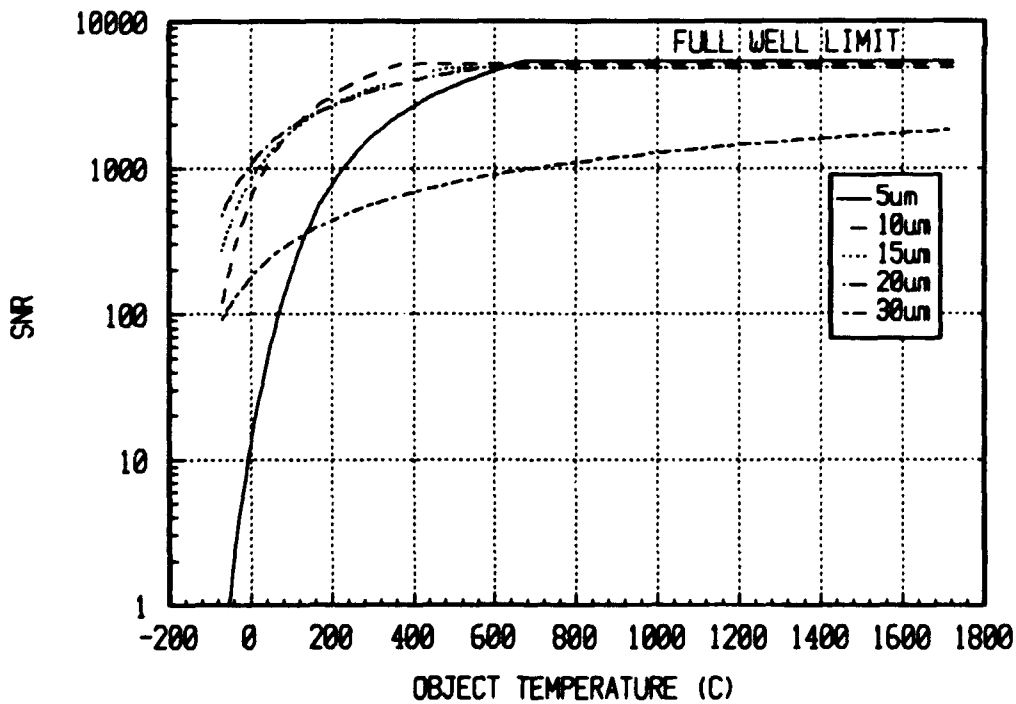


Figure 10. Si:As spectral imager versus temperature.

then transmission of the primary image to the detector will be near 100% at the center of the detector, but could fall to as little as 30% at the corners of the image.

Although individual pixel calibration can compensate for vignetting, signal-to-noise ratio will decrease as pixels move off axis due to the decreased signal level.

SOC's original visible-band prototype instrument suffered from this phenomenon, since the original customer did not want SOC to spend the time required to design and fabricate an F/0.9 relay optic. Even given the time, however, design and fabrication of such an optic is an extremely challenging and expensive task. This problem was solved in the second version of the visible-band instrument by resorting to the method originally envisioned: rather than relaying the image from the CVF to the detector with a relay lens, the detector was effectively placed directly behind the CVF, with a gap of about 0.010" between the CVF and detector. Since the visible-band instrument uses an intensifier in front of the detector, this task was accomplished by bonding a fiber-optic taper onto the input optic of the intensifier; this taper protruded about three-quarters of an inch in front of the intensifier and ended just behind the CVF. This approach greatly simplifies the optical train, increases performance, and saves cost.

Such an approach, however, was not originally seen as viable for the IR version of the instrument for two reasons: first, no IR fiber optic bundles are currently commercially available; second, the cryogenically cooled IR detector resides in an evacuated dewar behind an input window and cold shield. Placing this assembly directly behind the CVF would produce a gap of about half an inch between the detector and CVF, even if the detector dewar's input window were placed thousandths of an inch behind the CVF. Bandwidth of the resultant spectral imager would then be several times greater than the bandwidth of the CVF alone.

Clayton Labaw from JPL, however, with his expertise in designing optical systems both for space and terrestrial use, saw the solution to this problem. Rather than enclose the detector in its own evacuated dewar, the entire optical head would act as the dewar. JPL has extensive experience in designing such assemblies, and in using motors and actuators in vacuum environments. By evacuating the entire head, the detector no longer need reside in its own enclosure, so it can be positioned directly behind the CVF, removing the need for any relay optic; optical train is then greatly simplified, performance enhanced, and cost minimized. The optical head

would then need to be sealed, necessitating an input window where the objective lens mounts. This approach also makes the imaging head design much more universal and flexible. A single head design will work just as well for the VIS/NIR head as for the SWIR/MWIR head as for the LWIR head. Input lenses can be chosen from any available lenses that fit the lens mount on the front of the head, making for a much more flexible imager. Figure 11 shows the conceptual design of the imaging head assembly with a refractive input lens. A refractive lens would give wide fields of view if so required at the cost of some chromatic image aberrations. Figure 12 shows the same approach, but with a reflective Swarthchild objective lens. This choice of objective would be limited to about 10° fields of view, but would be completely free of any chromatic aberrations. Both approaches are equally easily implemented, since the head stays the same; only the objective lens changes. Not shown in these figures is the motor and cooler mounts which would also serve as heat sinks to conduct heat to the outer housing where it could then be convected away.

Using this approach for the SWIR/MWIR and LWIR heads will greatly simplify the instrument, greatly improve performance and flexibility, and greatly reduce cost and improve maintainability.

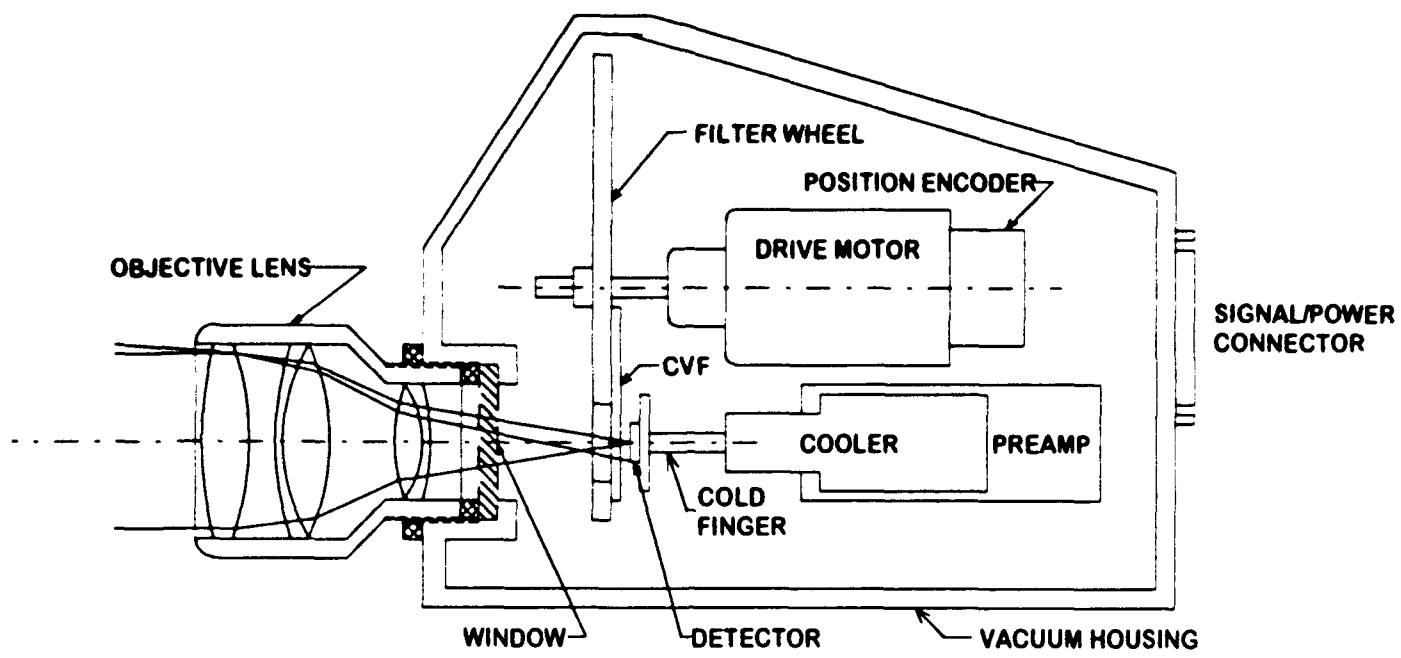


Figure 11. CVF-based high speed spectral imager, VNIR version.

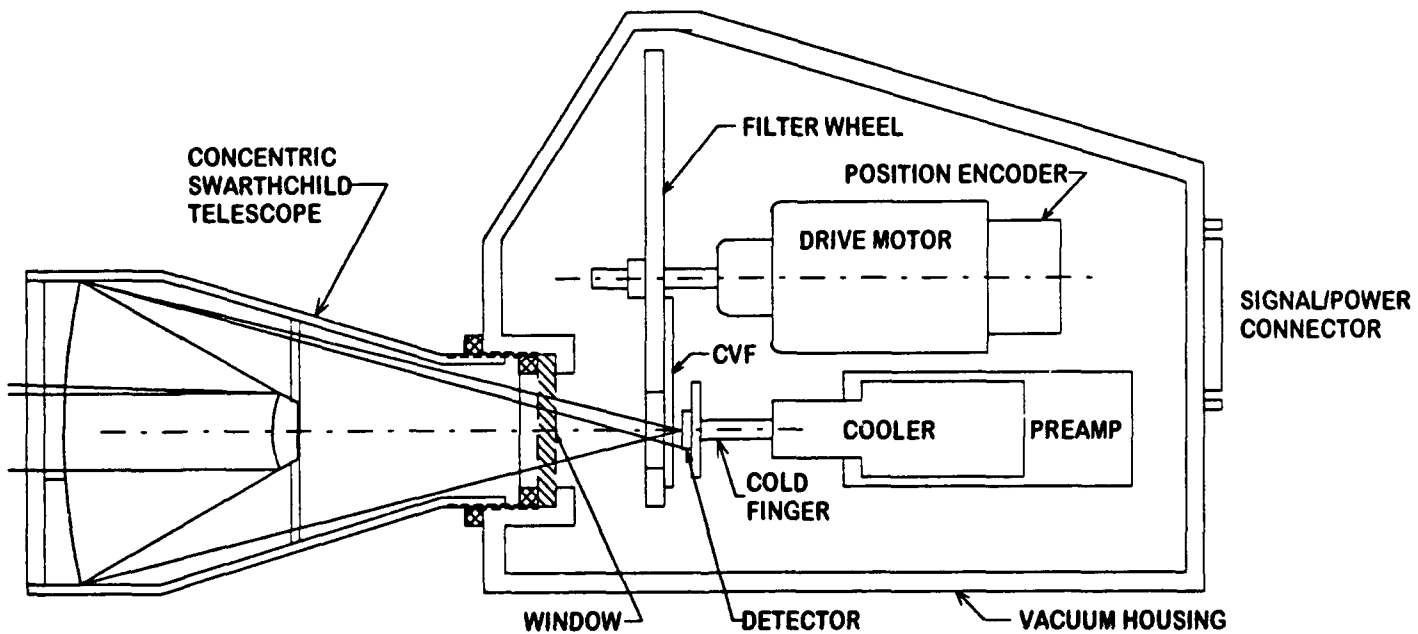


Figure 12. CVF-based high speed spectral imager, all waveband version.

3.0 ANALYTICAL STUDIES

This section describes the simulation studies that were performed to demonstrate the capabilities of imaging infrared spectral radiometry to non-destructive inspection and other applications. Two codes were developed during the course of this program, SPCFLT and TEMPFIT, for the purpose of testing and evaluating algorithms that will eventually be implemented in the imaging spectral radiometer hardware. The following sections provide a theoretical description of the techniques implemented in the code, show the results of simulations performed on the graphite composite and paint samples that were measured for this program, and provide a discussion of the result of the initial studies and describe the areas where the simulation will improved and extended.

3.1 Description of Computer Codes

Two computer codes were written as a test bed for algorithm development and evaluation. The SPCFLT (spectral filtering) code is used to generate and display infrared spectral imagery and process the image using a variety of spectral filtering algorithms. The TEMPFIT code is used to process the spectral radiometric data to obtain information on the material surface temperature and spectral emissivity.

3.1.1 SPCFLT Computer Code

The SPCFLT computer code calculates spectral IR imagery starting from an input file that defines the material temperatures and spectral emissivities for each pixel in the image. The pixels are identified by a material tag which is associated with a specific temperature and emissivity. The spectral emissivity data is obtained from laboratory Hemispherical Directional Reflectance (HDR) measurements that were made for the materials used in the scene. Value of the background temperature and band averaged emissivity are also input parameters to the program. The material spectral radiances are then given by

$$L(\lambda, T) = \epsilon(\lambda)N(\lambda, T) + [1 - \epsilon(\lambda)]\epsilon_b N(\lambda, T_b)$$

where ϵ_b and T_b are the background emissivity and temperature, $\epsilon(\lambda) = 1 - \text{HDR}(\lambda)$ is the material spectral emissivity, and $N(\lambda, T)$ is the Planck black body function. Material spectral radiances are computed for each tag value (unique material and temperature combination) in the scene. The spectral radiances are band averaged and displayed as an image. The spectral radiances are then further processed using spectral algorithms described below and redisplayed to demonstrate the effects of spectral processing.

Given the pixel spectral radiances defined for the materials in the image, the user can perform various spectral filtering algorithms by invoking the Process Image menu item. These algorithms are, by name, dot product, zero-mean dot product (correlation coefficient), derivative dot product, zero-mean derivative dot product (derivative correlation), absolute differential area, zero-mean absolute differential area, derivative absolute differential area, zero-mean derivative absolute differential area, RSS differential area, zero-mean RSS differential area, derivative RSS differential area, and zero-mean derivative RSS differential area. In addition, the images can be integrated with specified sensor response functions in order to simulate the performance of broad band IR imagers for comparison to spectral techniques. The exact form of these filtering algorithms is presented below.

The dot product is a very simple filtering algorithm that treats each spectral radiance as an N -dimensional vector and simply computes the dot product of the two vectors. Formally, this algorithm is given by

$$C_{\text{dot}} = \frac{\sum L(\lambda_n)F(\lambda_n)}{\sqrt{\sum L(\lambda_n)^2 \cdot \sum F(\lambda_n)^2}}$$

Where $L(\lambda_n)$ is the measured spectral radiance at the n^{th} wavelength, and $F(\lambda_n)$ is the filter spectral radiance at the n^{th} wavelength. A major problem with this algorithm is that it is extremely broad. That is, the measured and filter radiances need only

have roughly the same shape in order for the dot product to produce a high correlation value. The dot product generates the cosine between the two vectors acted upon by the algorithm. An N -dimensional vector can lie in any one of 2^N possible dimensional sectors, e.g., a three dimensional vector can lie in any one of 8 octants. Spectral radiances, however, are always positive, constraining radiance vectors to all lie in only one of their 2^N sectors. Hence, all vectors are necessarily forced to point in the same general direction, with the forced match becoming greater as more spectral points are added. How, then, can a tighter filter be implemented while still retaining spectral features?

The zero-mean dot product accomplishes this task. By removing the mean value from each spectral point, the shape of the spectral radiance curve is maintained, but the new zero-mean spectral radiance vector can now lie in any of the 2^N sectors of its N -space. Performing a dot product on the zero-mean radiance vectors then gives a tighter matching algorithm. This algorithm is given formally by

$$C_{ZMDOT} = \frac{\sum (L(\lambda_n) - \langle L(\lambda) \rangle)(F(\lambda_n) - \langle F(\lambda) \rangle)}{\sqrt{\sum (L(\lambda_n) - \langle L(\lambda) \rangle)^2} \cdot \sqrt{\sum (F(\lambda_n) - \langle F(\lambda) \rangle)^2}}$$

where the spectral radiance mean is given by

$$\langle L(\lambda) \rangle = \frac{1}{N} \cdot \sum_1^N L(\lambda_n)$$

and similarly for $\langle F(\lambda) \rangle$. Close inspection of the above equation reveals that applying the zero-mean dot product to two spectral radiances is equivalent to treating those two radiances as sets of discrete random variables and computing the correlation coefficient between the two. Both the dot product and zero-mean dot product can also be applied to the derivative of the spectral radiances to further tighten their matching characteristics by simply replacing $L(\lambda_n)$ and $F(\lambda_n)$ in the above equations with $(L(\lambda_{n+1}) - L(\lambda_n)) / (\lambda_{n+1} - \lambda_n)$.

Another completely different type of matching algorithm can be formed by normalizing both the measured and filter radiances such that each encloses unity

area, and subtracting the area "trapped" between the two curves from 1. For two identical spectral radiances, zero area will be "trapped", and the correlation value will be 1. As more and more area lies between the two curves, the correlation value will become smaller and smaller. For this algorithm, area is always defined as positive. This algorithm, the absolute differential area algorithm, is implemented formally by

$$C_{ADA} = 1 - \sum \left| \frac{L(\lambda_n)}{\sum L(\lambda_n)} - \frac{F(\lambda_n)}{\sum F(\lambda_n)} \right|$$

Although the absolute differential area algorithm is a tighter matching algorithm than the dot product, it suffers from the same problem as the dot product in that all spectral radiance values are positive; again subtracting the mean from each spectral radiance value and using the resultant radiance values in the above algorithm yields the zero-mean absolute differential area algorithm, given formally by

$$C_{ZADA} = 1 - \sum \left| \frac{L(\lambda_n) - \langle L(\lambda) \rangle}{\sum (L(\lambda_n) - \langle L(\lambda) \rangle)} - \frac{F(\lambda_n) - \langle F(\lambda) \rangle}{\sum (F(\lambda_n) - \langle F(\lambda) \rangle)} \right|$$

Note that in the zero-mean absolute differential area algorithm, if the zero-mean spectral radiances are mirror images of each other, then the area trapped between them will be 2, such that C_{ZADA} will have a value of -1, indicating exact anti-correlation. Using the derivative of the measured and filter spectral radiances in either the absolute differential area or zero-mean absolute differential area algorithm yields even tighter matching algorithms.

The final class of algorithms investigated and analyzed in the processing code is similar to the absolute differential area but rather than using absolute area, it uses RSS area. That is, the RSS value of each spectral radiance is normalized to unity, and the RSS area trapped between the resulting radiances is computed. The RSS differential area algorithm is given formally by

$$C_{RSSDA} = 1 - \sqrt{\sum \left(\frac{L(\lambda_n)}{\sqrt{\sum L(\lambda_n)^2}} - \frac{F(\lambda_n)}{\sqrt{\sum F(\lambda_n)^2}} \right)^2}$$

and the zero-mean RSS differential area algorithm, of course, is given by

$$C_{\text{ZERSSDA}} = 1 - \sqrt{\sum \left(\frac{L(\lambda_n) - \langle L(\lambda) \rangle}{\sqrt{\sum (L(\lambda_n) - \langle L(\lambda) \rangle)^2}} - \frac{F(\lambda_n) - \langle F(\lambda) \rangle}{\sqrt{\sum (F(\lambda_n) - \langle F(\lambda) \rangle)^2}} \right)^2}$$

Using the derivative of spectral radiance in either of these algorithms creates yet tighter filtering algorithms.

In the infrared, the shape of the individual material spectral radiance curves is dominated by the shape of the Planck black body function, which reduces the efficacy of the spectral matched filter algorithms described above. One way to overcome this difficulty is to normalize the material spectral radiance curves to the Planck function for an estimated surface temperature. For this case, the individual spectral radiance values are divided by the Planck black body radiance at each wavelength,

$$\epsilon_e(\lambda) = L(\lambda)/N(\lambda, T)$$

providing an estimate of the "effective" emissivity of each material. These emissivities are not the actual surface emissivity because background/atmospheric radiance effects and actual surface temperatures have not been taken into account. However, the "effective" spectral emissivities provide a much better estimate of actual material spectral variations, and are used in place of the radiance values in the spectral filtering algorithms. Techniques for estimating actual material spectral emissivities and surface temperatures based on spectral radiometric data are discussed below.

3.1.2 TEMPFIT Computer Code

The capability of measuring spectral radiometric data provides the opportunity for obtaining detailed emissivity and temperature information about the materials in the scene. The TEMPFIT code is a test bed for developing algorithms for simultaneous temperature and emissivity determination from the spectral radiometric data. The first code generates synthetic spectral radiances using HDR measurements in the same manner as the SPCFLT code. Then the code inverts this data to "recover"

the spectral emissivity and surface temperature using a number of different techniques.

The spectral radiance for a material isolated on a particular pixel can be written as

$$L(\lambda, T) = \epsilon(\lambda) N(\lambda, T) + [1 - \epsilon(\lambda)] L_b(\lambda)$$

or,

$$L(\lambda, T) = \epsilon(\lambda) [N(\lambda, T) - L_b(\lambda)] + L_b(\lambda)$$

where $L_b(\lambda)$ is the spectral background radiance. Given $N+1$ spectral measurements, this set of equations can be solved for N spectral emissivities, $\epsilon(\lambda_i)$, and the temperature. Since the Planck function is non-linear, non-linear data fitting techniques, such as the Levenberg-Marquardt method, must be used. A number of approaches to solving this problem have been described in the literature,^{1,2,3} including using ratios of intermediate observations, and curve fitting the spectral emissivity.

Our approach has involved curve fitting spectral emissivity using a Legendre expansion⁴ and iterating the temperature to find the best chi-squared fit to the spectral radiance data. The Legendre expansion is given by,

¹Ng and Williams, "Full-spectrum multi-wavelength pyrometry for nongray surfaces," SPIE Vol. 1682, p 260.

²Lindermeir, Tank, and Haschberger, "Contactless measurement of the spectral emissivity and temperature of surfaces with a Fourier transform spectrometer," SPIE Vol. 1682, P 354.

³Barani and Tofani, "Comparison of some algorithms commonly used in infrared pyrometry: a computer simulation," SPIE Vol. 1467, p 458.

⁴Spitzberg, "Spectrum Analysis Techniques for Non-Grey Targets." Conference on Optical Discrimination Algorithms, 17 October 1991, TBE, Huntsville, AL.

$$\epsilon(\lambda) = \sum_{k=1}^M a_k \cdot P_k(\lambda)$$

Given a set of ($i=1, \dots, N$) measured spectral pixel radiances, $L_m(\lambda_i)$, solve for the set of M ($M < N$) Legendre coefficients, a_k , that minimizes the equation,

$$SSQ = \sum_{i=1}^N \{L_m(\lambda_i) - L(\lambda_i)\}^2$$

which will yield spectral estimates of $\epsilon(\lambda_i)$, and the temperature, T , of the material in the pixel. So far, we have investigated four methods for solving this problem: a full, non-linear least squares approach using the Levenberg-Marquardt method, two linear techniques using Singular Value Decomposition (SVD) and Gauss-Jordan elimination for solving the normal equations, and manually stepping through the temperature grid, and an iterative ratio technique.

As was the case for the spectral filtering algorithms, curve fitting the spectral emissivity using radiance data is dominated by the shape of the Planck function and better fits were obtained from a normalized radiance equation

$$L_{norm}(\lambda, T_g) = \frac{L(\lambda, T_g) - L_b(\lambda)}{N(\lambda, T_g)}$$

where $L_b(\lambda)$ is a measurement (or guess) of the background spectral radiance, and T_g is a guess at the surface temperature.

3.2 Results

The SPCFLT and TEMPFIT codes were used to simulate two of the NDI applications that were discussed in the previous progress report; remote identification of rust versus red paint on metal substrates and identification of surface contamination on graphite composite materials. The simulations were performed based on laboratory HDR measurements that were made on samples of these materials. Complete documentation of the measurement procedure, tabular and

graphical results was presented in the previous progress report. For both simulations, the background radiance and effective background temperature were calculated in the 3 to 5 and 8 to 12 micron bands using LOWTRAN7, assuming a standard mid-latitude summer sky background.

The first example is the determination of the spectral emissivity and surface temperature of the red paint sample. Figure 13 shows the spectral HDR of the red paint (FS6830) that was measured in the laboratory. Figure 14 shows the simulated spectral radiance of the material at a temperature of 295 K, in the 3 to 5 micron band (diamonds) and the spectral radiance of the Planck black body function (solid curve) at the same temperature. The difference between these two curves is simply the spectral emissivity of the red paint. This clearly shows how the structure of the spectral radiance is dominated by the Planck function. Figure 15 shows the Legendre fit to the spectral emissivity using 6 terms in the expansion; the diamonds are the scaled measurements and the solid curve was generated by the fitting function. Figure 16 shows a comparison between the simulated radiance measurements and the fit obtained using the recovered temperature and Legendre emissivity expansion.

One of the difficulties in the recovery of temperature and emissivities from spectral radiance data is that the solutions are not unique. This is shown in the next simulation. Figure 17 shows measurements of the spectral HDR of a low emissivity paint that was made at Surface Optics. The 3 to 14 micron spectral radiance of the sample, shown as diamonds in Figure 18, was calculated using a 295 K surface temperature and 10 K (i.e., zero) background radiance. Because of the reduced radiance from the material due to the low emissivity paint, the temperature recovered was 282.5 K, 12.5 K lower than the actual temperature. The Planck function for 282.5 K is shown as the solid line in Figure 18. The Legendre fit to the temperature scaled emissivity is shown in Figure 19. The fit is quite good, however the actual values should be in the 0.4 to 0.5 range. The lower temperature and higher emissivities still provide a close fit to the simulated measurements, shown in Figure 20. More work need to be done to develop techniques to eliminate this uncertainty; for example, making use of an external, known radiation source, or iterating between mid-wave (3 to 5 micron) and long-wave (8 to 12 micron) solutions.

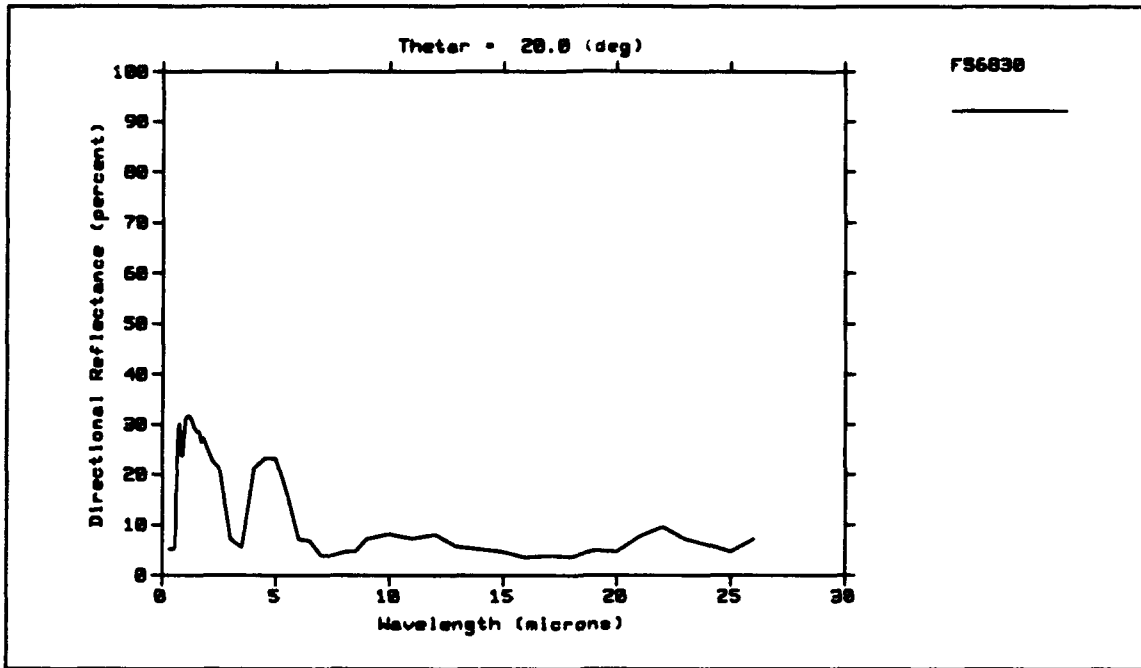


Figure 13. Spectral Hemispherical Directional Reflectance (HDR) measurement of red paint, FS6830.

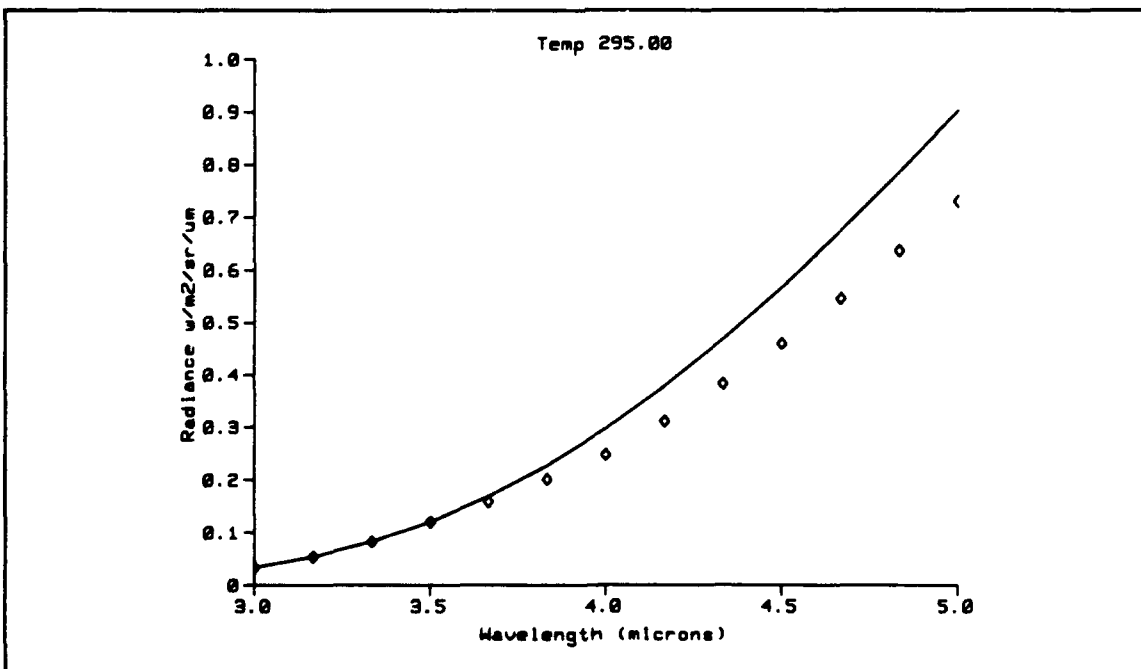


Figure 14. Spectral radiance for red paint sample (diamonds) and Planck function at 295 K.

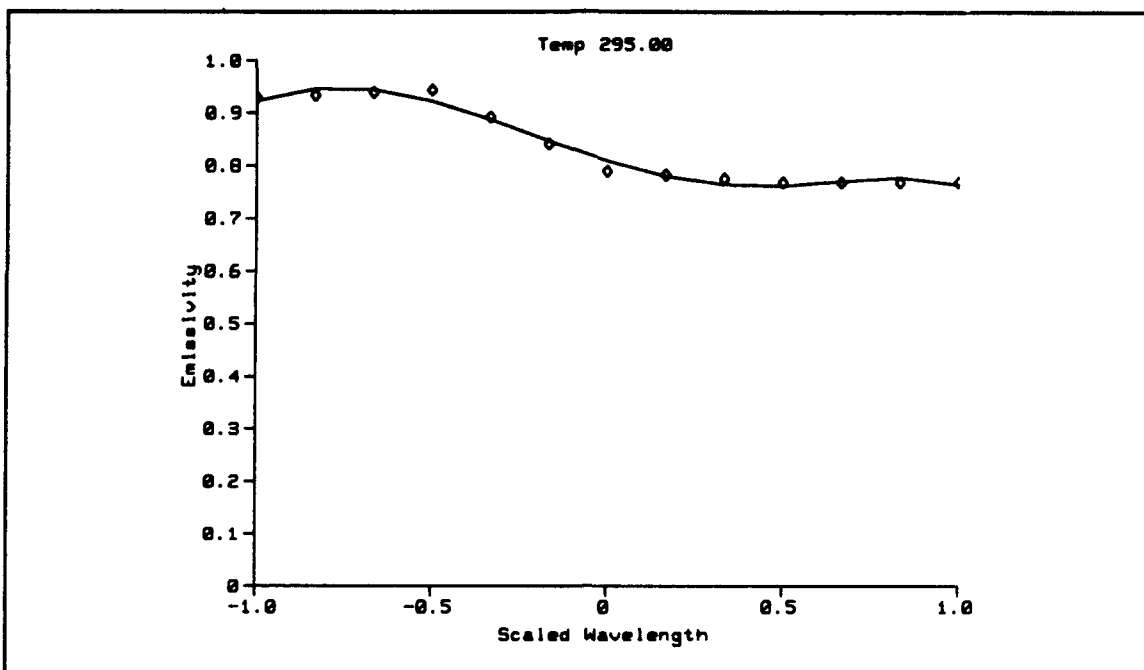


Figure 15. Fit to spectral emissivity data for red paint at guess temperature 295 K.

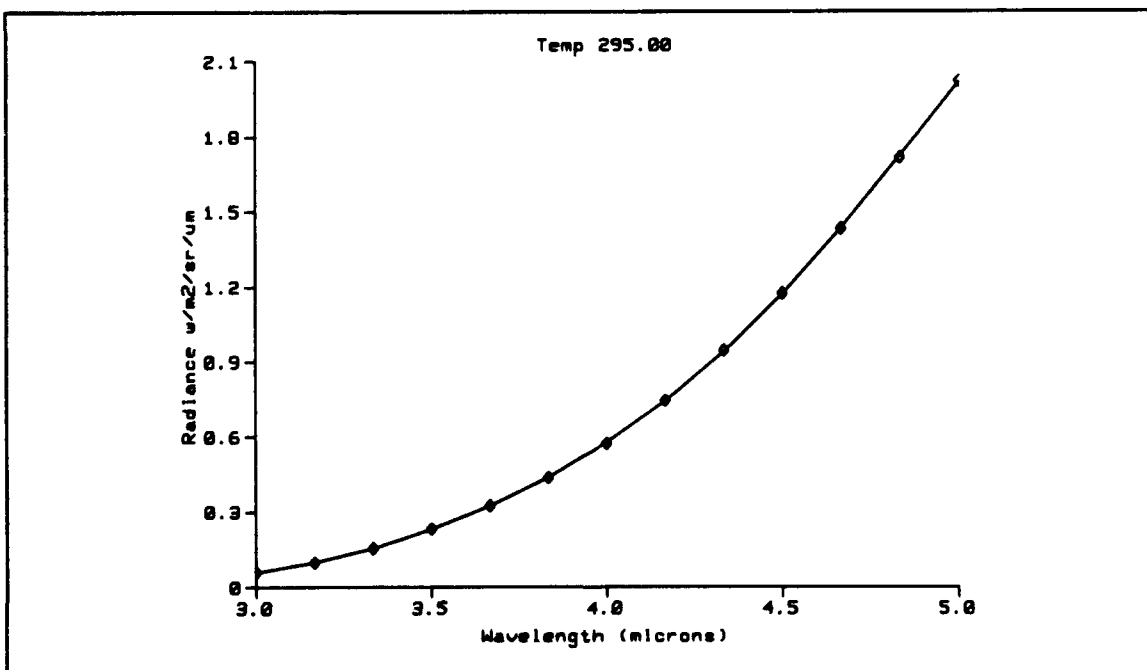


Figure 16. Comparison of spectral radiance data for red paint (diamonds), and the radiance using the emissivity curve fit.

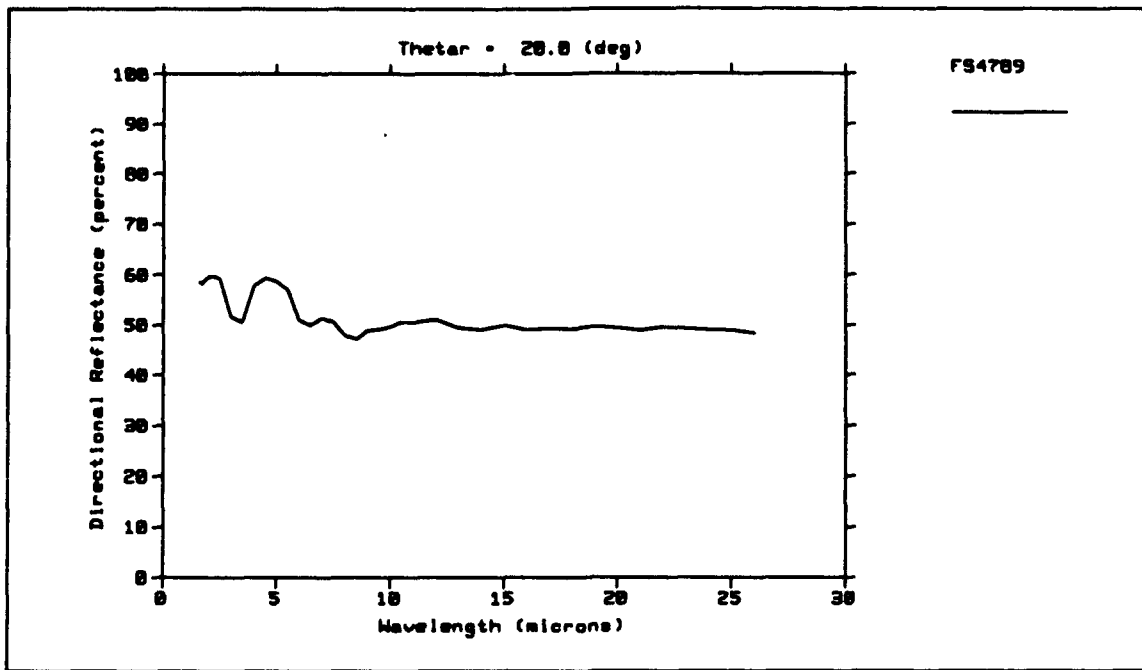


Figure 17. Spectral Hemispherical Directional Reflectance (HDR) measurement of low emissivity paint, FS4789.

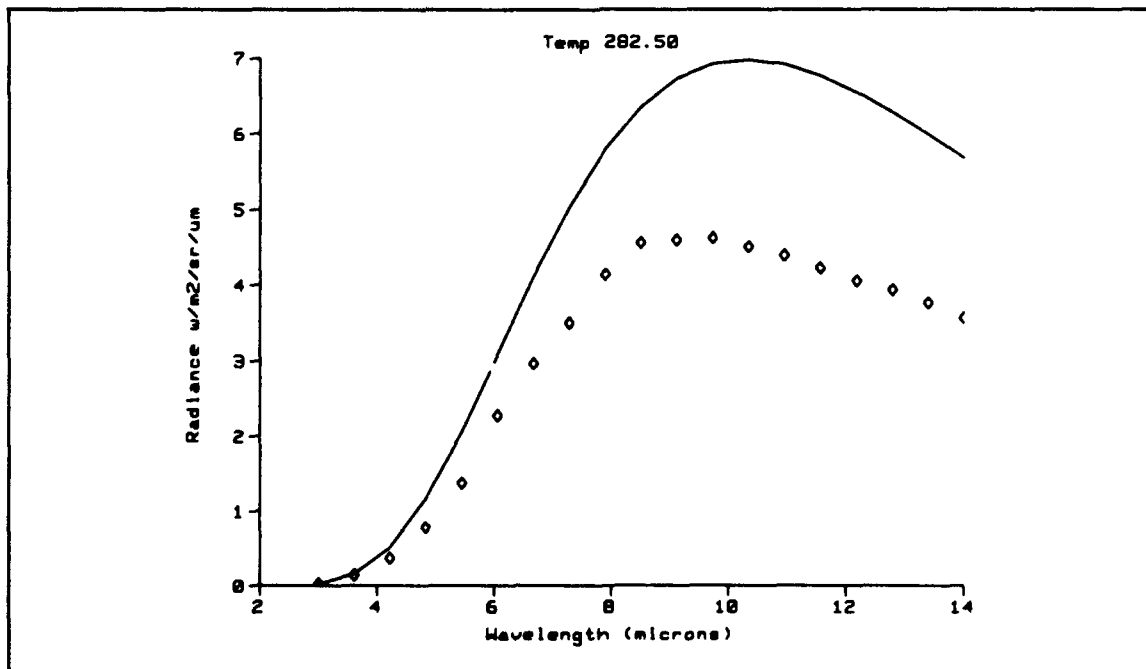


Figure 18. Spectral radiance of low emissivity paint sample (diamonds) and Planck function at 282.5K.

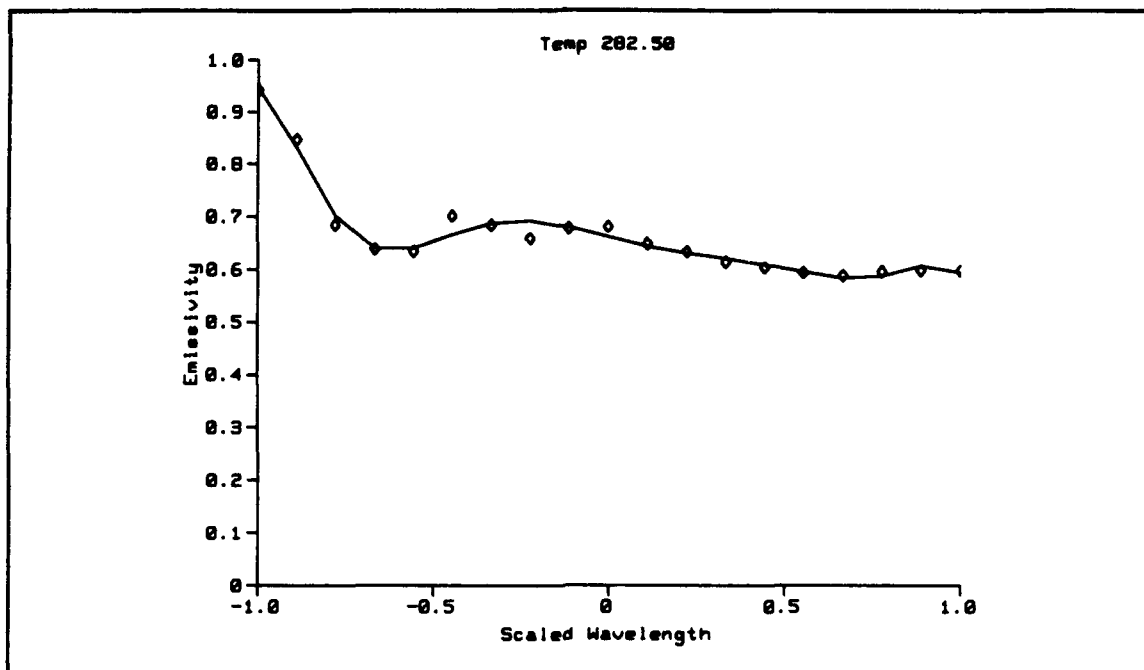


Figure 19. Fit to spectral emissivity data for low emissivity paint at guess temperature 282.5K.

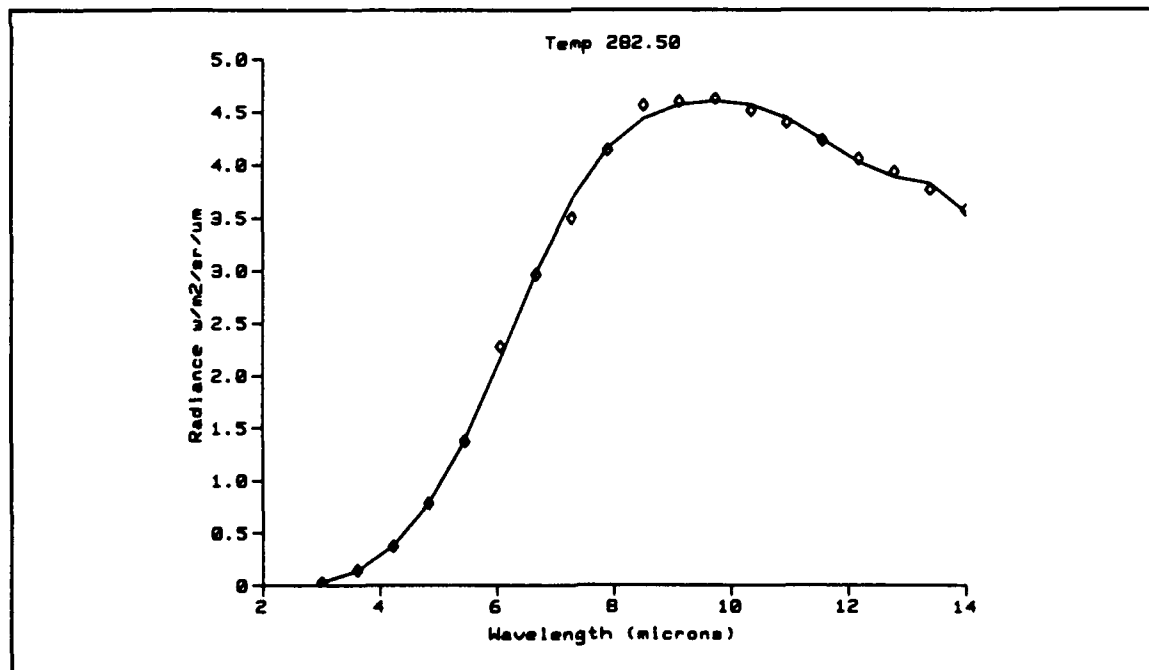


Figure 20. Comparison of spectral radiance data for low emissivity paint (diamonds), and the radiance using the emissivity curve fit.

As a final example of the TEMPFIT program, the temperature and 7 to 14 micron spectral emissivity was determined for the silicon contaminated graphite composite material (FS6854). The spectral HDR measurements for this material are shown in Figure 21. For this case, the simulated measured radiance for a surface temperature of 295 K is shown as diamonds in Figure 22, and the Planck function for the recovered temperature of 293.1 K is the solid curve. Figure 23 shows the Legendre fit to the emissivity data scaled to the recovered temperature, and Figure 24 shows a comparison between the simulated measurements and the radiance calculated using the recovered temperature and emissivity values. Again, the fit is quite good despite absolute temperature and emissivity errors.

The SPCFLT code was used to simulate imagery taken using an IR spectral imaging radiometer. Simulations were made for the rust/red paint materials and the graphite composite materials, and these samples were measured as part of the experimental demonstration, which is described in Section 4. Figure 25 shows a simulated 3 to 5 micron image using spectral emissivity data for four materials: 1) Army tan 686 paint, 2) rust, 3) red paint, and 4) oil contaminated red paint. The spectral HDR measurements for these materials are shown in Figure 26. The panel was defined to be a checker board, at a temperature of 295 K, with patches of these four materials arranged sequentially across the top row. Subsequent rows had materials 1 and 2 and 3 and 4 interchanged; i.e., row 1 materials (1,2,3,4), row 2 materials (2,1,4,3), row 3 materials (1,2,3,4), etc. For the 3 to 5 micron band, the bitmap image dump from the computer screen shows no variation across the panel. The actual computer screen showed small but discernable variations of the 16 color grey scale image. Figure 27 shows the results of differential dot product squared spectral filter after the simulated pixel spectral radiances were normalized by a 295 K Planck function. The spectral radiance of the rust material (number 2) was chosen as the filter function. The simulated filtered image clearly identifies the rust patches on the panel.

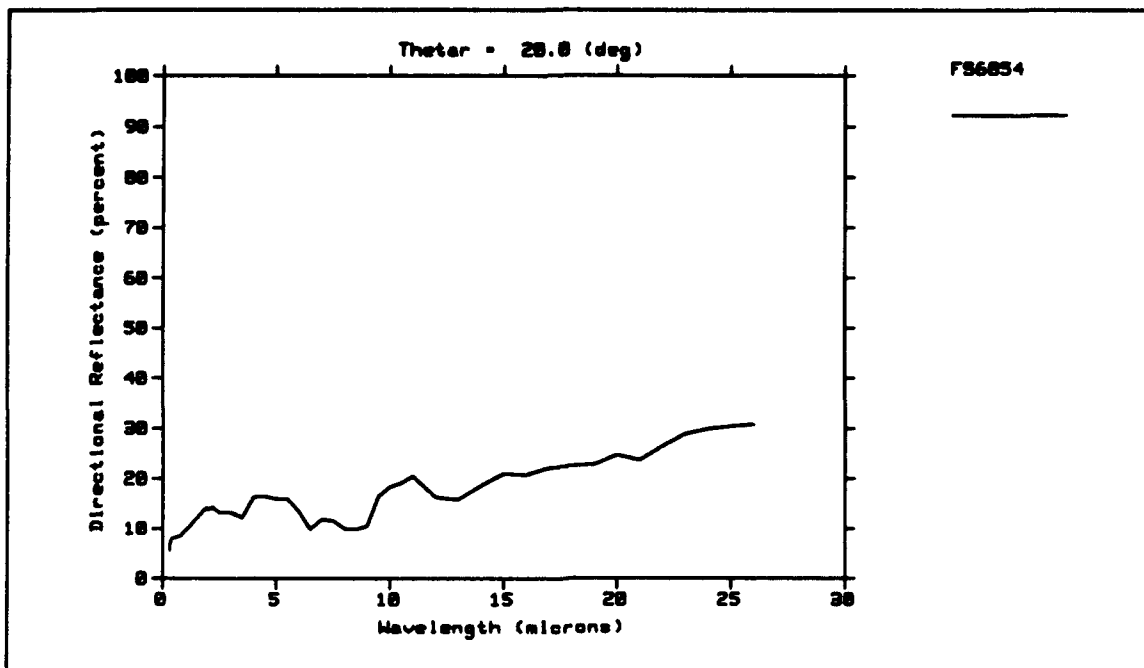


Figure 21. Spectral Hemispherical Directional Reflectance (HDR) measurement of graphite composite sample, FS6854.

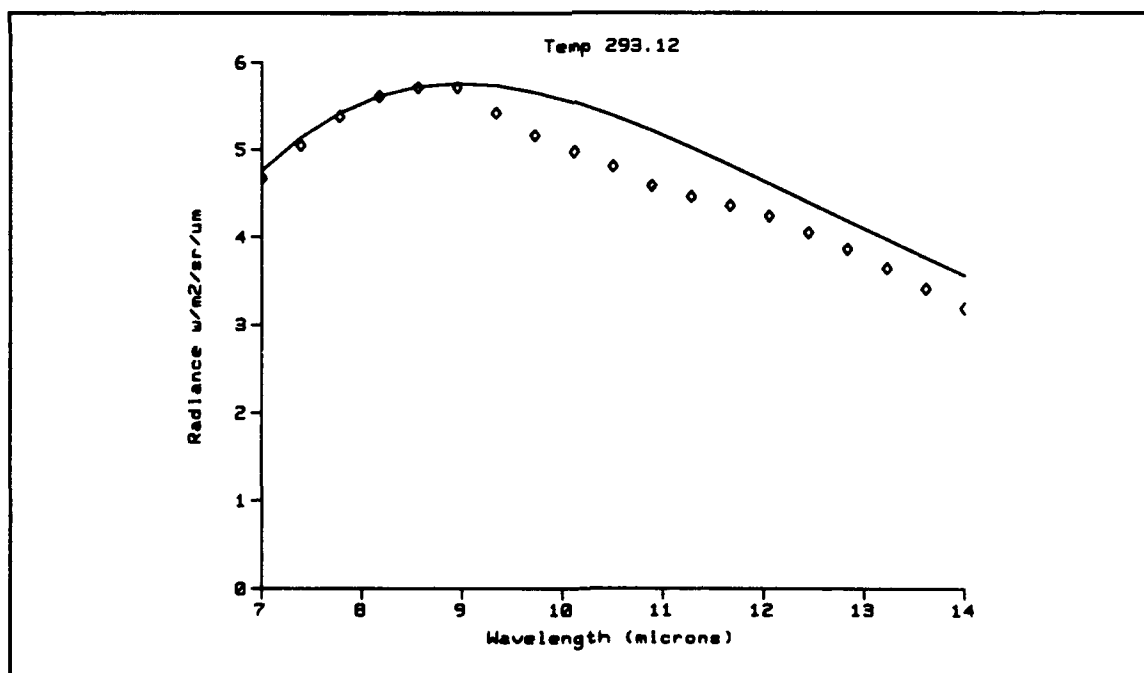


Figure 22. Spectral radiance for graphite composite sample (diamonds) and Planck function at 293.1 K.

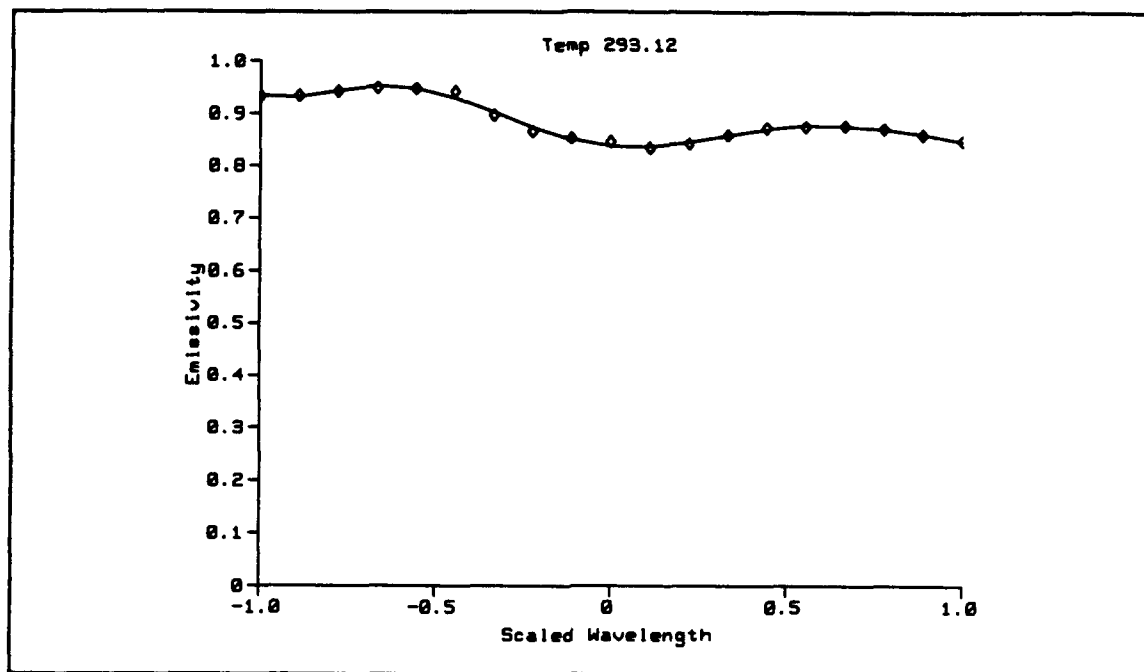


Figure 23. Fit to spectral emissivity data for graphite composite at guess temperature 293.1 K.

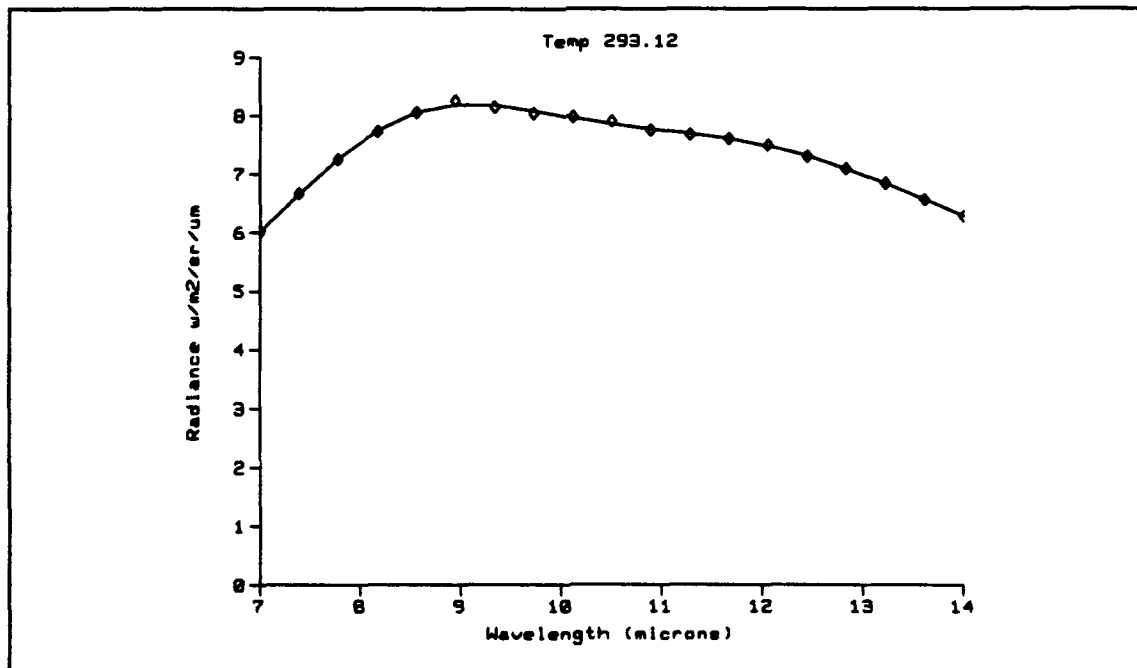


Figure 24. Comparison of spectral radiance data for graphite composite (diamonds), and the radiance using the emissivity curve fit.

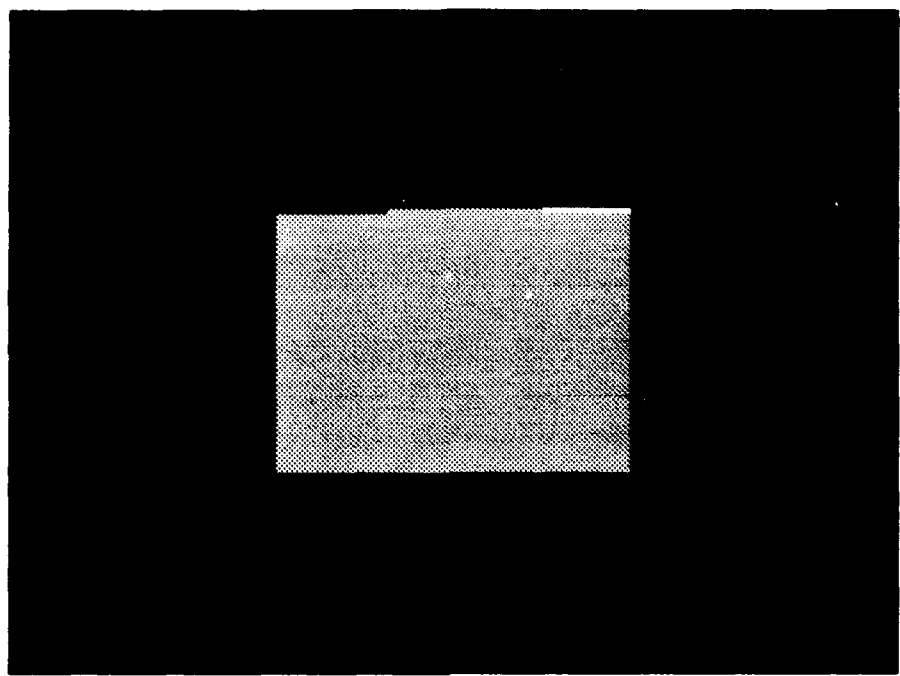


Figure 25. Simulated 3 to 5 micron image of panel painted with checker board pattern of four paint samples shown in Figure 26.

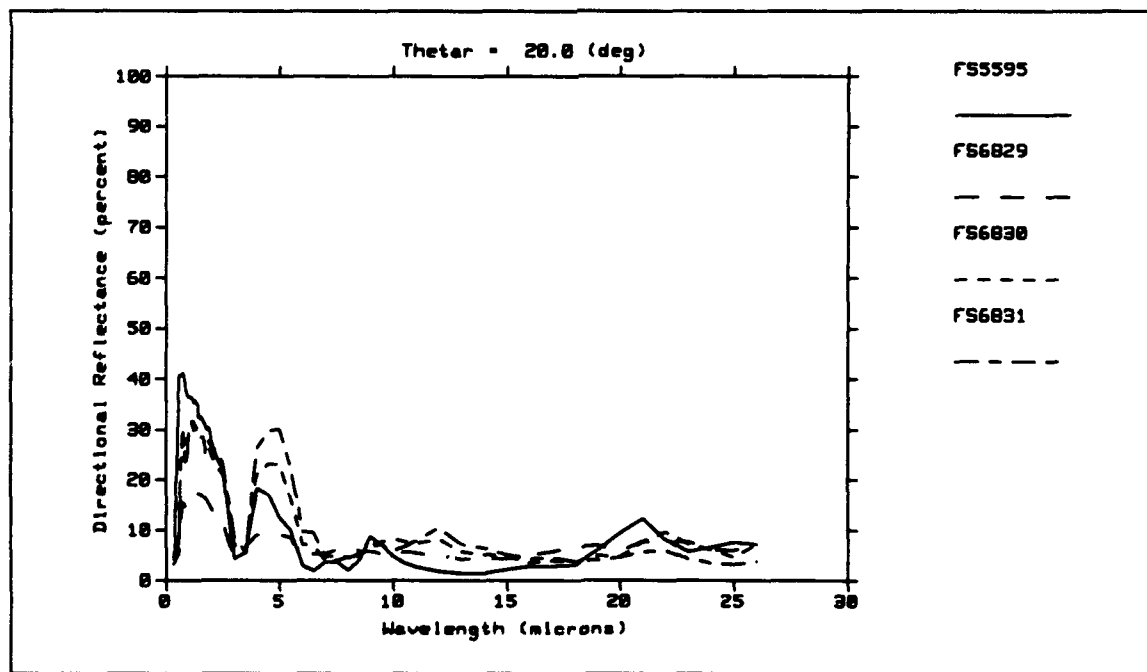


Figure 26. Spectral HDR of the materials used in the simulation: grey paint (FS5595), rust (FS6829), red paint (FS6830), oil contaminated red paint (FS6831).

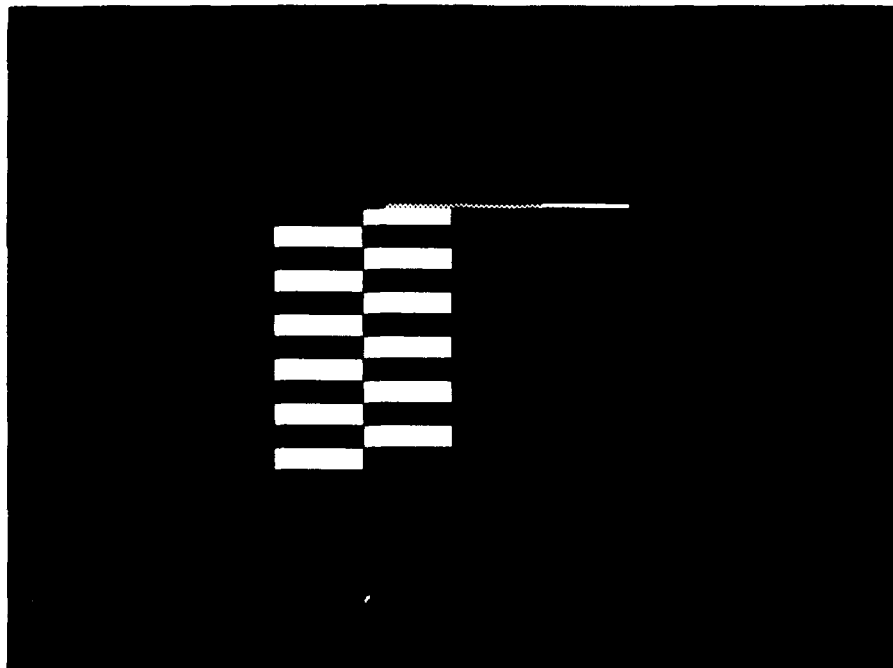


Figure 27. Simulated 3 to 5 micron image of painted panel that has been spectrally filtered using the normalized spectral radiance for the rust sample.

The laboratory measurements of the HDR for the clean and contaminated graphite composite materials, described in the previous progress report, are shown in Figure 28. The panel, at 295 K, was defined as a checker board with materials: 1) silica contaminated graphite composite, 2) uncontaminated graphite composite, 3) fluorine contaminated graphite composite, and 4) graphite composite with unknown contamination. The materials were arranged in a pattern identical to the one described above. The 7 to 14 micron band averaged image produced a bitmap image identical to Figure 25 and is not shown, although the screen image again displayed small but discernable radiance variations. The filtered image, shown in Figure 29, was produced using the differential dot product squared filter, and the normalized spectral radiance of the silica contaminated material. The pixel spectral radiances in the image were all normalized to the Planck function at 293 K, corresponding to the temperature recovered using the TEMPFIT code. Here again, the patches containing the silica contaminated material are clearly identified.

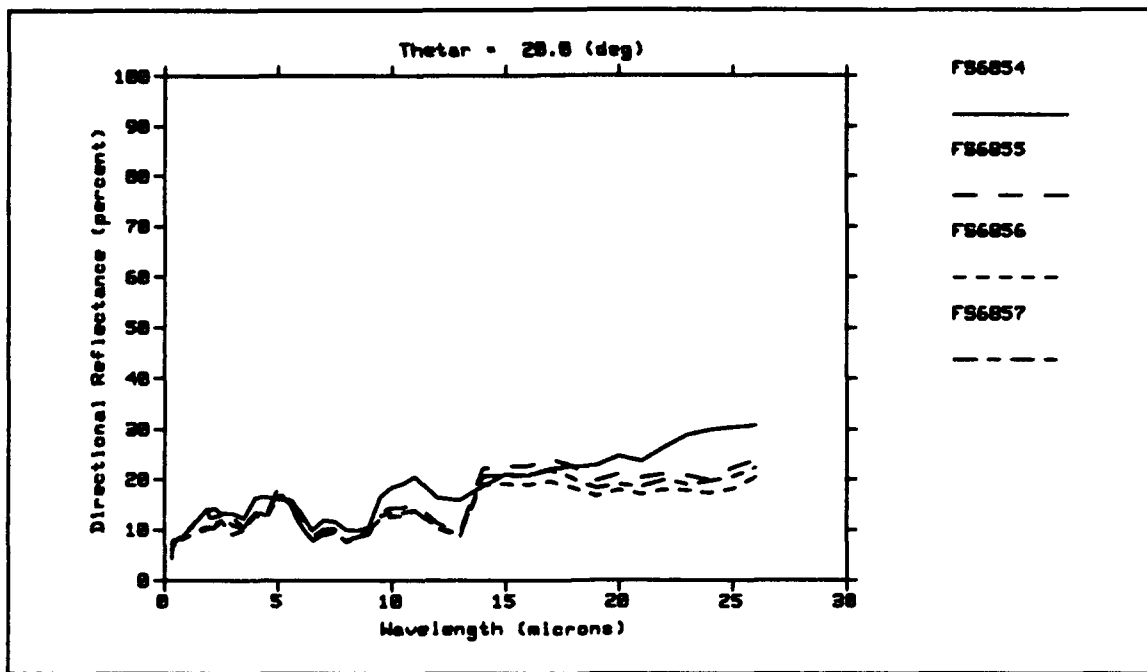


Figure 28. Spectral HDR of the graphite composite materials used in the simulation: silica contaminated (FS6854), clean sample (FS6855), fluorine contaminated (FS6856), unknown (FS6857).

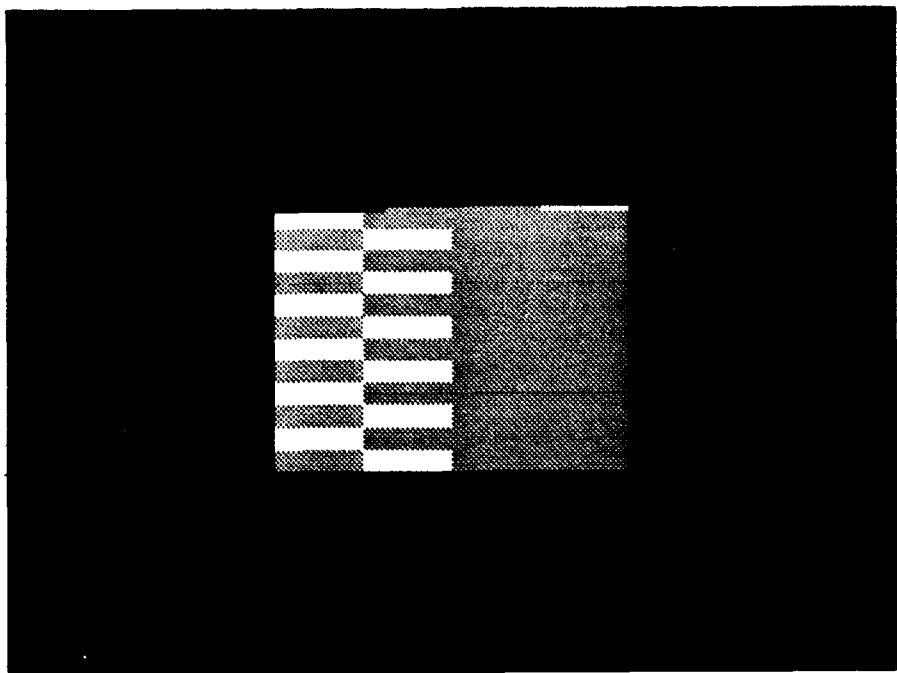


Figure 29. Simulated 8 to 12 micron image of graphite composite panel which has to be spectrally filtered to identify the silicon contaminated material.

3.3 Conclusions

Analytical studies were performed to demonstrate the performance of spectral radiometric image data for NDI applications. The SPCFLT code was developed to simulate the spectral imagery based on laboratory material measurements of the spectral emissivity, and to evaluate spectral filtering algorithms for material identification and discrimination. The TEMPFIT code was developed to recover material temperatures and spectral emissivities from the pixel spectral radiometric data. The initial simulations performed for the NDI applications of identifying rusted versus painted materials, and contamination on graphite composite materials indicate the viability of spectral filtering techniques. In both cases the spectral filter clearly identified the regions in the image with the specified spectral content. The recovery of the surface temperature and spectral emissivity from the spectral radiometric data for the silica contaminated graphite composite and red painted materials also produced promising results.

The analytical models need to be improved in two areas: First, the simulations need to include the effects of electronic and photon noise. Also, NDI and other applications will probably not have ideal, fixed relative positions of the sensor and the scene, and motion blurring effects should be included. Second, more work needs to be done to develop algorithms for uniquely recovering the temperature and spectral emissivity from the radiometric data. Experimental demonstrations of spectral filtering for material identification are presented in the next section.

4.0 SPECTRAL-MATCHED FILTERING

EXPERIMENTAL DEMONSTRATION

Perhaps the most important task accomplished since the first progress report is experimental, not theoretical, demonstration of the power of exploiting spectral signatures to identify materials. Using relatively broad spectral filters from SOC's stock of filters in conjunction with an Inframetrics model 760 IR imager supplied by JPL's test labs, spectral data was collected on the samples originally measured in SOC's lab. These spectral images were recorded on video tape and brought back to SOC for processing and application of spectral filtering algorithms to determine if objects could be discriminated based on their spectral signatures. Following is a detailed description of the experimental setup, the processing performed on the data, and the results.

4.1 Experimental Setup

In order to collect a set of IR spectral images which could be used to demonstrate the power spectral-matched filtering for material identification, an Inframetrics model 760 IR imager was used in conjunction with SOC filters to collect spectral images of test samples. JPL supplied the imager from their test/measurement lab. The model 760 uses a single element of HgCdTe as its detector. A two-axis scan mirror system in front of this detector allows the detector to sample scene radiances throughout an image. Working at standard 60 Hz field rate (2 fields per image, or 30 Hz frame rate), with a spatial IFOV (instantaneous field of view) of 1.8 mrad, the sensor produces an effective 194 pixels during a single line scan lasting 63.5 μ s. Effective integration time, then, for any single pixel is only 330 ns.

Compared to the imager which SOC will produce under the phase II effort which can achieve up to 300 μ s of exposure time at 600 fps image rate, and proportionately longer integration times at lower frame rates, the Inframetrics

camera has only 0.1% of the integration time of SOC's proposed imager. Importance of this comparison is that Inframetrics' imager is not capable of imaging at as fine a spectral resolution as SOC's planned imager, since narrower bandwidth means smaller photon flux at the detector; the Inframetrics is already collecting a minimal number of photons due to its short integration time, implying that fairly broad filters are necessary to achieve reasonable signal levels at the detector. In order to achieve as good a spectral resolution as possible, all of SOC's filters were taken to JPL along with test samples. Testing during setup of the experiment showed that filters no narrower than about 1 μm could be used. This limited the number of usable filters to 5. These filters had center wavelengths of 4.44 μm , 8.07 μm , 9.01 μm , 10.5 μm , and 11.7 μm .

Test articles were set up approximately two feet from the Inframetrics. In order to achieve usable contrasts, the samples were slightly heated by shining a 100 W flood lamp at them. To understand why this was necessary, consider the equation for radiance from an object. Total radiance is given by

$$L(\lambda) = \epsilon \cdot M(\lambda, T) + (1 - \epsilon) \cdot E(\lambda)$$

where $L(\lambda)$ is total object spectral radiance, ϵ is the object emissivity, $M(\lambda, T)$ is the planck blackbody function at the object's temperature T , and $E(\lambda)$ is the irradiance incident on the object; For visible band sensing of objects at reasonable temperatures, the right half of the equation dominates. For space-based IR sensing where background irradiance is near zero, the left side of the equation dominates. But for most earth-bound IR sensing applications where the object being sensed is not significantly above ambient, both terms of the equation are important. Note especially that if the incident irradiance is also a blackbody function at the same temperature as the object being viewed, the emissivity of the object disappears, and its total radiance is just the planck function. In a room where all objects are at nearly the same temperature, the background irradiance will be nearly a Planck function at the temperature of the room. Hence, almost no contrast will be seen between objects. In fact, when the inframetrics was first pointed towards the test

objects without the lamp shining on them, almost no contrast was seen. Heating them slightly allowed contrast to be seen.

Four sets of objects were measured. The first set consisted of a rust sample, a red painted sample, and a red painted sample with a thin film of oil on it. The second set consisted of five graphite-epoxy composite coupons with various contaminants supplied by Composite Optics Incorporated (COI). The third set consisted of the samples of hot and cold solder, and the fourth was a populated circuit board. These objects were placed in the target area against a passive blackbody, i.e., a non-heated object with unity emissivity. After allowing about 10 minutes for the objects temperatures to stabilize, the aforementioned spectral filters were placed in front of the Inframetrics one at a time, and the resulting spectral image recorded on video tape.

4.2 Data Processing

After returning to SOC, images were grabbed from the video tape and written to hard disk using a Data-Translation DT2871 RGB/HSI frame grabber. Two problems made this task rather challenging. First, amazingly no driver was supplied with the frame grabber to allow images to be written to disk, so SOC had to write its own. Second, as stated above, the DT2871 is an RGB/HSI color frame grabber, meaning three separate channels carry the color information. The Inframetrics, as do most video cameras, outputs a composite color signal which encodes all video information on a single signal. Although recorded images were only black and white, the color burst signal at the beginning of each video line caused the DT2871 to have problems maintaining sync on the video signal, causing "tears" and ripples to show up periodically in the grabbed images. In order to minimize noise, the Inframetrics was set to average 16 frames together, and four of these images were grabbed and averaged together to further reduce noise (recall the 300 ns integration time). Images had to be grabbed manually rather than by a computer program to ensure that corrupted images were not present in the average.

After grabbing four images from each spectral band and from 3 μm - 5 μm and 8 μm - 12 μm broad bands and averaging the four images together, the resultant spectral images were processed using various spectral filtering algorithms incorporated into a computer program written specifically to process the images. Since the Inframetrics was not providing any absolute radiance information, the first step in the processing was to normalize each spectral image. To accomplish this, the average brightness of a region of the passive blackbody was picked as the normalization value for each spectral image. Each pixel in each spectral image was then divided by the normalization value for that spectral image. In the final instrument, this normalization would be somewhat analogous to removing the temperature dependance of each pixel's spectral radiance.

To demonstrate spectral matched filtering, spectra from the various samples were obtained by averaging a small, identical area in each of the spectral images. The resultant spectrum was then used as the target spectrum in a variety of filtering algorithms, described in Section 3, above. The amount of computational power required to implement these algorithms on 20 point spectra at each of 50,000 pixels 30 times a second should be quite apparent. By way of comparison, a 66 MHz 486-based PC required a full minute to implement the zero-mean absolute differential area algorithm on 5 point spectra at each of 200,000 pixels (similar number of computations); this powerhouse of a computer, then, takes nearly 2,000 times as long to perform the same number of computations as the SOC MIIRIS instrument will.

4.3 Spectral Filtering Demonstration Results

Before presenting the results of the spectral matched filtering experimental demonstration, a few words about the limitations of the experiment compared to the prototype instrument to be developed under the phase II effort are in order. First, only 5 point spectra were obtained on the observed samples, whereas the MIIRIS instrument will collect and process a minimum of 20 point spectra. Second, the bandwidth of the filters used in the experiment were about 20% bandwidth at 4.44 μm , and about 10% at the four longer wavelengths. The MIIRIS instrument will

collect spectra at about 1.5% bandwidth in the infrared, and 2% in the visible. Third, spectral images collected in the experiment contained not only the objects' radiances, but also background radiances reflected from the backside of the filter placed in front of the imager. These limitations notwithstanding, the results of the experimental demonstration were none-the-less quite astounding. Figure 30 shows the broad-band image of the COI samples. Some contrast can be seen in the image, but not much. The samples are from left to right, FS6854 (contaminated), FS6855 (clean), FS6856 (contaminated), FS6856 (contaminated), FS6857 (contaminated), and FS6858 (unknown). Note that FS6856 appears splotchy. Note also that FS6857 has a small piece of kapton tape on it, although the poor reproduction of the image in this document does not make it apparent. Spectra were obtained for each of the samples, including spectra from the bright areas of FS6856 (referred to as FS6856B), and the dark areas of FS6856 (referred to as FS6856D), and from the kapton tape. These spectra, except for FS6858, are presented in Figure 31.

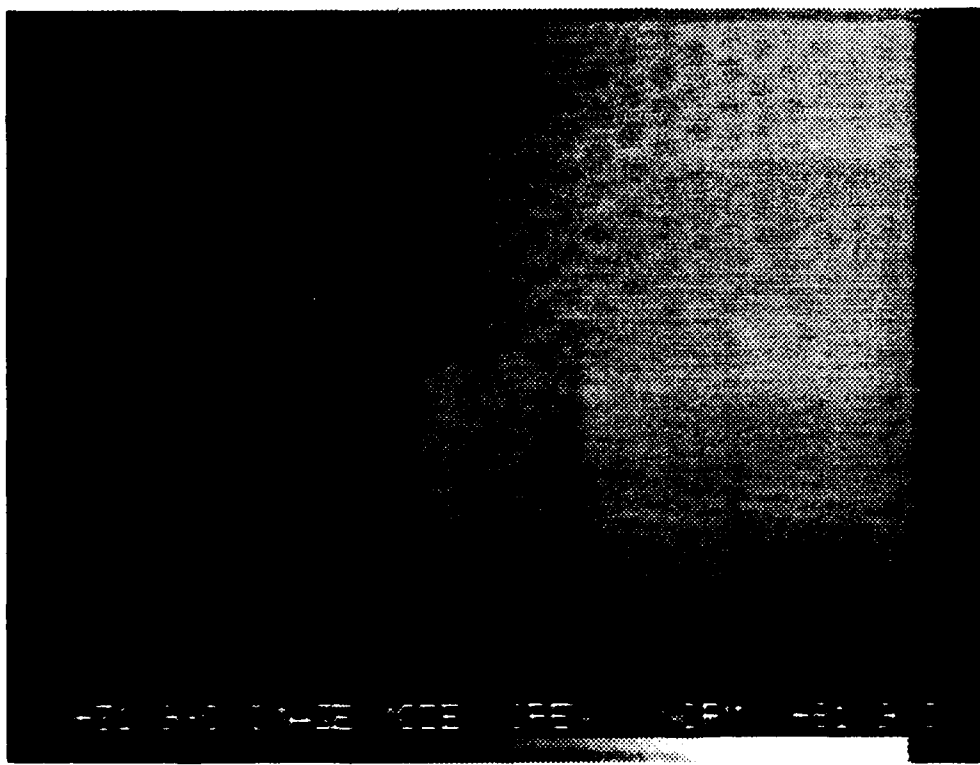


Figure 30. 8 μm - 12 μm broad-band image of COI samples.

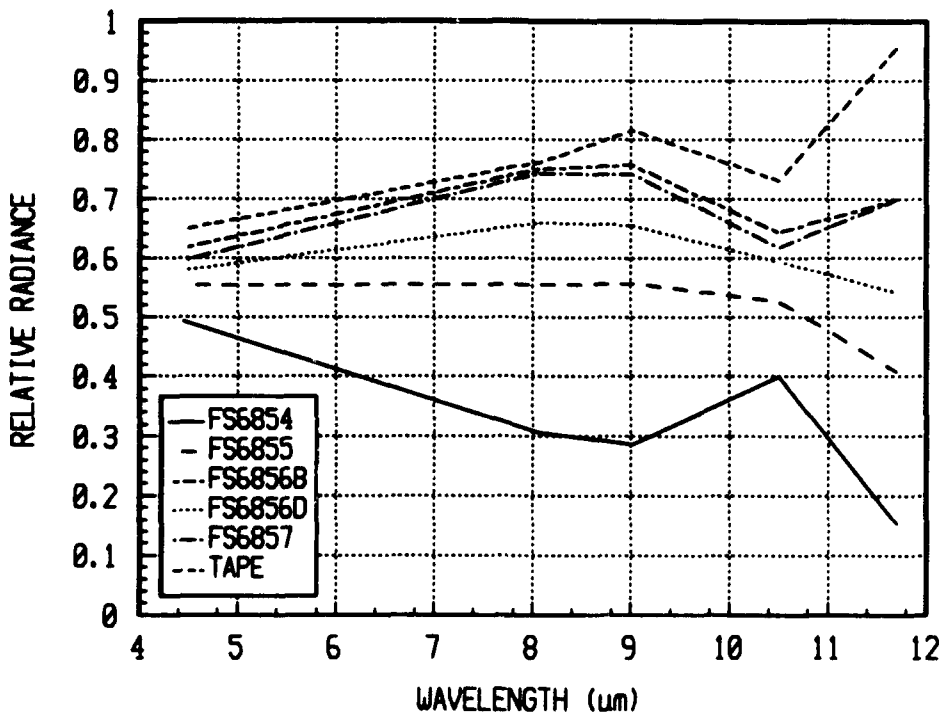


Figure 31. Relative spectrum of COI samples.

Results of the application of the zero-mean absolute differential area applied to every pixel in the image using each of the above spectra as the filtering spectrum are presented in Figures 32 through 37. These figures show the output of the filtering algorithm for each pixel, on a scale of 0 to 1, without any scaling or thresholding. Note the ability of the algorithm to identify each material. Note also that in Figure 34, when the spectrum from the bright splotches on FS6856 is used as the filter, not only do the bright patches show up, but so does FS6857, indicating that the bright areas are contamination since FS6857 is also a contaminated sample. Conversely, when the spectrum from the dark areas of FS6856 is applied as the filter, FS6855 also shows some correlation, although not as strong, indicating that the dark areas are relatively free of contamination.

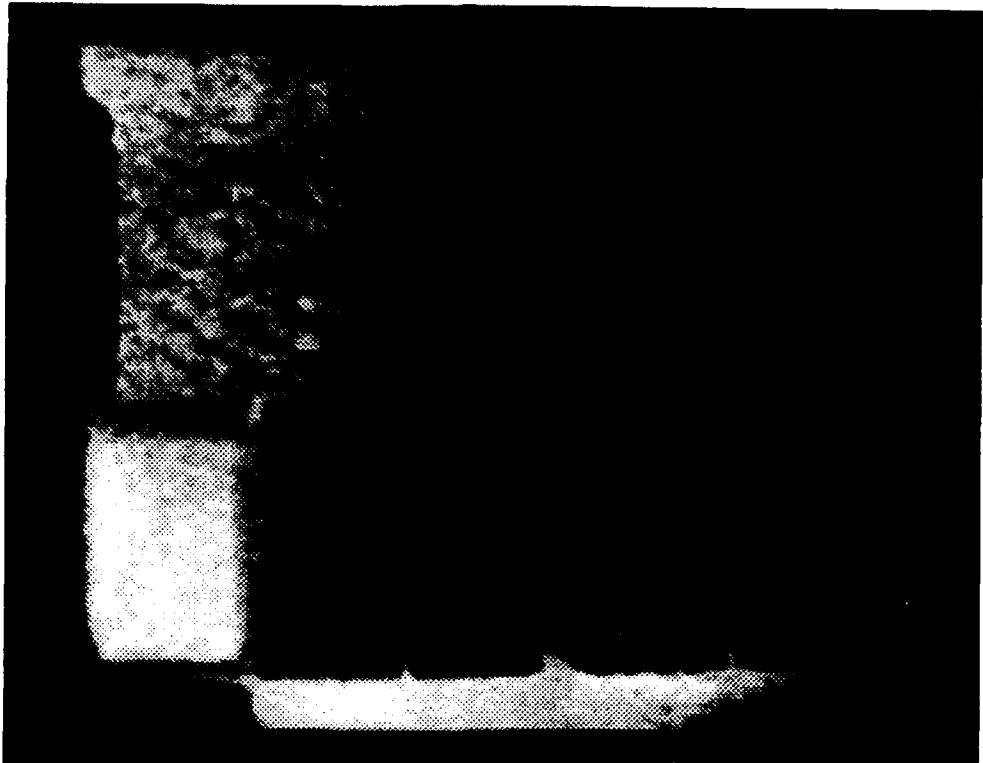


Figure 32. Filtered image using F56854 as filter spectral radiance.

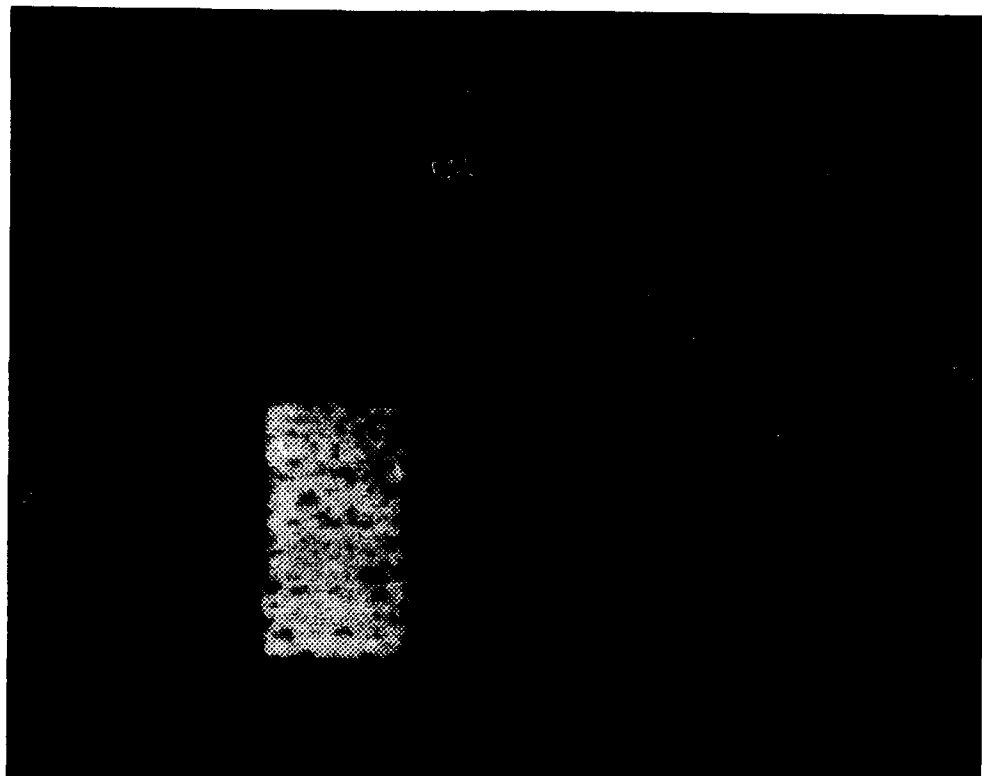


Figure 33. Filtered image using F56855 as filter spectral radiance.

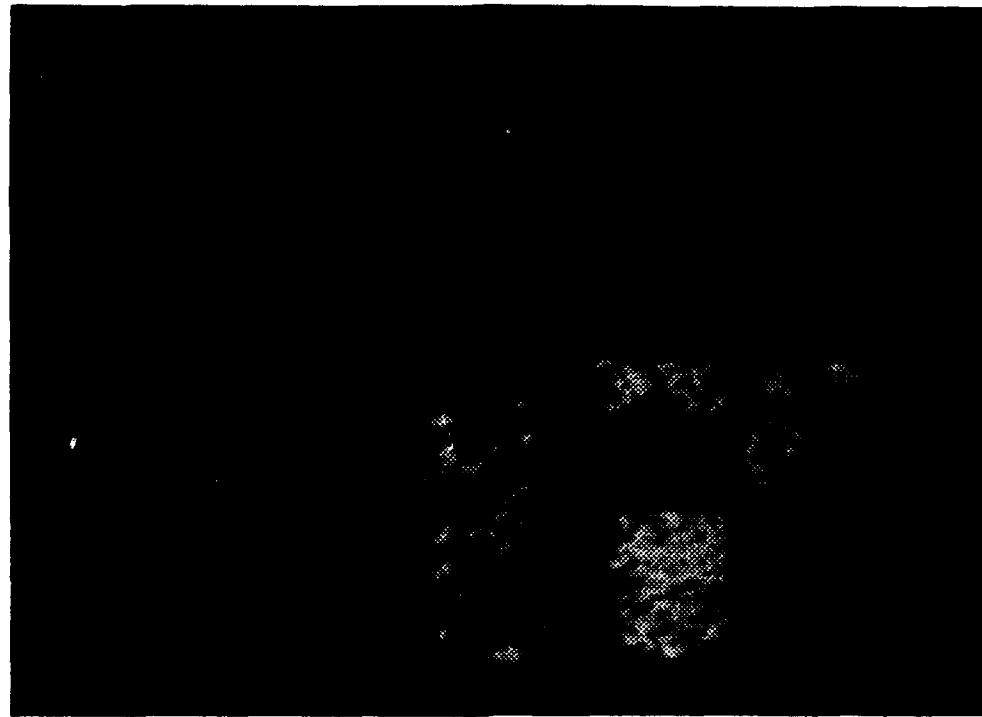


Figure 34. Filtered image using bright areas of F56856 as filter spectral radiance.



Figure 35. Filtered image using F56857 as filter spectral radiance.

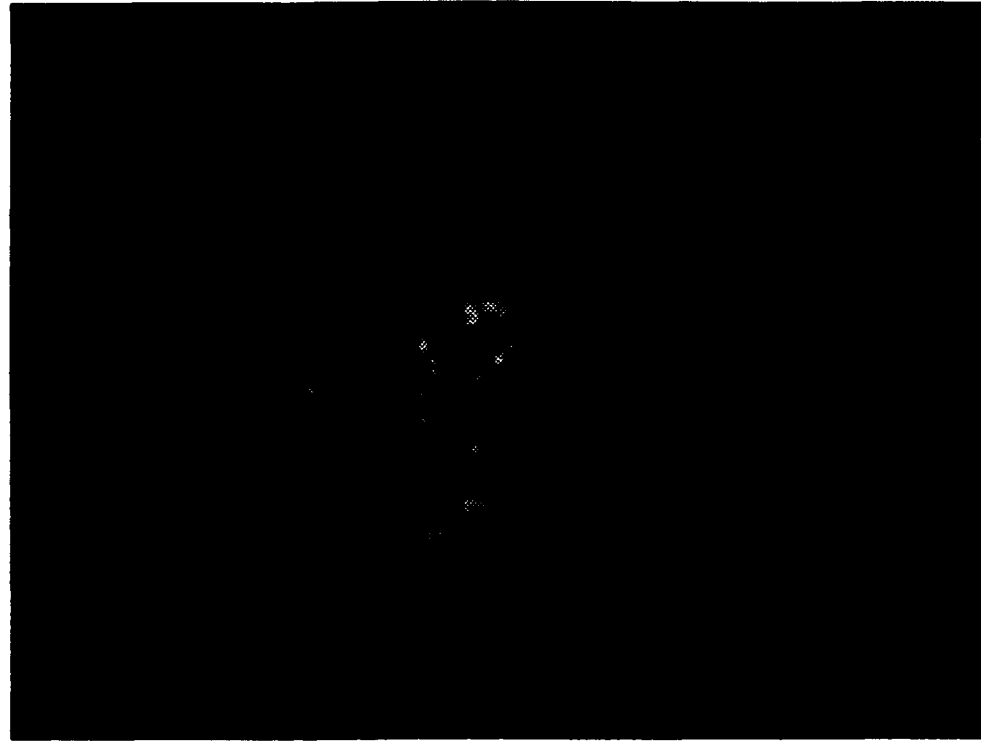


Figure 36. Filtered image using dark areas of F56856 as filter spectral radiance.

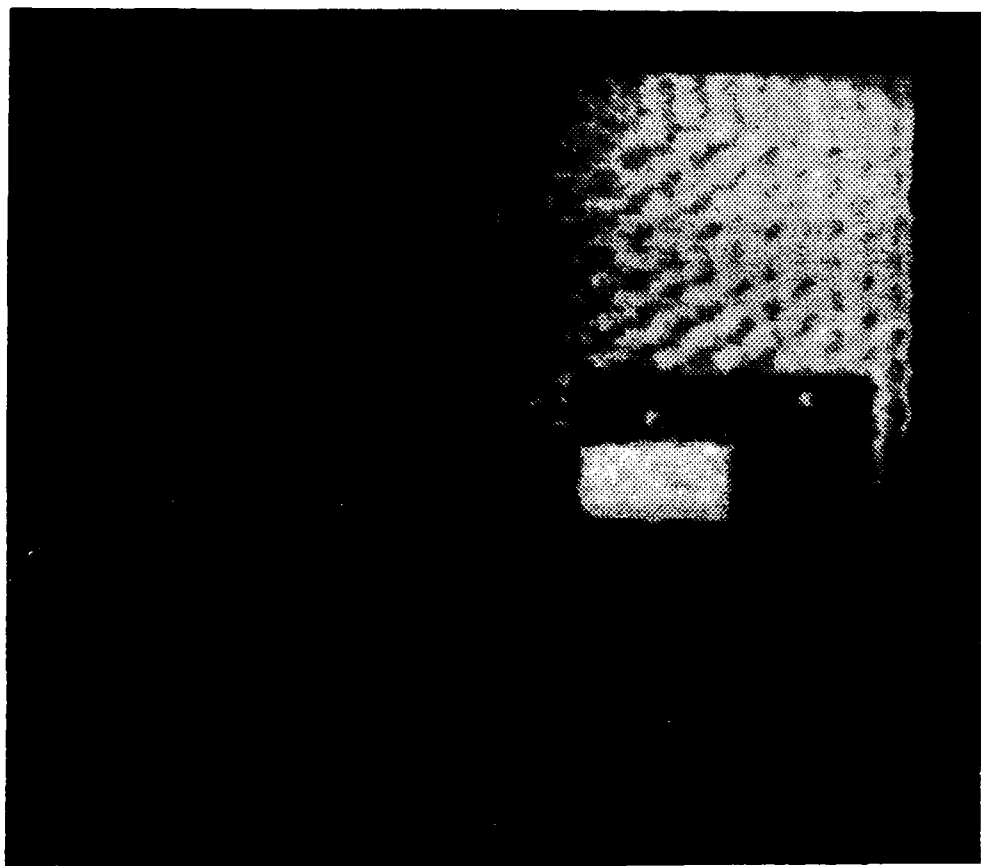


Figure 37. Filtered image using kapton tape as filter spectral radiance.

Similar processing was done for the rust, paint, and paint with oil samples. Figure 38 shows the broad-band image of the three samples in front of the passive blackbody. The samples are, from left to right, rust, red paint, and red paint with oil. Spectra from these objects is shown Figure 39. Note that these spectra have one less data point. One of the spectral images collected at JPL turned out to be unusable, but this wasn't known until the data was processed. Also note that the ordinate axis starts at 0.5 in this plot rather than 0.

Again, each of one of these spectra was used as the filtering spectrum in the zero-mean, absolute differential area filtering algorithms. Results of the filtering are shown in Figures 40 to 42. When the paint with oil spectrum is used as the filter, that sample is clearly identified, with the rust sample completely rejected, and the paint sample slightly visible. This is expected since the paint spectrum is closer to the paint with oil spectrum than is the rust spectrum. When the paint spectrum is used as the filter, both rust and paint with oil show a slight correlation (but not nearly as strong as the paint sample), again because the paint spectrum is, to an extent, mid way between the two. When rust is used as the filtering spectrum, both other samples still show a slight correlation, as does the blackbody behind. Since the rust is approaching unity emissivity with IR emissivity shape nevertheless similar to the other two samples, this makes sense. If more spectral points had been acquired with better resolution and potentially into the visible band, rejection of the other samples against the rust spectrum would have been more complete.

These results clearly show the power of spectral-matched filtering as a technique to discriminate and identify materials based on their spectral signatures. Even though the experiment was quite limited in the amount and quality of spectral data collected, the filtering algorithms were nevertheless able to extract each of the samples that were filtered for. When this technique is implemented in real-time with more and higher quality spectral imagery data, ability to accurately identify materials being viewed will be phenomenal.

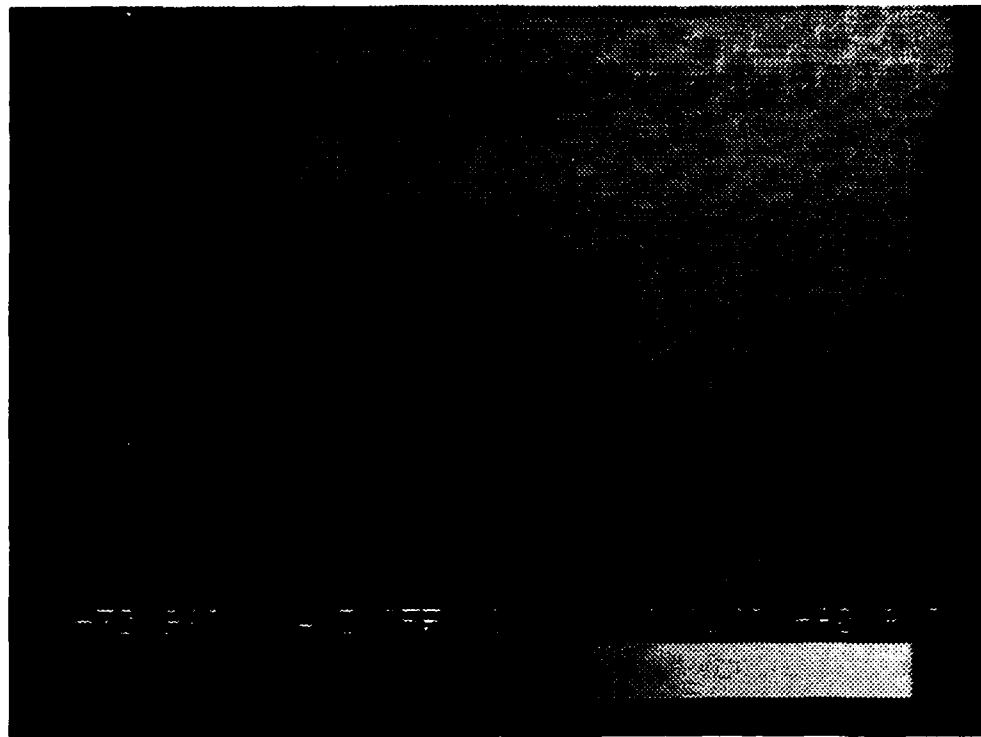


Figure 38. 8 μm - 12 μm broad band image of rust (left), red paint (center), and oil-coated red paint (right).

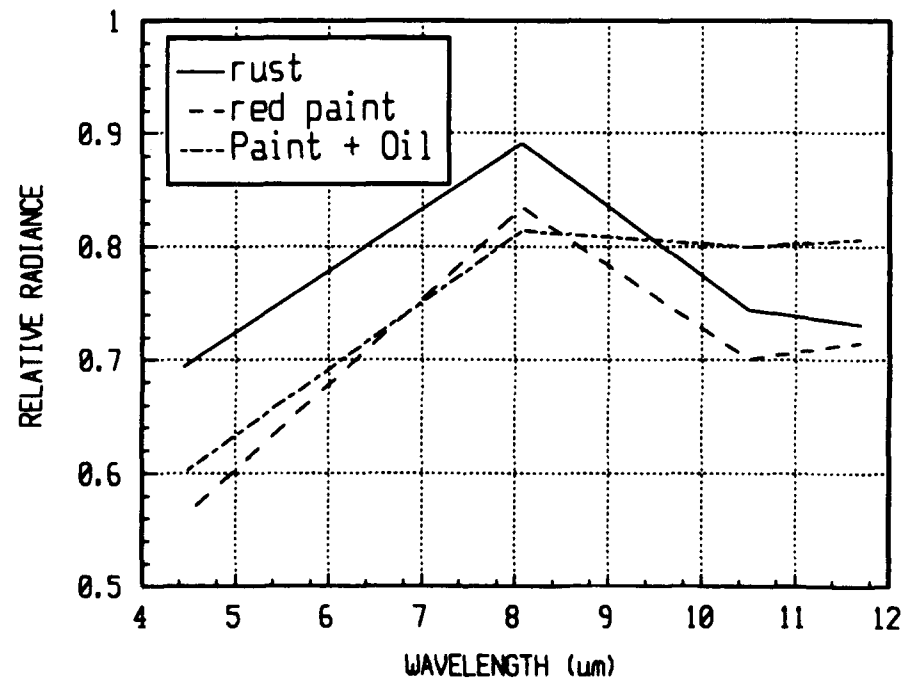


Figure 39. Relative spectral radiances of rust, paint and oil-coated paint samples.

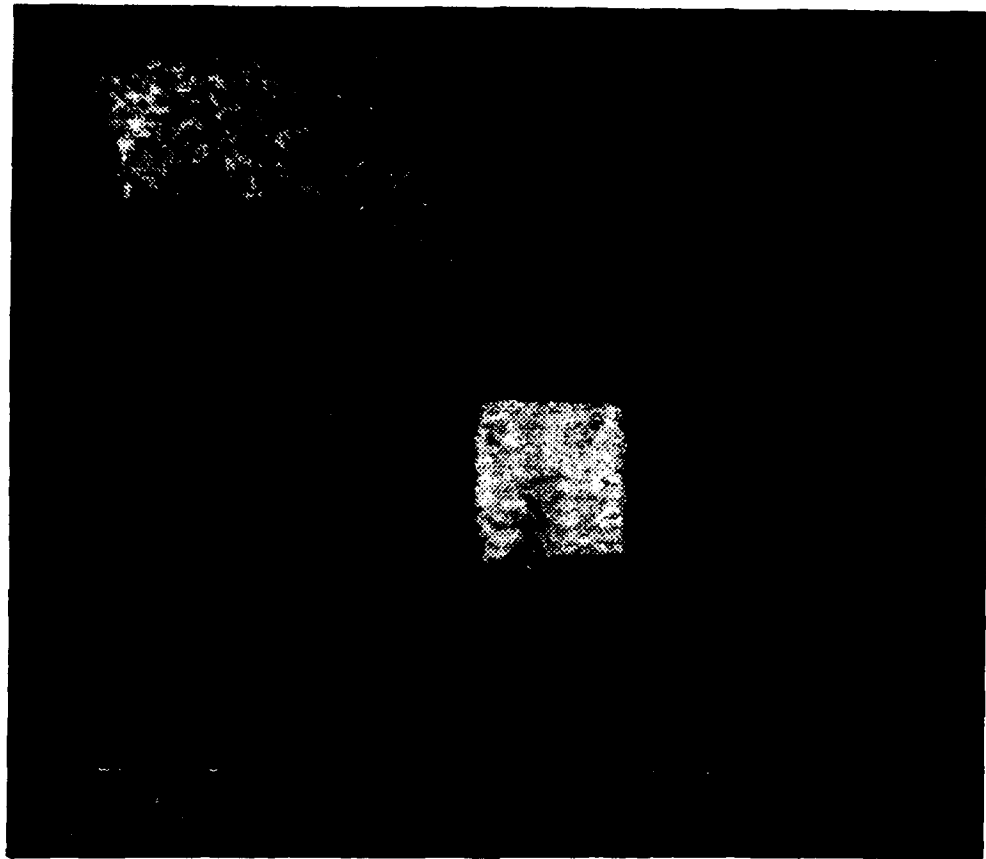


Figure 40. Filtered image using oil-coated paint as filter spectral radiance.

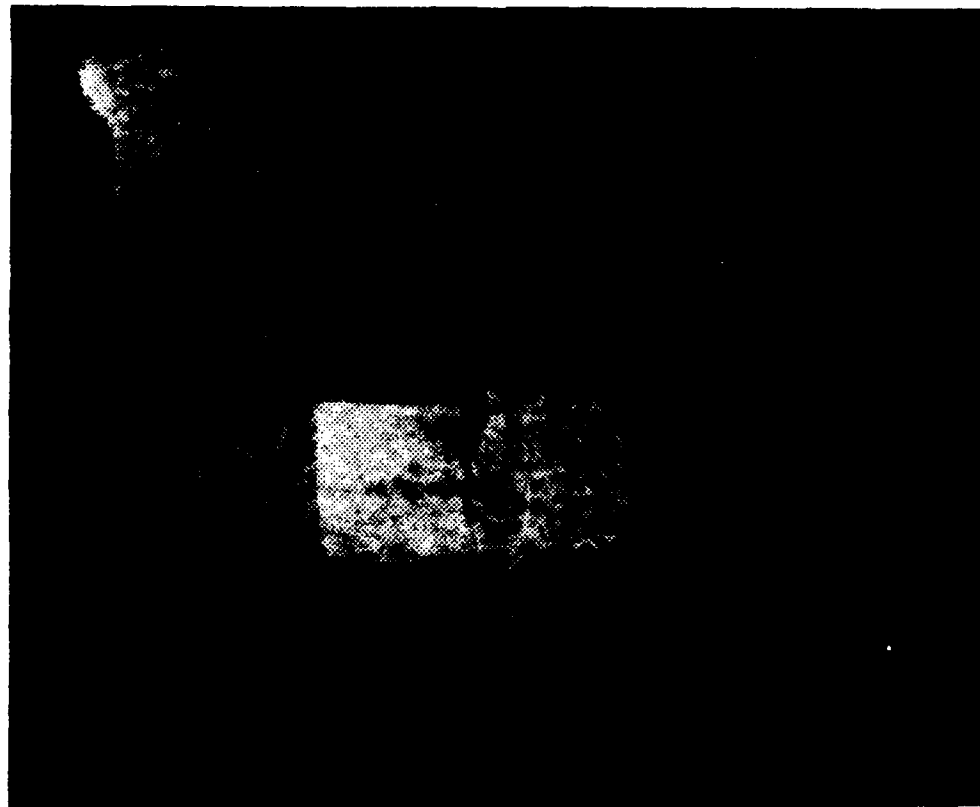


Figure 41. Filtered image using paint as filter spectral radiance.

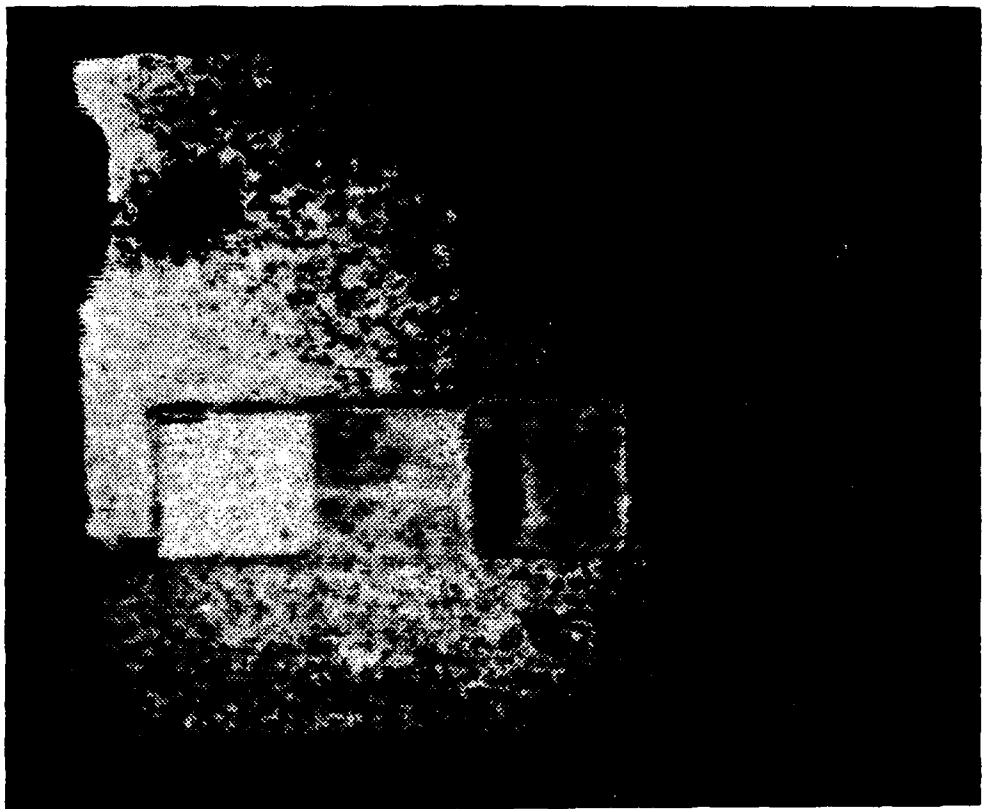


Figure 42. Filtered image using rust as filter spectral radiance.